

ABSTRACT

Title of dissertation: Wave Chaos Studies
and The Realization of
Photonic Topological Insulators

Bo Xiao, Doctor of Philosophy, 2022

Dissertation directed by: Professor Steven Anlage
Department of Electrical and
Computer Engineering

Wave propagation in various complex media is an interesting and practical field that has a huge impact in our daily life. Two common types of wave propagation are examined in this thesis: electromagnetic wave propagation in complex wave chaotic enclosures, where I studied its statistical properties and explored time-domain pulse focusing, and unidirectional edge modes propagating in a reciprocal photonic topological insulator waveguide.

Several theories, e.g. the Random Matrix Theory and the Random Coupling Model, have been developed and validated in experiments to understand the statistical properties of the electromagnetic waves inside wave chaotic enclosures. This thesis extends the subject from a single cavity to a network of coupled cavities by creating an innovative experimental setup that scales down complex structures, which would otherwise be too large and cumbersome to study, to a miniature version that retains its original electromagnetic properties. The process involves shrinking down the metal cavity in size by a factor of 20, increasing the electromagnetic wave

frequency by the same factor and cooling down the cavity by a dilution refrigerator to reduce its ohmic loss. This experimental setup is validated by comparison with results from a full-scale setup with a single cavity and it is then extended for multiple coupled cavities.

In the time domain, I utilized the time-reversal mirror technique to focus electromagnetic waves at an arbitrary location inside a wave chaotic enclosure by injecting a numerically calculated wave excitation signal. I used a semi-classical ray algorithm to calculate the signal that would be received at a transceiver port resulting from the injection of a short pulse at the desired target location. The time-reversed version of this signal is then injected into the transceiver port and an approximate reconstruction of the short pulse is observed at the target port.

Photonic topological insulators are an interesting class of materials whose photonic band structure can have a bandgap in the bulk while supporting topologically protected unidirectional edge modes. This thesis presents a rotating magnetic dipole antenna, composed of two perpendicularly oriented coils fed with variable phase difference, that can efficiently excite the unidirectional topologically protected surface waves in the bianisotropic metawaveguide (BMW) structure recently realized by Ma, et al., despite the fact that the BMW medium does not break time-reversal invariance. In addition to achieving high directivity, the antenna can be tuned continuously to excite reflectionless edge modes to the two opposite directions with various amplitude ratios.

Overall, this thesis establishes the foundation for further studies of the universal statistical properties of wave chaotic enclosures, and tested the limits of its

deterministic properties defined by the cavity geometry. It also demonstrated in experiment the excitation of a unidirectional edge mode in a Bianisotropic Metawaveguide, allowing for novel applications in the field of communications, for example phased array antennas.

Wave Chaos Studies
and The Realization of
Photonic Topological Insulators

by

Bo Xiao

Dissertation submitted to the Faculty of the Graduate School of the
University of Maryland, College Park in partial fulfillment
of the requirements for the degree of
Doctor of Philosophy
2022

Advisory Committee:

Professor Steven Anlage, Chair/Advisor

Professor Thomas Antonsen

Professor Thomas Murphy

Professor Neil Goldsman

Professor Yanne Chembo

Professor John Cumings, Dean's Representative

© Copyright by
Bo Xiao
2022

Acknowledgments

For the work on testing the Random Coupling Model predictions in scaled-down cavities (Chapter 2 - 5), we acknowledge the assistance of Bisrat Addissie. This work was supported by ONR under Grant No. N000141512134, AFOSR COE Grant FA9550-15-1-0171 and ONR DURIP grant N000141410772, and the Maryland Center for Nanophysics and Advanced Materials.

For the work on focusing waves at arbitrary location in a ray-chaotic enclosure using time-reversed synthetic sonas (Chapter 6), we thank the group of A. Richter (Uni. Darmstadt, Germany) for graciously loaning the cut-circle billiard, H.J. Paik and M. V. Moody for use of the pulsed tube refrigerator, Martin Sieber for comments on improving the short orbit calculation algorithm, and the High-Performance Computing Cluster at UMCP for use of the Deepthought cluster. This work is funded by the ONR under Grants No. N00014130474 and N000141512134, and the Center for Nanophysics and Advanced Materials (CNAM).

For the work on exciting reflectionless unidirectional edge modes in a photonic topological insulator medium (Chapter 7), the work was supported by ONR under Grant No. N000141512134, AFOSR COE Grant FA9550-15-1-0171 and the National Science Foundation (NSF) under Grants No. DMR-1120923, No. PHY-1415547 and No. ECCS-1158644.

Table of Contents

List of Tables	vi
List of Figures	vii
List of Abbreviations	xv
1 Introduction and Overview	1
1.1 Background	2
1.2 Thesis Overview	3
1.3 Ray-chaotic Cavities	5
1.4 Random Matrix Theory	7
1.4.1 Random Matrices	7
1.4.2 Normalized Spacings Between The Nearest Eigenfrequencies	8
1.5 Random Coupling Model	9
1.5.1 S-parameters & Z-parameters	11
1.5.2 Normalized Impedance	12
1.5.3 Loss Parameter α	13
1.5.4 Extensions of RCM	14
2 Testing The Random Coupling Model Predictions in a Scaled-Down Cavity With Remote Injection Setup	16
2.1 The Need For Scaled Cavities	18
2.2 Scaling of The Cavity	20
2.2.1 Frequency Scaling	20
2.2.2 Cavity Wall Conductivity Scaling	21
2.2.3 Scaling Limits	26
2.3 Experimental Setup	26
2.3.1 VNA & Extenders	28
2.3.2 Cryostat	30
2.3.3 Free-space Propagation Path	33
2.3.4 Mode Stirrer	36
2.4 Testing Experiments	40

2.4.1	Overall Plan	40
2.4.2	Free-space Propagation Path Measurement	42
2.4.3	Collecting an Ensemble of Cavity Data	42
2.4.4	Direct Injection	45
2.4.5	Remote Injection	48
2.4.6	Extension to Multiple Connected Cavities	48
2.4.7	Further Studies	50
3	Introducing Radiation Efficiency to the Random Coupling Model	54
3.1	Radiation Efficiency η and RCM With Lossy Ports	55
3.1.1	\mathbf{Z}_{rad} , \mathbf{Z}_{ant} , \mathbf{Z}_{cav} and \mathbf{Z}_{avg}	56
3.1.2	Radiation Efficiency η in One-port Systems	58
3.1.3	Radiation Efficiency η in Multi-port System	61
3.1.4	Scaling Relation Between α and η	61
3.2	Applying Radiation Efficiency η to Experimental Data	64
3.2.1	Calculating Loss Parameter Through Time-domain Energy Decay Time τ	66
3.2.2	Fitting Radiation Efficiency η	67
3.2.3	η 's Independence From Cavity's α	70
3.2.4	Apply η to Experimental Data	71
4	Single Scaled Cavity Experiment	74
4.1	Full-Scale Cavity Analysis	75
4.1.1	Frequency Dependent Loss Parameter	76
4.1.2	Fitting Error	77
4.2	Miniature Cavity Analysis	79
4.2.1	Frequency Dependency of η and α	80
4.3	Comparison Between Full-Scale and Miniature Cavity	82
4.3.1	Full-Scale Cavity with 1/4 absorber for $N = 1$ Frequency Segment	83
4.3.2	Full-Scale Cavity with 1/4 absorber for $N = 10$ Frequency Segments	84
4.4	α Range Limitation	86
4.4.1	Difference in $\text{Re}[\xi_{11}]$ and $\text{Re}[\xi_{22}]$	86
4.4.2	Difference in $\text{Re}[\xi_{12}]$, $\text{Re}[\xi_{21}]$ and $\text{Im}[\xi_{12}]$, $\text{Im}[\xi_{21}]$	87
5	Multiple Scaled Cavity Experiment	91
5.1	Experimental Design	92
5.1.1	Design considerations	93
5.1.1.1	Cost efficient construction	93
5.1.1.2	Efficient use of space and material	93
5.1.1.3	Flexible configuration	100
5.1.1.4	Perturbers	103
5.1.1.5	Antenna and lens alignment	103
5.1.2	Assembled setup	107

5.2	Lessons Learned	108
5.2.1	Design assistance tools	110
5.2.1.1	CST modeling tool	110
5.2.1.2	3D printed models	112
5.2.2	Methods to Construct a Metal Box	112
5.2.3	External vendors	115
5.3	Experimental Results	116
6	Focusing Waves at Arbitrary Locations in a Ray-Chaotic Enclosure Using Time-Reversed Synthetic Sonas	119
6.1	Introduction	120
6.2	Experiment	124
6.2.1	Calculation of Synthetic Sona	124
6.2.2	Experimental Setup	125
6.2.3	Frequency Domain Experiment	127
6.3	Analysis	129
6.3.1	Reconstruction Quality	129
6.3.2	Effects of Loss and Mismatched Port Coupling	131
6.3.2.1	Effect of Loss on Reconstruction	131
6.3.2.2	Mismatched Port Coupling	134
6.3.3	Synthetic Sona Duration Constraint	136
6.4	Conclusion	141
7	Exciting Reflectionless Unidirectional Edge Modes in a Reciprocal Photonic Topological Insulator Medium	142
7.1	Introduction	143
7.2	Design and Simulations	145
7.3	Experiment	146
7.4	Analysis	152
7.5	Ferrite Induced Non-reciprocity	158
7.6	Conclusions	159
8	Conclusions	160
8.1	Prior Works	162
8.2	Future Work	163
	Appendices	165
	Appendix A MATLAB Script For Generating Normalized Impedance Ensem- bles For 2-port Systems	166
	Bibliography	171

List of Tables

7.1	Summary of extreme transmissison values as deduced from experimental data where T_L and T_R are transmission amplitude to left and right, respectively.	158
-----	---	-----

List of Figures

1.1	Diagram of an electric power system; transmission system is in blue. [1]	2
1.2	Random Matrix Theory predictions for the Probability Density Functions of (a) $\text{Re}[z]$ and (b) $\text{Im}[z]$ as a function of increasing α , for a one-port time-reversal symmetric wave-chaotic cavity. Figure 2.3 in Ref. [2].	14
2.1	RCM-predicted probability density function of power ratios $R_N(\alpha = 6) \equiv P_{in}^{(N)}/P_{in}^{(1)}$ for chains of up to seven cavities: the high-loss regime is assumed for all the (statistically identical) cavities in the chain. This is Figure 7 in Ref. [3].	19
2.2	Electrical resistivity of copper vs. temperature. The different curves on the plot are the experimental results for different aluminum samples and were measured with different techniques at different times from 1908 to 1981. (which is Figure 1 in [4])	24
2.3	The schematics for the scaled cavity experiment setup.	28
2.4	Block diagram for Virginia Diode Inc frequency extender modules. (*) Variable attenuator. (†) Isolator. Picture taken from VDI product manual [5].	29
2.5	A typical setup with VNA and VDI extenders for measurement. Picture taken from VDI product manual [5].	30
2.6	The drawings (left), the outside vacuum can (middle) and the cooling plates inside of the cryostat (right). The cooling plates are cooled in a staged manner from 50K at the top to 10mK at the bottom. The sample will be mounted onto the 10 mK plate, also called the sample plate.	32
2.7	The setup for high frequency waves to propagate in free-space from the frequency extender to the cavity, and from the cavity to the receiving frequency extender. The horn antennas can efficiently launch and receive electromagnetic waves and the Teflon lens collimates the waves into a parallel beam.	34

2.8	Magnetically coupled mode stirrer powered by a cryogenic stepper motor. The magnetic strip outside the cavity (lower yellow bar in the left side) is coupled by static magnetic field with the magnetic strip inside the cavity (upper yellow bar in the left side), eliminating the need for any hole on the wall. The upper right inset is an example of the mode stirrer placed inside the cavity.	39
2.9	The transmission amplitude in dB for free-space propagation measurement. The x-axis and y-axis are the distance between the lens to the transmitter antenna (d_1) and the receiver antenna (d_2) respectively. The yellow dotted circles enclose the region for best d_1, d_2 values for optimal transmission.	43
2.10	Experimentally measured reflection (top two plots) and transmission (bottom two plots) magnitude for the $s = 20$ cavity for 5 realizations created by rotating the magnetically coupled mode stirrer. The left column plots the data in the full frequency range from 75 GHz to 110 GHz while the right column zooms in a 100 MHz window. Each curve is wildly different from others but yet follow the same slowly varying trend which is the non-statistical system specific feature. . . .	44
2.11	Power ratio Λ as a function of frequency and its histogram for a good ensemble (left) and a bad ensemble (right) data. Λ should have a large mean and a large dynamic range if the cavity modes are well perturbed and uncorrelated, which gives us a good ensemble of data. . . .	45
2.12	Loss parameter α values for the full scale cavity measured by collaborators at U.S. Naval Research Laboratory. Each α value is calculated from experimental data in a 0.1 GHz window at the specified frequency. The data points are taken from Table 1 in [6].	46
2.13	Probability Density Function (PDF) of the normalized impedance for a direct injection experiment on a scaled-down $s = 20$ copper cavity (dotted line), in comparison with the RCM Monte Carlo simulation with $\alpha = 4.5$ (solid line).	47
2.14	3D-printed model of the multiple connected cavities and the configuration for a 3-cavity cascade drawn in CST.	49
2.15	The air region of the 3-cavity cascade model with cavity walls and backplane omitted. The wave goes into the first cavity through the antenna mounting point, then couples into the second cavity mounted on the other side of the backplane (not shown) through an aperture. It is then coupled to the third cavity through the other aperture, and gets out through the antenna mounting point on the third cavity. . .	50

2.16	A simple cascade of three scaled cavities. Top: the graph of the cascade, consisting of three nodes (scaled cavities) and two edges (apertures connecting two neighbor cavities). Bottom: the configuration of scaled cavities mounted onto the two opposing sides of a central plate. Green rectangles represent scaled cavities on the front side and blue rectangles represent scaled cavities on the back side. Orange circles represent apertures connecting the two cavities on the opposing sides.	52
2.17	A network of seven scaled cavities. Top: the graph of the network, consisting of seven nodes (scaled cavities) and eight edges (apertures connecting two neighbor cavities). Bottom: the configuration of scaled cavities mounted onto the two opposing sides of a central plate. Green rectangles represent scaled cavities on the front side and blue rectangles represent scaled cavities on the back side. Orange circles represent apertures connecting the two cavities on the opposing sides.	53
3.1	The circuit model for a lossless (left) and a lossy (right) antenna. Z_{ant} is the input impedance of the antenna which is approximated by Z_{avg} (which also includes short orbit effect in addition to Z_{ant}) in RCM normalization process, Z_{rad} is the radiation impedance which describes the feature of the port, and R is the real part of Z_{rad} that represent the power loss due to radiation. Figure 4, 5 in [7].	58
3.2	The inverse Fourier transform of the measured S-parameters give the value of τ from each fit in log-scale versus time. a) For the case of transmission and b) for the case of reflection of the $s = 20$ scaled enclosure measured through remote injection. Data from 9 realizations at room temperature are plotted with different colors. The purple line is the average, and the green line is the linear fit for the energy decay portion of the average. The slope of the fitted line is $-1/2\tau$, where τ is the energy decay time of the cavity. The time domain response inside the blue dashed box in (b), labeled 'Prompt response', arises from the impedance mismatch between the external transmission channel and the cavity. This information is captured in Z_{avg}	67
3.3	Comparison between the normalized impedance PDF for a 2-port system from a RCM Monte Carlo simulation with $\alpha = 5.6$, in solid lines, and that from a normalization process of experimental data with $\eta_{11} = 0.14$ and $\eta_{22} = 0.19$, in dotted lines.	69
3.4	The comparison between the normalized impedance PDF from a direct injection experiment with an empty cavity (solid lines), and that from a one-sided remote injection experiment with an empty cavity (dotted lines). The remote injection data is processed using the radiation efficiency $\eta_{11,\text{absorber}}$ obtained from the one-sided remote injection with an absorber.	71

3.5	A comparison between α values calculated from different methods as a function of time during a cycling of the dilution refrigerator hosting the scaled cavity. Blue solid line: calculated from time domain energy decay time method; Dotted lines: calculated from RCM normalization process with various values of η	73
4.1	The full-scale cavity α measured by Zachary Drikas and Jesus Gil Gil at NRL with various number of absorbers inside. The left side plot is the average α for the whole frequency range, i.e. number of frequency segments $N = 1$. The right side plot is the α for $N = 10$ frequency segments.	77
4.2	The fitting error for calculating the $\alpha_{N=10}(f)$ values for the full-scale cavity is mostly around 0.05. The few high error data points are for $\alpha > \alpha_{\max}$ over the limit of the simulation α range. The right plot shows a typical case of the comparison between the PDF curves for the 5 th frequency segment where the fitting error is 0.036164.	78
4.3	The tunable range of α values by using different wall material and varying temperature. The least lossy wall material is polished copper, which gives a range of $2.6 \leq \alpha \leq 4.2$, including the α_{full} for full-scale cavity with 1/4 absorber in its range. The plotted α is calculated from the time-domain energy decay time τ	80
4.4	The horn antenna has higher gain at higher frequency band which results in higher radiation efficiency. Left plot taken from Virginia Diode, Inc documentation Nominal Horn Specifications [8].	81
4.5	The frequency dependent loss parameter for the miniature cavity calculated from the time-domain energy decay time method, α_Q , and from fitting with RCM simulation results, α_{fit}	82
4.6	The comparison of PDFs for the normalized impedance $\text{Im}[\xi_{21}]$ for the full-scale cavity with 1/4 absorber, the miniature cavity at 103 Kelvin and the RCM simulation with $\alpha = 3.0$. The experimental data is selected from the whole frequency range ($N = 1$), i.e. 3.75 ~ 5.5 GHz for the full-scale cavity and 75 ~ 110 GHz for the miniature cavity.	84
4.7	Comparison of the probability density function (PDF) for the imaginary part of the normalized impedance ξ_{12} and ξ_{21} between the full-scale cavity (solid line based on data) and the miniature cavity (dotted line based on data) for three different frequency bands (of the full-scale cavity) at different temperatures (of the scaled cavity). Top row shows the PDFs in linear scale while the bottom row shows the same PDFs in log scale. (a) $\alpha = 2.83$ within [4.45, 4.625] GHz at 130 Kelvin, (b) $\alpha = 4.19$ within [4.975, 5.15] GHz at 217 Kelvin and (c) $\alpha = 5.82$ within [5.325, 5.5] GHz at 297 Kelvin. Notice that in each plot, all four curves collapse into one because they match each other very well.	85

4.8	The comparison of all 8 PDFs for the normalized impedances, the real and imaginary part of ξ_{11} , ξ_{12} , ξ_{21} and ξ_{22} , for the full-scale cavity with 1/4 absorber and the miniature cavity. The experimental data are selected from [5.325, 5.5] GHz, the 10 th segment of the $N = 10$ frequency segments, for the full-scale cavity and is selected from 297 Kelvin and [106.5, 110] GHz for the miniature cavity.	87
4.9	The comparison of all 8 PDFs for the normalized impedances, the real and imaginary part of ξ_{11} , ξ_{12} , ξ_{21} and ξ_{22} , for the full-scale cavity with 1/4 absorber and the miniature cavity. The experimental data are selected from [4.275, 4.45] GHz, the 4 th segment of the $N = 10$ frequency segments, for the full-scale cavity and is selected from 90.1 Kelvin and [85.5, 89] GHz for the miniature cavity.	88
4.10	The distribution functions of the real (solid line) and the imaginary (dotted line) part of the normalized impedance ξ_{12} calculated from the RCM simulation for various α . The real and the imaginary part distribution functions are identical when $\alpha = 8$ but start to differ when $\alpha = 5$ and lower.	90
5.1	The complete computer 3D model for the multiple interconnected scaled cavity experiment setup. The details of each component visible here are discussed below.	94
5.2	Scaled interconnected cavity design with aperture, antenna mounting hole and mounting screws.	96
5.3	Cross section of copper box wall showing the antenna mounting arrangement. The antenna is mounted to the box with an adapter plate. Concealed PEM studs are used to avoid having protruding screws or nuts in the box interior.	97
5.4	One scaled cavity with two antenna installed is mounted on the central plate. Notice that the aperture is covered up since this is a single cavity configuration.	98
5.5	The 3D models of one unit box with different insert configurations. Insert plates, shown in the upper right, can have two apertures (allowing the box to be coupled with two other boxes), one aperture (allowing the box to be coupled with another box as the end of a cascading chain of boxes) or no aperture at all (for a single cavity configuration).	99
5.6	3D model for a 3-cavity cascade setup. 3 unit boxes are mounted to opposite side of the center plate, connected through the apertures to form a cascade. Electromagnetic waves come in from a receiving antenna, passes through all 3 boxes in the cascade and go out through the other antenna.	101
5.7	Center plate model with apertures and clear screw holes. The notch at the top of the plate is to accommodate the antenna and lens. . . .	102
5.8	Perturber assembly 3D model.	104
5.9	Perturber assembly.	105

5.10	Another view of a 3-cavity cascade setup. The 1X3 opening, the lens and antenna are aligned with the cryostat window to ensure maximum transmission of mm-waves. The grid of small green slots are for rotating gears (shown as red gears in upper right figure) to rotate magnetically coupled perturbers inside the cavity. A special plate can be installed within the 1X3 opening to mount gear if needed.	106
5.11	Antenna adapter model. An adapter plate (rectangular blue plate) is required to mount the antenna (blue cone) and the lens holder (green) onto the cavity (red box). The antenna and lens can be installed onto the adapter plate first, as shown in the upper left figure. Then the adapter plate is mounted onto the cavity by PEM studs (small red cylinder in upper left figure), which do not require screw holes or any protrusion into the cavity.	108
5.12	Stepper motor mounting location.	109
5.13	Smooth mirror-like finish from sheet copper. The part comes with a protective plastic film that can be peeled away to reveal the metal surface that is free of milling marks.	114
5.14	A side by side comparison for a 3-cavity cascade setup with the scaled-down cavities on left and full scale cavities on the right. Figure 6 in [9]	116
5.15	Comparison of the PDF of the induced voltage on a 50 Ohm load attached to the last cavity between the scaled cavity cascade and its full-scale counterpart. Figure 4 in [9].	118
6.1	Calculation of a brief synthetic sona from four simple orbits in a representative 2D 1/4-bow-tie billiard. We first calculate a scaled and time-delayed version of the input signal, which is a Gaussian pulse modulation of a 7 GHz carrier signal in this example. These waveforms are summed to obtain the synthetic sona shown at the bottom. The two ports are 17.5 cm apart.	125
6.2	(a) Physically measured sona, and (c) synthetic sona signal calculated from orbits less than 4 m ($= 10\sqrt{A}$) in length, and their time reversal reconstruction signals, (b) and (d), respectively. Only the upper half of the signals are plotted since they are essentially symmetric about the time-axis. The upper inset shows closeups of the initial Gaussian pulse (left, blue), the measured sona reconstruction (middle, green) and the synthetic sona reconstruction (right, red). The bottom inset plots some of the orbits used to calculate the synthetic sona. The horizontal and vertical straight walls of the billiard have lengths of 43.18 cm and 21.59 cm, and the two ports are 17.5 cm apart.	128

6.3	Measured signals in cut-circle cavity in the measured sona time-reversal process. The sona signal in the cavity normal (green, shorter in time) and superconducting (blue, longer in time) states, and time-reversal reconstruction in the cavity normal (cyan, lower amplitude) and superconducting (red, higher amplitude) states. The sonas are generated by injection of a Gaussian pulse with $6\sigma_t = 3\text{ns}$, modulating a 7 GHz carrier signal. Data is taken at 6.4 K (superconducting state) and room temperature (normal state).	133
6.4	Reconstruction quality (V_{pp} and focus ratio) and $ S_{21} ^2$ statistics (μ and σ_n) measured in the 1/4-bowtie billiard as a function of carrier frequency: (a) (b) when no noise is added; (c) (d) when 2mV Gaussian random noise is added to the sonas and reconstructions. (a) (c) use the physically measured sona method, while (b) (d) use the synthetic sona method. All quantities are plotted normalized to their maximum values.	137
6.5	Normalized reconstruction quality (normalized to its saturation value) for the physically measured and synthetic sona methods when a windowing function is applied to the sona before being time reversed, so that only the beginning part of the sona is used for the time backward step. The peak-to-peak voltage of the reconstruction is shown in (a) while the focus ratio is shown in (b). “MEA” and “SYN” refer to the physically measured and synthetic sona methods, respectively. “insert1” and “insert2” are two variations of the bowtie cavity geometry when inserts are added, as shown in the inset.	140
7.1	Figure 1 in Ref. [10]. BMW as a photonic topological insulator. (a) Schematic of the BMW. Part of the top metal plate is removed to reveal the bed-of-nails structure below. The enlarged regions on the right illustrate the origin of the bianisotropic response. Right inset: an equivalent way to produce bianisotropy by adding an asymmetrically placed metallic volume (washer) around the rod. (b) PBS of spin-degenerate metawaveguide with TE and TM modes forming doubly degenerate Dirac cones at K points. (c) Field profiles of the degenerate TE and TM mode at the K point. Colors: energy density. Arrows: electric field for the TM mode and magnetic field for the TE mode. Yellow dashed line: metallic border. (d) PBS with the band gap induced by the bianisotropy of the metawaveguide. Dashed lines in (b) and (d): TE and TM bands of interest.	148
7.2	(a): Numerically calculated band structure of the waveguide, where four edge modes have been labeled. (b) to (e): Field profile $ H_x - iH_y $ of the four edge modes at 6.13GHz (shown in (a) as a dashed line). It is clear that only the two spin-up states (from the two valleys), but none of the spin-down states, can be excited by a right circularly polarized magnetic dipole.	149

7.3	(a) Schematic of the experimental setup. Δ_{em} is the bianisotropy coefficient [10] and the interface is defined by the boundary of the two regions with Δ_{em} of opposite sign, denoted by a red dashed line. (b) Photograph of the top of the BMW structure showing the corresponding elements in (a). The inset shows the arrangement of the two loop coils which are in the air gap of a cylinder at the interface.	150
7.4	Transmission amplitude at the (a) left and (b) right side of the BMW interface as a function of frequency while varying the phase difference ϕ of the two driving loop antennas. The probe is positioned at the center of the edge. The BMW bulk band gap extends from 5.80 GHz to 6.47 GHz, as shown with the vertical dashed lines.	152
7.5	Simulated BMW structure with TPSW-supporting interface in CST with 16 period long and 8 period wide graphene-like lattice structure of rods. The two loops making up the rotating magnetic dipole antenna are perpendicularly placed with two independent driving coaxial cable inputs.	154
7.6	CST simulation results for transmission amplitude to the left and right side of the BMW structure while varying both the phase difference ϕ and driving amplitude (parameterized by angle $\theta \in [0, \pi/2]$) of the two loop antennas. Results are shown for (a) left, (b) right 6.47 GHz and (c) left, (d) right 6.08 GHz.	155
7.7	Transmission amplitude to the (a) left and (b) right side when varying both the phase difference ϕ and the input power (parameterized by θ) of the two loop antennas as deduced from the data at a frequency of 6.38 GHz. To examine the directivity, we plot the ratio of (c) left to right side and (d) right to left side transmission amplitude (in dB) as a function of θ and ϕ	157

List of Abbreviations

α	Alpha. The dimensionless loss parameter in Random Coupling Model
ξ	The normalized impedance. Sometimes also denoted as \mathbf{z}
\mathbf{z}	The normalized impedance. Sometimes also denoted as ξ
\mathbf{Z}_{cav}	Measured cavity impedance
\mathbf{Z}_{avg}	Ensemble average of \mathbf{Z}_{cav}
\mathbf{Z}_{rad}	Radiation impedance of the antennas, or ports
\mathbf{Z}_{ant}	Input impedance of the antennas, or ports
	\mathbf{Z}_{ant} includes both \mathbf{Z}_{rad} and the antenna's internal loss and delays
BMW	Bi-anisotropic Meta-Waveguide
BTRS	Broken Time Reversal Symmetry
CNAM	Center for Nanophysics and Advanced Materials
CST	Computer Simulation Technology, a numerical simulation software
FDTD	Finite-Difference Time-Domain
IACS	International Annealed Copper Standard
IREAP	Institute for Research in Electronics and Applied Physics
LCP	Left Circularly Polarized
NRL	Naval Research Laboratory
OFHC	Oxygen-Free High Conductivity
ONR	Office of Naval Research
QHE	Quantum Hall Effect
QSH	Quantum Spin Hall
RCM	Random Coupling Model
RCP	Right Circularly Polarized
RMT	Random Matrix Theory
TE	Transverse Electric
TM	Transverse Magnetic
TPSW	Topologically Protected Surface Wave
TRS	Time Reversal Symmetry
VDI	Virginia Diodes Inc
VNA	Vector Network Analyzer

Chapter 1: Introduction and Overview

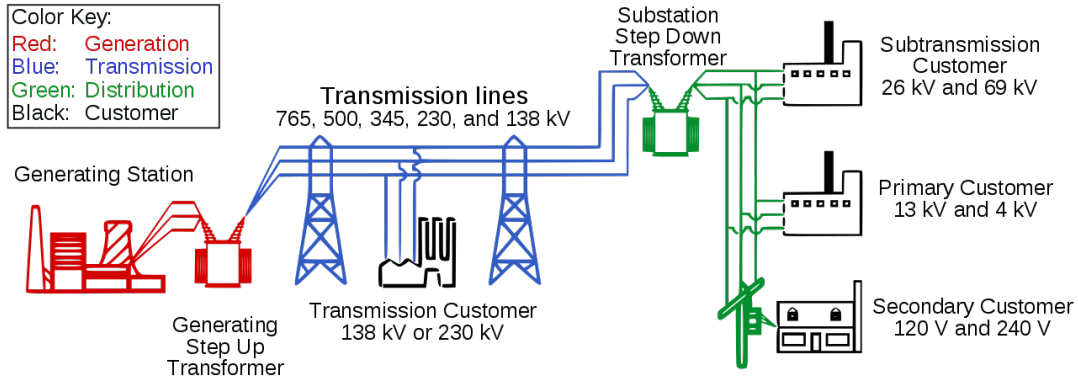


Figure 1.1: Diagram of an electric power system; transmission system is in blue. [1]

1.1 Background

Wave propagation in various complex media is an interesting and practical field that has a huge impact in our daily life. One basic type of wave propagation is guided waves through carefully engineered and manufactured media, such as waveguides and transmission lines. For example, high frequency electromagnetic waves carrying encoded information in optical fibers can travel vast distances in seconds, providing the backbone of internet that connects the world. As another example, electric power transmission relies on a mesh of transmission lines to transfer electric power generated from power plants to users across the globe, providing the crucial infrastructure of modern society.

Over the decades, research and engineering efforts has been made to optimize wave propagation properties in such media to better suit our needs. The most commonly seen highly-engineered wave propagation medium in our daily life is probably the optical fiber, a widely used waveguide to transmit light over long distances for high bandwidth communication. In this case, we want to have lower insertion loss

such that the signal quality can be maintained with less re-amplification [11–13], thus traversing longer distances without loss of signal fidelity. People also explored single-mode fiber vs. multi-mode fiber for different use cases considering the travel distance and bandwidth, invented new materials to achieve better properties compared with the conventional silicon dioxide, or even to acquire entirely new novel properties [14–17].

Another common type of wave propagation is in a confined medium, such as inside a room, a building or in general any partially open enclosure. Its applications includes telecommunication, sensors and wireless power transfer. One major difference with guided waves is that we typically do not try to control the details of the enclosure, which makes sense since we would like our WIFI to work regardless of which room I am standing in and what objects are placed around. Instead, we are interested in the generic statistical properties of the wave transmission in enclosures categorized by generic properties, such as the volume or the material making up the walls, as opposed to the exact shape or other specific conditions.

1.2 Thesis Overview

In this thesis, I study both of the above two types of wave propagation with experimentation and compare them with simulation and theoretical results.

For wave propagation within enclosures, we measured the transmission properties of electromagnetic waves inside metal cavities, launching and receiving microwave signals through antennas mounted on the cavity walls. To imitate the

propagation of microwave signals used in telecommunication frequency ranges (typically $1 \sim 6$ GHz) inside a typical building, we scaled down an otherwise enormous metal structure spanning several rooms into small metal boxes that could be managed, configured and integrated into our experimental setup. In this thesis, I discuss the practical challenges of scaling down the cavities in Chapter 2, explore the properties of the antenna on the transmission measurements in Chapter 3, verify my experimental methodology with a single cavity setup in Chapter 4, then applied it on a more complex multiple connected cavities setup in Chapter 5.

Although it is mentioned above that our focus is on the cavity's statistical properties, which are independent of the exact geometric details, it is nevertheless interesting to explore what we could achieve if the geometric information of the cavity boundaries is known. Specifically, we'd like to see if we could construct a signal based on the geometry information alone and broadcast it from one antenna to another such that it would focus in space and time at the second antenna. At first glance, the geometric information seems simple to obtain. After all, we manufactured all the cavities according to our own design specifications. However, the actual geometry could vary with lots of uncontrollable factors, e.g. room temperature changing the volume of the cavities, warping of the cavity walls, differences in surface condition due to dust, oil, or other residues, etc. So the effectiveness of our constructed signal decreases as it bounces off the cavity walls more and more as it travels. We discuss our findings in Chapter 6.

Finally, as a case study for guided wave propagation, we looked into the emerging new type of materials, photonic topological insulators, which are an interesting

class of materials whose photonic band structure can have a band-gap in the bulk while supporting topologically protected unidirectional edge modes. In Chapter 7, we performed experiments on a 2D waveguide composed of hexagonal graphene-like lattice. The resulting electromagnetic waves traveled from the source antenna, along the waveguide, to the two sides in a reflectionless manner, i.e. there's no reflection or back scattering of waves.

But before we delve into the topics in this thesis, there are some fundamental theories and prior work that need to be discussed first.

1.3 Ray-chaotic Cavities

The property of waves coupling into and propagating inside an electrically large complex enclosure is of interest to several fields. In electromagnetic compatibility (EMC) the goal is to minimize the coupling by providing better shielding and thus lower the chance of a larger induced voltage on sensitive devices located inside the enclosure, thus minimizing potential damage. In telecommunications one would like to maximize the coupling and the induced voltage to boost up the transmitted signal inside an enclosure, which could be a room with windows and doors. These enclosures are modeled as ray-chaotic cavities, where waves are very sensitive to geometry details and small changes, which is the case for most real life situations. Thus a statistical description is more approachable and applicable than trying to calculate an exact solution of the problem. In light of this, the Random Coupling Model (RCM) was introduced by Zhang et al., as a method to predict the statistical dis-

tribution of the induced voltages at locations inside a ray-chaotic enclosure [18, 19]. It combines the universal predictions from Random Matrix Theory (RMT), briefly introduced below in section 1.4, and the system-specific properties characterized by the system's port radiation impedances.

Complex enclosures, such as computer cases with circuitry inside, or offices filled with desks, chairs, and electronics, are examples of ray-chaotic systems. To define what we mean by ray-chaotic, consider the case where the wavelength is short and a ray description is appropriate. Consider two rays starting from the same location in such an enclosure but with slightly different directions. As the rays propagate, reflecting from either curved surfaces or the interior features of the enclosure, their separation will tend to increase exponentially in time, and we call such a situation ray-chaotic. Ray chaos leads to an extreme sensitivity to initial conditions for the rays [20]. For waves propagating in highly over-moded ray-chaotic structures, the exact solution for the fields depends strongly on the geometric details of the structure and is very sensitive to small changes in frequency or geometry. Thus, in the presence of even small uncertainties in structure or frequency, a statistical approach may be more appropriate than trying to obtain an exact solution for field quantities inside the structure [21]. The Random Coupling Model (RCM) is one such method to predict the statistical properties of the waves inside a ray-chaotic enclosure [18, 19]. The RCM has been widely discussed and tested over the years, with good agreement between theory and experimental results on individual complex structures [2, 3, 6, 7, 22–24]. It has also been used to study the effect of a non-linear port on the measured statistical electromagnetic properties of a ray-chaotic complex

enclosure in the short wavelength limit [25].

1.4 Random Matrix Theory

The RCM is based on Random Matrix Theory, originally proposed to model the energy level statistics of heavy nuclei [26]. The idea is that if the wave system is sufficiently complex then its fluctuating properties have the same statistics as those of a suitable ensemble of random matrices [27] (hence the name "Random Matrix Theory"). Certain statistical properties, such as the distribution of the normalized spacings between nearest neighbor eigenfrequencies (ϵ), follow a universal behavior regardless of the system details. The type of random matrix is chosen according to the general symmetry of the system in order to correctly represent its dynamics. For instance, the Gaussian Orthogonal Ensemble (GOE) describes systems with Time-Reversal Symmetry and the Gaussian Unitary Ensemble (GUE) describes systems with Broken Time-Reversal Symmetry. It is later conjectured [26, 28–32], and validated in some cases [27, 33–35], that most wave-chaotic systems follow random matrix statistics for a properly chosen ensemble, giving Random Matrix Theory a broad range of applications.

1.4.1 Random Matrices

Random Matrices are matrices whose elements are random variables. If we take one realization for each of the random variables and group them together as a matrix, then we get one realization of the random matrix. Taking many such realizations is

called an ensemble. The two random matrices relevant to electromagnetic systems are Gaussian Orthogonal Ensemble (GOE) and Gaussian Unitary Ensemble (GUE) corresponding to systems with Time-Reversal Symmetry (TRS) and Broken Time-Reversal Symmetry (BTRS) respectively.

- For a GOE matrix, each element, $X_{i,j}$, is a real independent-identically-distributed (i.i.d) Gaussian random variable with zero mean. All the off-diagonal elements have a variance of $1/2$ while the diagonal ones have a variance of 1 , i.e. $X_{i,j} \sim N(0, \frac{1}{2})$ for $i \neq j$ and $X_{i,i} \sim N(0, 1)$.
- For a GUE matrix; It is a Hermitian matrix with real diagonal elements and complex off-diagonal elements. Each diagonal element is a real i.i.d Gaussian random variable with zero mean and unit variance, i.e. $X_{i,i} \sim N(0, 1)$. The off-diagonal elements are complex with real and imaginary parts both being i.i.d Gaussian random variable with zero mean and $1/2$ variance, i.e $X_{i,j} \sim N(0, \frac{1}{2}) + iN(0, \frac{1}{2})$ for $i < j$.

Once an appropriate random matrix is constructed, its eigenvalues can be calculated and then used to study the statistical properties of the corresponding wave-chaotic system, such as the normalized spacings between the nearest eigenfrequencies.

1.4.2 Normalized Spacings Between The Nearest Eigenfrequencies

In the case of electromagnetics, the normalized spacings between the nearest eigenfrequencies is defined as $\epsilon = (k_{n+1}^2 - k_n^2)/(\Delta k_n^2)$ where k_n is the n^{th} eigenfrequency's wavenumber, and $\Delta k_n^2 = \langle k_{n+1}^2 - k_n^2 \rangle$ is the mean spacing between eigenlevels. For

a given enclosure whose size is much larger than the wavelength, the mean spacing can be calculated as

$$\Delta k_n^2 \cong 4\pi/A \quad (2D) \tag{1.1}$$

$$\cong 2\pi^2/(kV) \quad (3D)$$

where A and V are the area and volume of the 2D or 3D cavity. Then according to the RMT, the probability density function (PDF) of ϵ for different enclosures follows one of the two universal curves, depending on whether the system has Time Reversal Symmetry (TRS) or Broken Time Reversal Symmetry (BTRS):

$$P(\epsilon) \cong \frac{\pi}{2} \epsilon e^{-\pi\epsilon^2/4} \quad (\text{TRS}) \tag{1.2}$$

$$\cong \frac{32}{\pi^2} \epsilon^2 e^{-4\epsilon^2/\pi} \quad (\text{BTRS})$$

These are called ‘‘Wigner distributions’’ and they are proven to be applicable to various wave-chaotic systems. Note that $P(0) = 0$ in both cases, meaning that all degeneracies are broken in pure RMT systems.

1.5 Random Coupling Model

Random Matrix Theory (RMT) provides a universal statistical prediction for the generic properties of wave-chaotic systems, however it is difficult to identify these universal statistical properties in experimentally measured data because it inevitably contains system-specific features like the coupling between the ports and the cavity modes and short orbits [36–38]. The Random Coupling Model (RCM) introduces a framework to incorporate the non-universal features with the universal statistical

properties of appropriate random matrices to reproduce in the statistical sense the experimentally measured cavity impedance matrices. The effect of uniformly distributed loss in the system is to create a sub-unitary scattering system [39], and this effect is captured to very good approximation by a single loss parameter α [18, 19]. The RCM is formulated in terms of the impedance matrix \mathbf{Z} of an N -port system in analogy to the reaction matrix in nuclear scattering theory [40–45]. The ports represent sources or sinks of radiation that introduce or absorb energy in the enclosure. The impedance relates the voltage induced on one port to the currents at all of the N ports, and is simply related to the $N \times N$ scattering matrix \mathbf{S} through a bilinear transformation $\mathbf{S} = \mathbf{Z}_0^{1/2}(\mathbf{Z} + \mathbf{Z}_0)^{-1}(\mathbf{Z} - \mathbf{Z}_0)\mathbf{Z}_0^{-1/2}$, where \mathbf{Z}_0 is a diagonal real matrix whose elements are the characteristic impedance of the transmission line modes connected to each port.

Similar to RMT, the loss parameter α defines the universal statistical property of the normalized impedance matrix, \mathbf{z} (sometimes also denoted as $\boldsymbol{\xi}$), which is a key parameter to describe any electromagnetic enclosure. α is defined as $\alpha = k^2/(\Delta k_n^2 Q)$ where Q is the unloaded cavity quality factor. If we plug in Equation (1.1) for 2D and 3D systems, α can be written as

$$\begin{aligned} \alpha &= \frac{k^2 A}{4\pi Q} \quad (2\text{D}) \\ &= \frac{k^3 V}{2\pi^2 Q} \quad (3\text{D}) \end{aligned} \tag{1.3}$$

1.5.1 S-parameters & Z-parameters

For an electromagnetic system, waves are coupled into or out of the system through ports. An N port passive electromagnetic network is usually described by a N -by- N scattering matrix \mathbf{S} (S-parameters) or impedance matrix \mathbf{Z} (Z-parameters), which are both well-established quantities in microwave engineering. The S-parameter element $S_{i,j}$ is the complex ratio of the amplitude and phase of the outgoing wave at port i to the amplitude and phase of the incoming wave at port j when only the j^{th} port has a nonzero incoming wave while all other ports are terminated with a matched reflectionless load, i.e. $S_{i,j} = \frac{b_i}{a_j}|_{a_m=0, m \neq j}$, where a_i, b_i are complex numbers representing the incoming and outgoing wave at port i respectively. Similarly, the Z-parameter element $Z_{i,j}$ is the ratio of the induced voltage at port i to the source current at port j when only the j^{th} port has nonzero source current, i.e. $Z_{i,j} = \frac{V_i}{I_j}|_{I_m=0, m \neq j}$, where V_i, I_i are the voltage and current at the i^{th} port respectively. In a typical microwave experiment, one uses a vector network analyzer to measure the cavity S-parameters, which can be converted into the cavity Z-parameters by

$$\mathbf{Z} = \mathbf{Z}_0^{1/2}(\mathbf{I} + \mathbf{S})(\mathbf{I} - \mathbf{S})^{-1}\mathbf{Z}_0^{1/2},$$

where \mathbf{I} is an identity matrix, \mathbf{Z}_0 is a diagonal matrix whose elements, $Z_{i,i}$, are the characteristic impedances of the transmission line connecting to the i^{th} port (typically 50 or 75 Ohms for a coaxial cable). To couple waves into or out of an enclosure, an antenna is required which usually presents an impedance mismatch

with the connected transmission line. The mismatch causes the incoming waves to partially reflect back and also prevents the antenna from picking up waves inside the enclosure efficiently. This is an inevitable system-specific feature that exists in almost all microwave experiments, resulting in a deviation from the expected RMT universal behavior when analyzing the experimental data.

1.5.2 Normalized Impedance

To remove the system-specific features, the Random Coupling Model uses a non-statistical impedance matrix, \mathbf{Z}_{avg} , which is obtained by averaging the measured cavity Z-parameters \mathbf{Z}_{cav} over many realizations, to characterize the system-specific properties and to normalize the experimental data. It is expected that the universal fluctuations cancel out in the ensemble average because $\langle \text{Re}[\mathbf{Z}] \rangle_{\text{realization}} = 1$ and $\langle \text{Im}[\mathbf{Z}] \rangle_{\text{realization}} = 0$. Realizations of the same cavity are created by perturbing the cavity modes while retaining the same cavity volume, usually by rotating a large irregularly-shaped metal panel. \mathbf{Z}_{avg} mainly includes the radiation impedances of the antennas which characterize the mismatch mentioned above, and it also includes the influence of non-statistical short orbits between the ports, as discussed in [38]. Once we obtain $\mathbf{Z}_{\text{avg}} = \langle \mathbf{Z}_{\text{cav}} \rangle_{\text{realizations}}$, the RCM suggests normalizing the measured \mathbf{Z}_{cav} by

$$\boldsymbol{\xi} = (\text{Re}[\mathbf{Z}_{\text{avg}}])^{-1/2} (\mathbf{Z}_{\text{cav}} - j\text{Im}[\mathbf{Z}_{\text{avg}}]) (\text{Re}[\mathbf{Z}_{\text{avg}}])^{-1/2} \quad (1.4)$$

This quantity $\boldsymbol{\xi}$, sometimes also simply called \mathbf{z} in some papers, is expected to have the statistical properties predicted by RMT for some value of loss parameter α .

1.5.3 Loss Parameter α

Similar to Random Matrix Theory, the statistics of the normalized impedance ξ follows a universal curve defined by the loss parameter α , which can be calculated according to Equation (1.3). Figure 1.2 (which is Figure 2.3 in [2]) illustrates the statistics of ξ for a one-port system with different α values. The statistics are not calculated by traditional electromagnetic simulations that solve Maxwell's equations inside a particular enclosure. Instead, the statistics are obtained by Monte Carlo simulations by constructing many random matrices following RMT, and examining their statistics. In practice, it is usually difficult to obtain an accurate estimate for the unloaded quality factor of the cavity, thus alternative methods are employed to determine α .

For example, in the high loss regime ($\alpha > 5$), the variance of the normalized impedance can be expressed as

$$\begin{aligned} \sigma_{\text{Re}[\xi]}^2 &\approx \sigma_{\text{Im}[\xi]}^2 \cong \frac{1}{2\pi\alpha} && \text{(BTRS)} \\ &\cong \frac{1}{\pi\alpha} && \text{(TRS)} \end{aligned} \tag{1.5}$$

Hence, one can conduct experiments to measure \mathbf{Z}_{cav} for many realizations, normalize them to get ξ then use Equation (1.5) to calculate α . More generally, α can always be determined by finding the universal curve defined by α that best fit the statistics of ξ , which is obtained through experiment. The universal impedance statistics curves only depend on α values and can be calculated by methods presented in [2] Chapter 2.5.

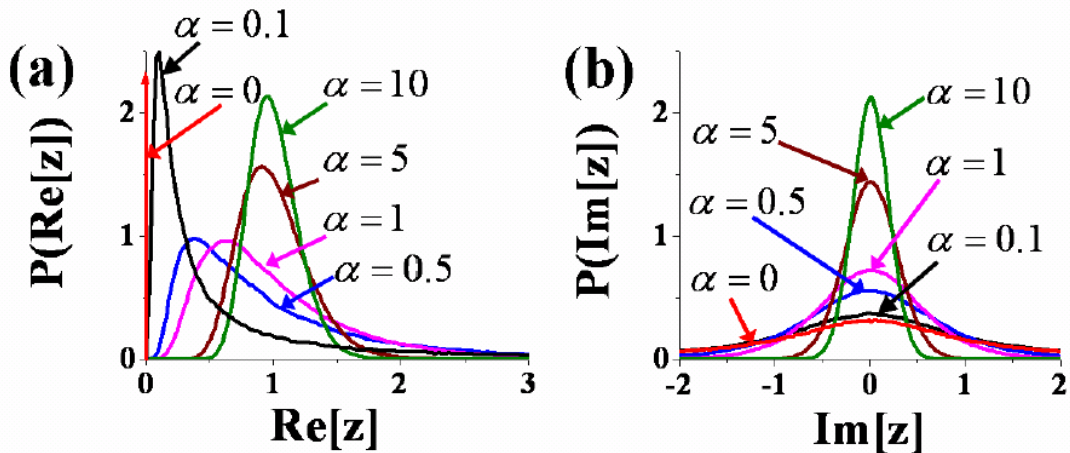


Figure 1.2: Random Matrix Theory predictions for the Probability Density Functions of (a) $\text{Re}[z]$ and (b) $\text{Im}[z]$ as a function of increasing α , for a one-port time-reversal symmetric wave-chaotic cavity. Figure 2.3 in Ref. [2].

A complete list of methods to estimate cavity α is presented in Ref. [2] Appendix B.

1.5.4 Extensions of RCM

The RCM provides a framework to analyze the statistical properties of wave-chaotic systems, taking into account the universal properties, the loss parameter α , and the system-specific properties. However, it only covers single-cavity linear systems. In real life scenarios, this means that RCM can be used to study the wave properties inside, say, a room, but it requires additional steps to study interconnected cavities, such as the floor of a building consisting of multiple rooms connected with doors and hall ways, with each room potentially having its own unique geometry and properties. In Chapter 5, we look into this case by extending RCM to model multiple connected cavities.

There are also situations where nonlinear behavior is added to the mix, for

example when an amplifier or p/n junction-based electronics is present in the room. Nonlinearity adds complexity to the system, making the modeling of the system more difficult, but is nevertheless an interesting property that often opens avenues for novel applications not only in electromagnetic waves [46], but also in other areas such as elastic waves [47] and gravity waves [48]. Extending RCM into nonlinear systems, Min Zhou added an active nonlinear circuit which generates strong second harmonic waves into a quasi-2D wave-chaotic billiard in [49]. The study showed that the statistics of the harmonics can be predicted by modeling the nonlinear cavity as two cascaded linear cavities connected by a nonlinear circuit.

Chapter 2: Testing The Random Coupling Model Predictions in a
Scaled-Down Cavity With Remote Injection Setup

There is interest in using the RCM to understand the wave properties of more complex structures, such as a cascade or a network of coupled cavities [50, 51]. It becomes increasingly difficult to experimentally test these structures due to their large size and the difficulty in managing and reconfiguring them in a typical laboratory environment. To solve this problem, we propose miniaturizing the complex structure while maintaining the statistical properties of the waves by carefully scaling the frequency and the quality factor of the system. Electromagnetic geometric scale modeling has been used extensively in simulations and modeling of large structures for decades [52–54]. It is also routinely done in other fields such as ship model testing [55] and wind tunnel testing [56] where a miniature model is constructed and studied for design verification. The idea of scaling down the geometric size is not new in modeling, but the challenge is to make other electromagnetic properties scale appropriately as well.

In Chapter 2, we discuss the practical challenges of testing the theory in experiment, explain how the scaled cavity setup works and introduce the experimental setup. In order to analyze the experimental data, we need to modify the RCM to accommodate the case with lossy ports, which is discussed in Chapter 3. Then in Chapter 4 we validate this setup by comparing the single miniature cavity result with the single full-scale cavity result obtained by our collaborators at the Naval Research Laboratory (NRL). Finally we expand the setup to have multiple cavities coupled through apertures, and present the experimental result in Chapter 5

2.1 The Need For Scaled Cavities

Many RCM predictions have been successfully tested in experiments and it is still expanding to include more complex scenarios. In this project, we are interested in the RCM prediction for connected cavities, as discussed in [3,24]. A chain of coupled ray-chaotic cavities represents many common situations, such as the compartments in a ship and offices and hallways in a building. RCM predicts the statistics of the induced voltages for ports located in each cavity along the chain as a function of the loss and the coupling. Figure 2.1 shows the predicted ratio of the power coupled into the N^{th} cavity over the power coupled into the first cavity, as a function of N for serially connected $\alpha = 6$ cavities. However this theoretical result is hard to verify in experiment since it requires a huge space to host the connected cavities, and many decades of dynamic range of microwave power measurement. The previous experimental setup for a single over-moded cavity with volume $V \approx (20\lambda)^3$ is about 1m^3 and it would be difficult to fit in even a few cavities in the limited university lab space. Hence we introduced a scaled cavity experiment setup that can host a chain of cavities with total volume $V \approx (450\lambda)^3$. The basic idea is to scale down the cavity size and, in order to keep Maxwell's equations unchanged, scale up the frequency of the electromagnetic waves and conductivity of the cavity walls. We'll discuss the details of the scaling in Section 2.2, its implementation in Section 2.3 and present a series of progressive experiments to help understand and test the operation of this setup.

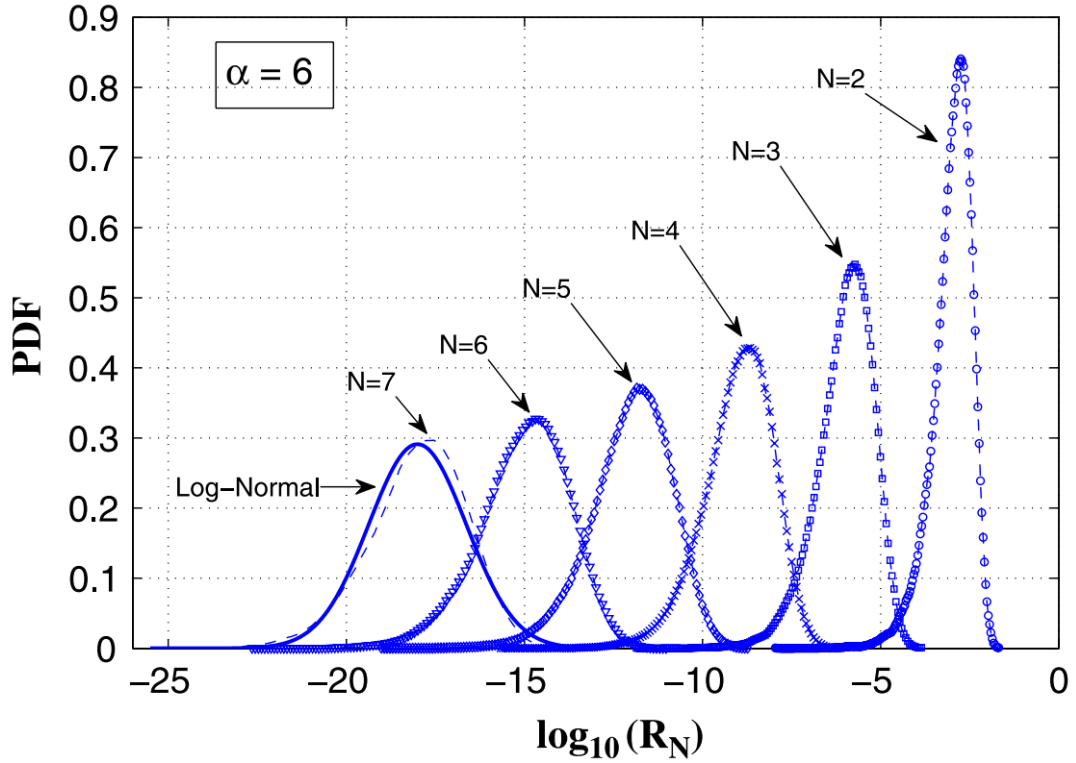


Figure 2.1: RCM-predicted probability density function of power ratios $R_N(\alpha = 6) \equiv P_{in}^{(N)}/P_{in}^{(1)}$ for chains of up to seven cavities: the high-loss regime is assumed for all the (statistically identical) cavities in the chain. This is Figure 7 in Ref. [3].

2.2 Scaling of The Cavity

The main purpose of the scaling is to shrink the cavities down in linear size by a factor of s , i.e. $V' = V/s^3$, and create a scaled-down-in-size version with the same statistical electromagnetic properties. Note that each individual mode in the full scale enclosure will not be reproduced precisely in the miniature version. Instead, the statistical properties should be identical before and after the scaling. We are targeting scaling factors of $s = 20$ and $s = 40$. We would also like to make this a manageable, reconfigurable and extendable experimental setup. In this section, we will discuss the necessary scaling of the frequency and cavity wall conductivity in order to maintain the same α value, and thus the same statistical properties.

2.2.1 Frequency Scaling

The need for frequency scaling is obvious: when the cavity is scaled down in size by a factor of s the wavelength must also scale down by s in order for the cavity to remain the same electrical size. If volume is scaled down to $V' = V/s^3$ and $V = (N\lambda)^3$, we need $V' = (N\lambda')^3$, where λ and λ' are the wavelength before and after the scaling respectively. Thus wavelength is scaled down by s , $\lambda' = \lambda/s$, and the frequency $f = c/\lambda$ is scaled up by s .

Frequency scaling can be achieved by using frequency extenders which are frequency multipliers that convert signals from $0 \sim 10$ GHz (microwave) to the several hundred GHz range (mm-wave). After scattering, the signals are received and then mixed down to $0 \sim 10$ GHz so that they can be measured by a microwave

Vector Network Analyzer (VNA). The proposed setup uses extenders that are in the range of 75 ~ 110 GHz (WR10 band) and 220 ~ 330 GHz (WR3.4 band), which correspond to the scaling of $s = 20$ from 3.75 ~ 5.5 GHz and $s = 40$ from 5.5 ~ 8.25 GHz.

2.2.2 Cavity Wall Conductivity Scaling

As stated in Equation (1.3), since $\alpha \propto k^3 V/Q$ must remain unchanged, and that $k^3 V$ remains the same for the given cavity, the quality factor Q must be the same as the full-scale cavity. The quality factor is defined in general as the ratio of the energy stored to the energy dissipated per cycle on resonance. When the wavelength is much smaller than the system size, the quality factor of an empty metallic enclosure with loss dominated by ohmic loss in the walls can be estimated as

$$Q \approx \frac{3 V}{2 S \delta},$$

where S is the wall surface area, $\delta = \sqrt{2/(\omega\mu\sigma)}$ is the skin depth in the local limit, and σ is the electrical conductivity.

δ is the depth that the electromagnetic waves can penetrate into the metal before the induced current screens out the incident wave. Ohmic loss within the skin depth is the main cause of energy loss in our cavities. In the local limit, the skin depth is related to the conductivity σ by $\delta = \sqrt{2/(\omega\mu\sigma)}$, where $\omega = 2\pi f$ is the angular frequency, μ is the magnetic permeability of the conductor. Putting this into the expression for Q and then putting Q into the expression for the RCM loss

parameter $\alpha \propto k^3 V/Q$, we have

$$\alpha \propto \frac{k^3 S}{\sqrt{\omega \mu \sigma}}. \quad (2.1)$$

If we only look at the scaling with respect to s , we can further apply $k \propto s$, $\omega \propto s$, $S \propto 1/s^2$, which leads to

$$\alpha \propto \frac{s^3(1/s^2)}{\sqrt{s\sigma}} = \sqrt{s/\sigma}. \quad (2.2)$$

Therefore, the conductivity of the wall must also be scaled by a factor of s in order to keep the RCM loss parameter α the same after the scaling. This is required to have the same fluctuating statistical properties in the scaled and un-scaled cavities.

In theory, the electrical resistance of a metal changes with temperature in two regimes [57]:

- At room temperature the change in resistance is proportional to the change in temperature: $\Delta R = R_0 \alpha_R \Delta T$, where ΔR is change in resistance, ΔT is change in temperature, R_0 is resistance at the reference temperature and α_R is the temperature coefficient of resistance (not to be confused with the loss parameter α in the Random Coupling Model). Typically a metal's resistance goes up as temperature goes up, i.e. α_R is positive, since collisions between vibrating atoms and conduction electrons happen more frequently.
- At low temperature the resistance is dominated by impurities or defects in the material and becomes almost constant with temperature.

In experiment, conductivity scaling can be achieved by a combination of meth-

ods:

- Cool down the cavity to low temperatures using a cryostat,
- Change the cavity wall material to a better conductor, such as from aluminum to Oxygen Free High Conductivity (OFHC) copper,
- Reduce surface roughness by physical polishing of the cavity interior surfaces.

First we put the metal cavity in a cryostat that can bring down the temperature to about 10 Kelvin. The electrical resistivity of aluminum ρ_{Al} vs. temperature is shown in Figure 2.2 (Figure 1 in [4]) with different samples and measurement techniques. It is clear that ρ_{Al} is decreasing as temperature goes down but the curve eventually saturates at some value $\rho_{\text{Al}}^{\text{sat}}$. The saturation value are different for different curves, which are the result of measuring different samples. In general, the higher the purity, the lower the $\rho_{\text{Al}}^{\text{sat}}$ value. So ideally by choosing a suitable aluminum material, we can achieve more than $s = 40$ scaling by cooling down to a certain low temperature, before reaching the superconducting transition of aluminum (which happens around 1.2 Kelvin).

During the cavity design, we discovered that commercially available aluminum may not have a high enough conductivity scaling range to match the $s = 40$ scaling, i.e. their $\rho_{\text{Al}}^{\text{sat}}$ value is not low enough. This is mainly due to the added impurities in the aluminum alloy that lead to higher $\rho_{\text{Al}}^{\text{sat}}$ but are required to maintain certain desirable mechanical properties. So instead of using aluminum as the cavity material, we chose OFHC copper which has a lower $\rho_{\text{Cu}}^{\text{sat}}$ value.

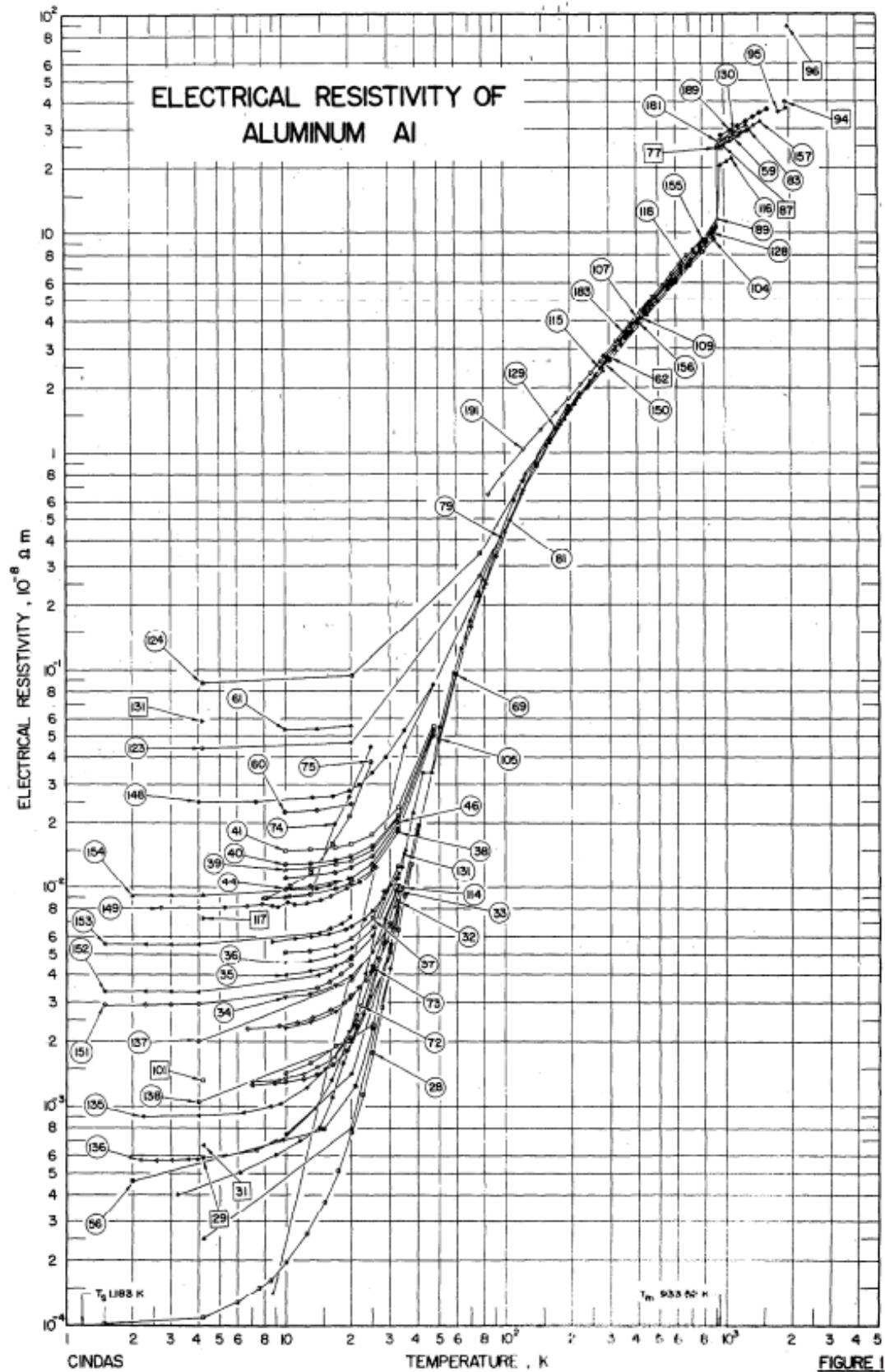


Figure 2.2: Electrical resistivity of copper vs. temperature. The different curves on the plot are the experimental results for different aluminum samples and were measured with different techniques at different times from 1908 to 1981. (which is Figure 1 in [4])

After changing to OFHC copper, it was found in experiment that the α value at the lowest temperature is still higher than what we expected, prompting more research into the factors that affect surface conductivity of metals. One simple method to increase the surface conductivity is to reduced surface roughness [58, 59] by physically polishing the inside walls of the cavity. The 5-sided rectangular cavity, or the cup, is milled out from a piece of bulk metal, leaving a milling pattern on the inside walls. Although the surface feels smooth the milling pattern indicates that there are micro-structures that increases surface roughness. If the surface roughness is at the scale of the skin depth, the microwave surface losses will be enhanced [58, 59]. After polishing it to a mirror finish, we observe a further decrease in the α value. An important constraint is that the polishing work is not at its best performance because it is difficult to put proper tools inside the solid 5-sided box. Thus in the future design of scaled cavities, it is best to start with a well-polished sheet metal and then fold it into a 5-sided cavity, which is the basis for my design for the multiple coupled cavities. The copper used in the 5-sided cavity is C10100 Oxygen-Free Electronic (OFE) copper, 99.99% pure copper with 0.0005% oxygen content and a minimum 101% IACS (International Annealed Copper Standard) conductivity rating. The copper used in the multiple-cavity design is C11000 Electrolytic-Tough-Pitch (ETP), the most common copper with 0.02% to 0.04% oxygen content and usually meets or exceeds the 101% IACS specification, and is mechanically polished to mirror-like finish.

With these three methods combined, we are able to reduced the α value from about 6.5, at room temperature for the miniature aluminum cavity, to about 2.8, at

the lowest temperature for the polished copper cavity. The comparison is shown in Figure 4.3

2.2.3 Scaling Limits

How far can we scale the cavities down in size? The current limiting factor for s to go beyond 40 is mostly the difficulty in further frequency scaling. As we will discuss in the following sections about the experimental setup, the corresponding frequency band for $s = 40$ is $220 \sim 330$ GHz, which is a very high frequency range for millimeter wave products such as frequency extenders, waveguides and horn antennas. Perhaps as millimeter-wave technology advances and matures, we could reach a scaling factor of 60, 80 or beyond.

Another issue with scaling with larger values of s is the need to increase the wall conductivity by even greater amounts in the scaled structure. This is certainly possible if we start with full-scale systems having large values of RCM loss parameter α , for example 10 and larger.

2.3 Experimental Setup

In our setup, we scale down a 66 cm by 122.5 cm by 127.5 cm aluminum “full-scale” cavity designed for the $3.7 \sim 5.5$ GHz range (WR187 band) by a factor of 20 in each dimension, i.e. $s = 20$. The scaled cavity is a rectangular box (6.375 cm X 6.125 cm X 3.300 cm with rounded corners) containing a perturber of irregular shape that can be rotated by motor control. The new (scaled) frequency range becomes

75 ~ 110 GHz (WR10 band), which can be measured by using a Keysight network analyzer (KT-N5242A 10 MHz to 26.5 GHz PNA-X) working together with two VDI frequency extenders (Tx/Rx WR10 module). To achieve higher Q , the miniature cavity is made of oxygen-free high-conductivity (OFHC) copper, with mechanically polished inner wall surface to reduce the surface resistance [58, 59]. We then use a custom-built BlueFors BF-XLD400 cryogen-free dilution refrigerator system, which can reach a base temperature of 10 mK under minimum heat-load conditions, to cool the cavity and further increase Q . The available volume for samples is a cylinder of 50 cm in diameter and 50 cm in height, that has a total volume of $V \approx (150\lambda)^3$ at 100 GHz, providing abundant space for larger structures.

The following sections describe the detail of the above experimental setup in four parts:

- Measurement system including a VNA and frequency extenders (2.3.1) to extend the frequency range of VNA from 26.5 GHz to 330 GHz.
- Cryostat to keep the sample in low temperature in order to achieve conductivity scaling (2.3.2).
- Free-space propagation path to inject the source signal (75 ~ 110 GHz or 220 ~ 330 GHz frequency range) into the sample cavity without direct waveguide connection (2.3.3), also called remote injection.
- Magnetically coupled mode stirrer powered by a cryogenic stepper motor to generate multiple realizations of the cavity by perturbing the cavity modes (2.3.4).

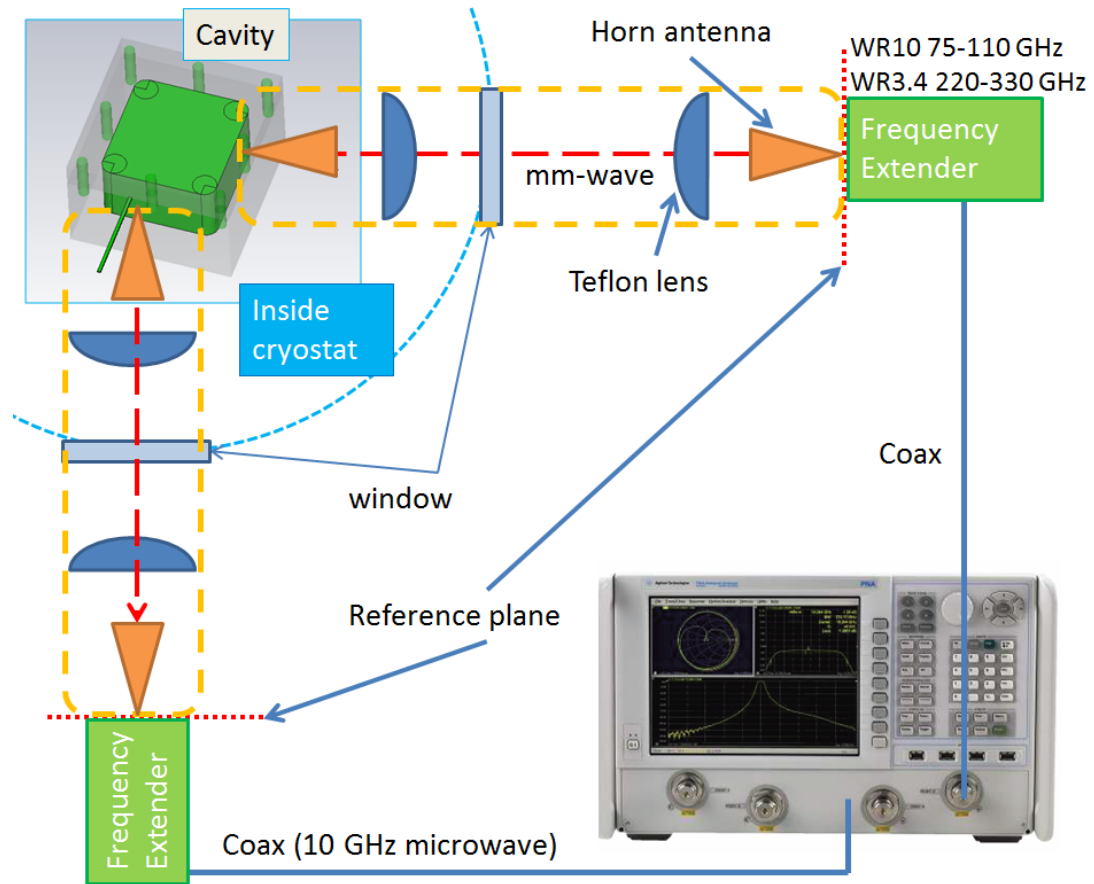


Figure 2.3: The schematics for the scaled cavity experiment setup.

The schematics of the setup is shown in Figure 2.3.

2.3.1 VNA & Extenders

As mentioned in Section 2.2.1, we need frequency extenders to up convert the VNA source signal from around 10 GHz to hundreds of GHz, and then down convert the transmitted signal for the VNA to measure. The VNA that we are using is a 4-port Keysight N5242A PNA-X, a high performance model that works up to 26.5 GHz. The frequency extenders are made by Virginia Diode Inc, models WR10TxRx and WR3.4TxRx, whose block diagram is shown in Figure 2.4 (Figure 1 in [5]). The

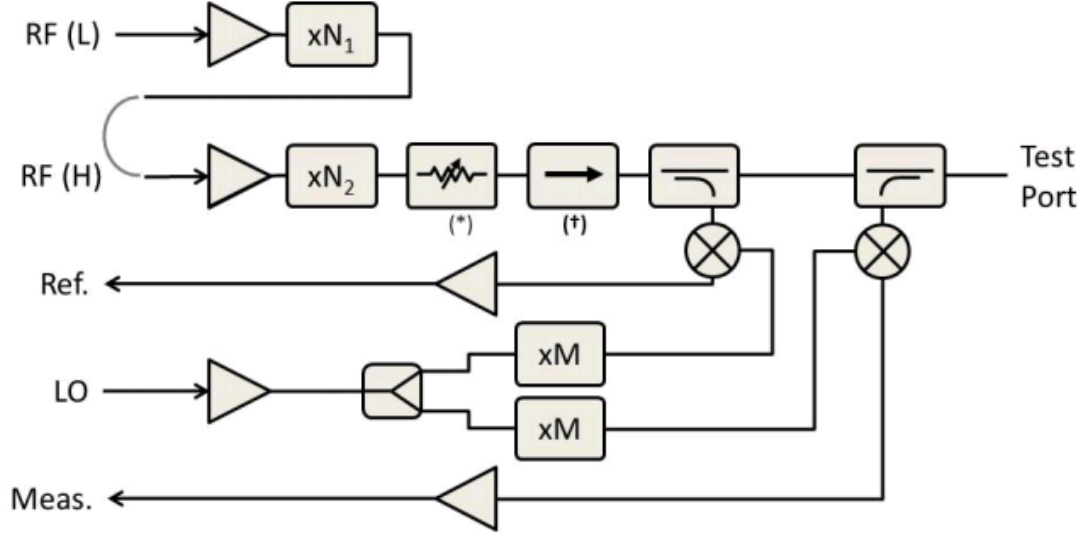


Figure 2.4: Block diagram for Virginia Diode Inc frequency extender modules. (*) Variable attenuator. (†) Isolator. Picture taken from VDI product manual [5].

“RF (L)” and “RF (H)” are input microwave signals generated by the VNA with relatively lower (L) or higher (H) frequency. The RF signal is first multiplied in frequency by a factor of N_2 (for “RF (H)” input) or N_1N_2 (for “RF (L)” input) and then attenuated and sent through an isolator to become the mm-wave input signal. A portion of the mm-wave signal is sampled out before sending to the test port, in order to be mixed down by the local oscillator (LO) signal, which is also multiplied in frequency by a factor of M . The resulting intermediate frequency (IF) $f_{\text{IF,Ref.}} = N_1N_2f_{\text{RF(L)}} \pm Mf_{\text{LO}}$ is in the range of 10 GHz, measurable by the VNA, and is measured at the “Ref.” port. The reflected mm-wave signal from the test port is sampled and mixed down in a similar fashion and is measured at the “Meas.” port. As discussed in Section 1.5 the S-parameters are complex ratios of amplitudes of the outgoing waves, measured at the “Meas.” port, to the incident waves, measured at the “Ref.” port.

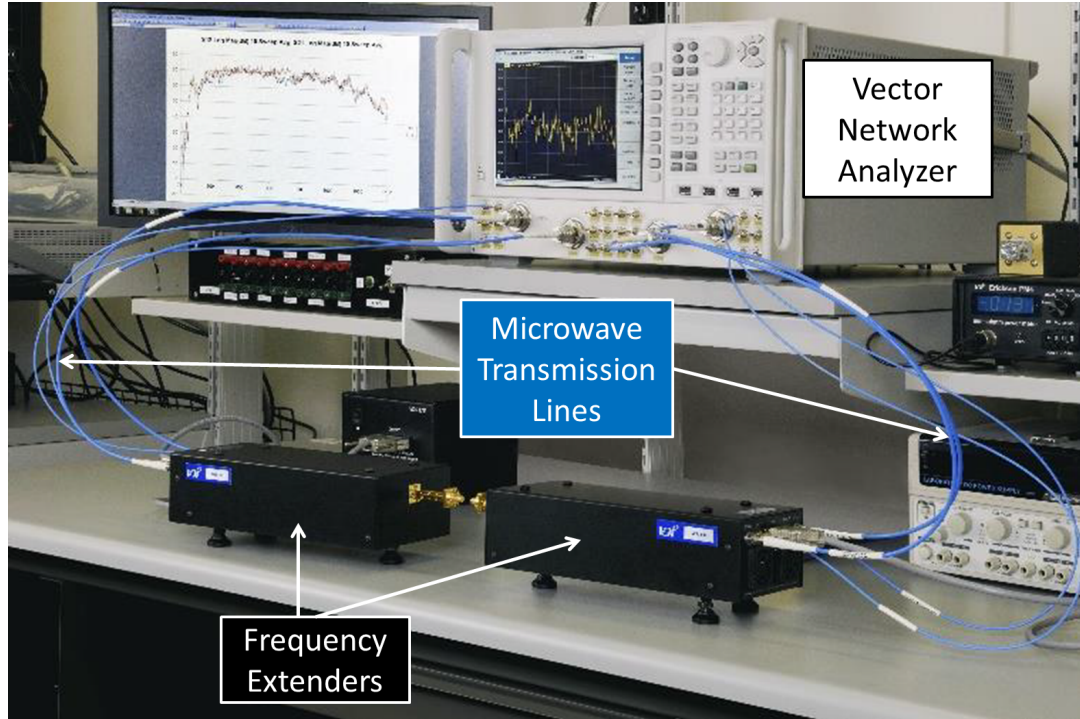


Figure 2.5: A typical setup with VNA and VDI extenders for measurement. Picture taken from VDI product manual [5].

A typical setup with VNA and VDI extenders for measurement is shown in Figure 2.5 (Figure 10 in [5]). These models are chosen because they provide the best dynamic range in the global market, and since the loss during the transmission from one extender to the other is expected to be fairly high, especially when multiple cavities are connected, we must ensure that the dynamic range is large enough for the transmitted signal to stay above the noise level.

2.3.2 Cryostat

A cryostat is an apparatus for maintaining a very low temperature. In our setup, we are using a custom made BlueFors BF-XLD400 cryogen-free dilution refrigerator system that can reach a base temperature of 10 mK under minimum heat-load

conditions. The space available for mounting samples is a cylinder of 50 cm in diameter and 50 cm in height, giving us a volume of $V \approx (450\lambda)^3$ at 300 GHz. For $s = 40$, we are scaling the frequency from 5.5 ~ 8.25 GHz to 220 ~ 330 GHz, and shrinking a geometry as large as $V \approx 25^3\text{m}^3$ into our cryostat. This is extremely difficult to achieve in full scale and also hard to operate and manage. Our scaled setup is an elegant solution to electromagnetic problems in such large scales.

Figure 2.6 shows the drawings, the outside vacuum can and the cooling plates inside of the cryostat. The horizontal circular plates will be cooled down to 50K, 4K, 1K and 10mK from the top plate to the bottom plate, respectively. Our sample cavity will be mounted onto the bottom plate (the sample plate) which should reach the lowest temperature. There are several thermal shields designed to thermally isolate the cooling plate and a vacuum can at the outermost layer to provide a single vacuum space. Due to the need for a special free-space propagation path from extender to the sample cavity, there are windows on the side of the cryostat shields allowing electromagnetic waves to propagate in and out of the cryostat interior. These windows, allowing outside radiation to get inside, puts an extra heat load on the cryostat, which changes the lowest temperature that it can reach from 10 mK to about 10 K. However, this higher base temperature is still lower than we need for the scaled structure measurement.

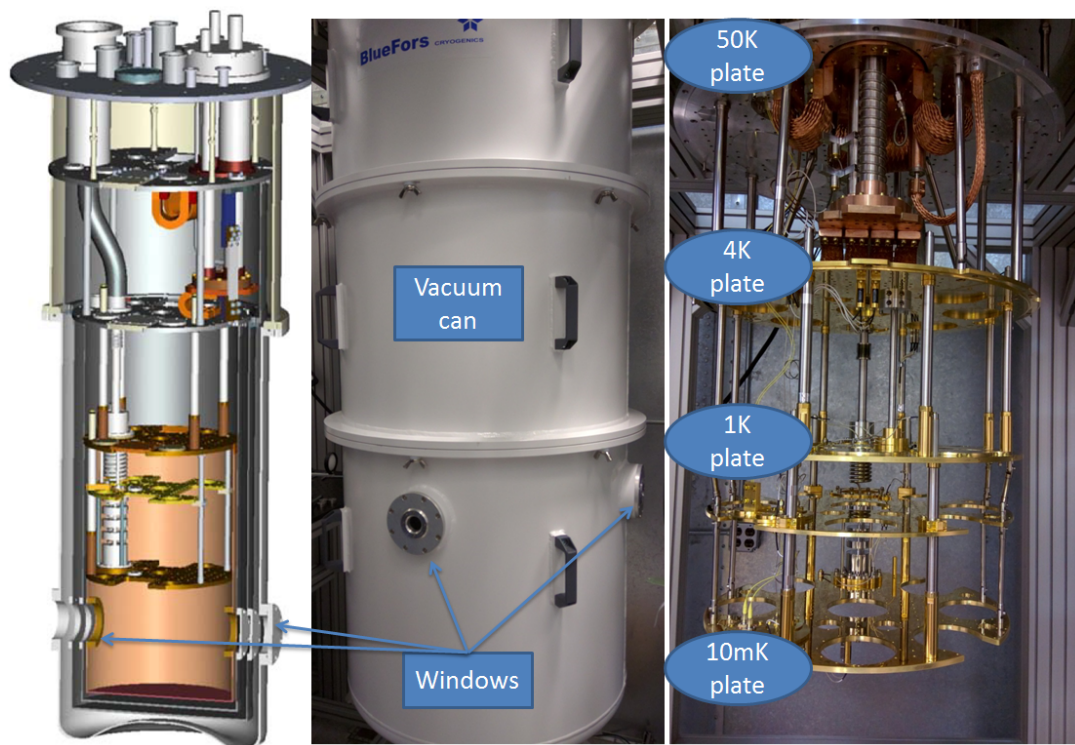


Figure 2.6: The drawings (left), the outside vacuum can (middle) and the cooling plates inside of the cryostat (right). The cooling plates are cooled in a staged manner from 50K at the top to 10mK at the bottom. The sample will be mounted onto the 10 mK plate, also called the sample plate.

2.3.3 Free-space Propagation Path

Since the miniature cavity is sitting inside the evacuated cryostat at low temperature, it is not possible to employ an input connection from the signal source to the cavity via a coaxial cable or waveguide. Accordingly, we use a quasi-optical free-space propagation path similar to that of a collimated beam in an optical experiment.

The high frequency electromagnetic wave coming out of the frequency extender is launched into air by a horn antenna, then collimated by a Teflon lens. The output is a collimated beam propagating in free-space like a plane wave which has significantly lower loss compared to transmission in any waveguide or transmission line. The receiving end has a focusing lens, identical to the one on the source side, and a receiving horn antenna which is mounted on the wall of the cavity to transmit the received wave into the cavity. Two such free-space propagation paths are used for the two cavity ports, one path for each port. Figure 2.7 shows the experimental setup highlighting the free-space propagation path, the frequency extenders, the horn antennas, and the lenses.

This free-space propagation path has its advantages and challenges compared to other methods.

First of all, there is no direct thermal contact between the source and the cavity. This is the most crucial reason why we choose this setup. The cavity needs to be cooled to a low temperature inside the cryostat in order to achieve conductivity scaling. A direct connection, such as waveguide, will certainly prevent the cavity

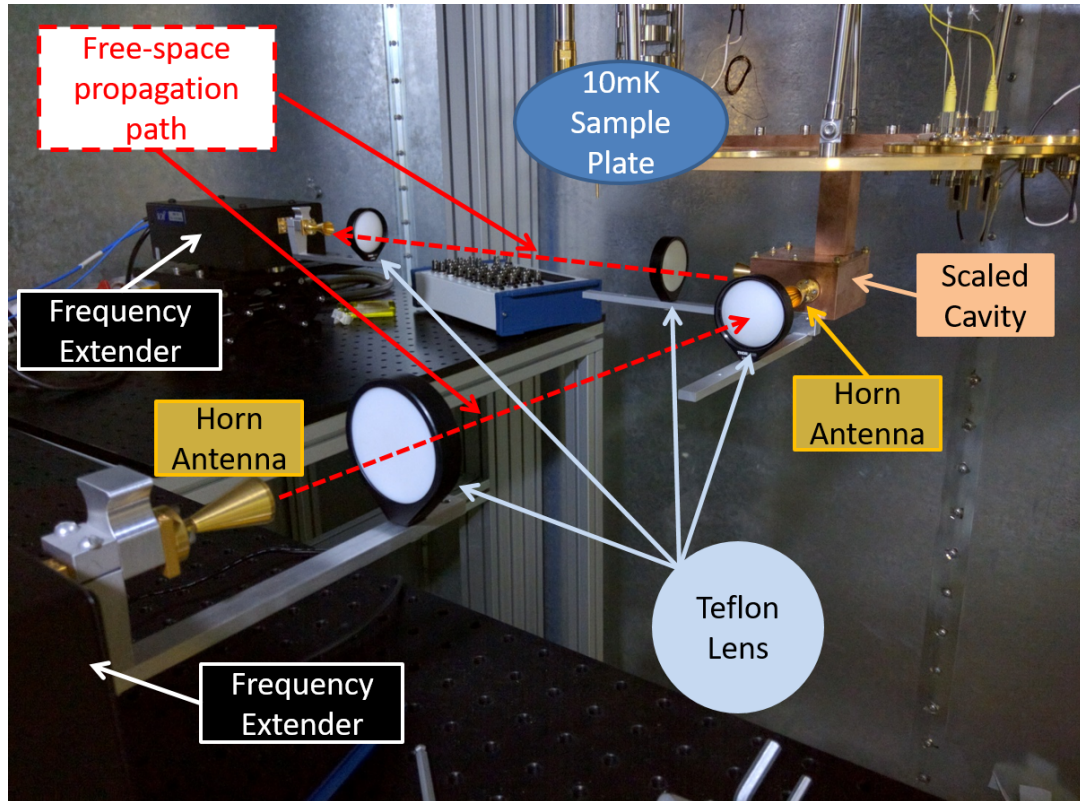


Figure 2.7: The setup for high frequency waves to propagate in free-space from the frequency extender to the cavity, and from the cavity to the receiving frequency extender. The horn antennas can efficiently launch and receive electromagnetic waves and the Teflon lens collimates the waves into a parallel beam.

from cooling down by thermal conduction. Whereas this remote injection method only introduces some thermal radiation which can be lowered by proper filtering.

Secondly, it is very low loss. Transmission lines and waveguides suffer from high loss at high frequency due to the scaling of ohmic loss and dielectric loss with frequency. The ohmic loss in metal is proportional to the surface resistance $R_s = 1/(\sigma\delta)$ where σ is the conductivity and $\delta = \sqrt{2/(\omega\mu\sigma)} \propto 1/\sqrt{\omega}$ is the skin depth. So $R_s \propto \sqrt{\omega}$ increases as frequency goes up, leading to higher ohmic loss. In addition to ohmic loss, transmission lines also have dielectric loss which also scales with frequency. In transmission lines, waves propagate as $\mathbf{E}(z) = \mathbf{E}_0 e^{-(\alpha+i\beta)z}$, where α is the attenuation constant (not the loss parameter in RCM) given by $\alpha \approx (\omega\epsilon''/2)\sqrt{\mu/\epsilon'}$ in which $\epsilon = \epsilon' - j\epsilon''$ is the complex permittivity of the dielectric. So $\alpha \propto \omega$ and the wave decays much faster when frequency goes up.

However, it is a challenge to properly collimate the free-space beam. For free-space propagation, the dielectric loss in air is negligible, and the reflection at the horn antenna due to the impedance mismatch is also very small, about -20 dB (1% of power is reflected). The only significant factor for losing signal strength is the imperfect collimation. Since the frequency is not in the visible light spectrum range, it is not easy to properly position the antenna and lens to guarantee best collimation. But through careful experimentation, we can achieve an average transmission amplitude of -5 dB across a 1 meter transmission distance for WR3.4 band (220 ~ 330 GHz). For comparison, the loss of a 1 meter long gold-plated waveguide (about \$1000 per 5 cm piece) would be 14 ~ 20 dB, according to the Virginia Diode Inc waveguides data sheet [60].

2.3.4 Mode Stirrer

Since the RCM is a statistical theory, an ensemble of scattering systems is required to determine the system-specific features and the statistical properties of the enclosures. Consequently, we need to perturb the cavity modes while maintaining the volume of the cavity such that each measurement is a unique realization of the cavity with the same loss parameter. A typical method to create many realizations is to rotate a large metal panel inside the cavity (a “mode stirrer”), as used in Refs. [6, 23, 61, 62]. But for our setup, which has very high frequency and is sitting inside the cryostat in low temperature, we need to consider the following issues:

- The motor that powers the panel must be able to work in high vacuum and low temperatures. The heat generated by the motor coil can quickly build up in vacuum with normal motors, and the motor material and design must be carefully chosen such that thermal contraction won’t cause mechanical problems.
- The cavity must be tightly enclosed by metal walls since any small gap or hole can leak out the electromagnetic waves reverberating inside. Normally The hole on the wall to host the panel axis is not a problem since the microwave wavelength (a few centimeter) is much larger than the hole diameter (a few millimeter). But with the wavelength scaled into the millimeter range, the leakage through the hole is substantial.

To meet these requirements, we designed a magnetically coupled mode stirrer

powered by a cryogenic stepper motor, as shown in Figure 2.8. The cryogenic stepper motor (Phytron VSS 52.200.2.5UHVC) is suitable for ultra high vacuum (up to 10^{-11} mbar) and cryogenic temperature environment, typically used in space applications. The motor rotates a magnetic strip outside the cavity which is magnetically coupled to another magnetic strip inside the cavity, thus eliminating the need for an opening on the wall or direct mechanical contact. The metal mode-stirring panel is attached to the inside magnetic strip and rotates when the stepper motor rotates.

It is worth noting that we do not need to control the exact location or the shape of the perturber for any given measurement, which would be an extremely difficult task in such a high frequency (and short wavelength) regime. The goal is to create an ensemble of scattering systems which differ in detail, but all have the same underlying statistical properties. Since the sole purpose of introducing the perturber is to scatter the waves in a different way without changing the statistical properties of the cavity (i.e. the loss parameter α) the precise location and orientation of the perturber is not important. However, it is important that we rotate and move the perturber to uniquely different orientations and positions, so that a diverse set of cavities with different scattering properties is created, enabling a high quality statistical ensemble.

In experiments, the motor rotates a small step then waits for the Vector Network Analyser (VNA) to measure the S-parameters of the cavity in the current realization. When the VNA measurement is complete, the motor rotates again, and this process is repeated. Representative S-parameter measurements for two nearby realizations of the cavity and perturber are shown in Fig. 2.8 (b). In this way, data

for 200 highly uncorrelated realizations of the full-scale cavity is collected and used to obtain statistics of the electromagnetic properties, and to calculate the ensemble average required by the RCM to characterize system-specific properties. After collecting the ensemble S-parameter data, we check to see if each realization is statistically independent to a significant degree from all the others by looking at their correlation coefficient. The Matlab function “corrcoef” is used for this purpose. We then construct the impedance matrix for the cavity data Z_{cav} as described in Section 1.4. The ensemble averaged impedance is obtained as $Z_{\text{avg}} = \langle Z_{\text{cav}} \rangle_{\text{realizations}}$ for each measured frequency point. A histogram of the impedance values is constructed by taking the real or imaginary part of a matrix element of the Z-matrix over the entire ensemble (9 realizations for the miniature cavity or 200 realizations for the full-scale cavity) and over the whole frequency range (75 - 110 GHz for the miniature cavity or 3.7 - 5.5 GHz for the full-scale cavity). For the miniature cavity, since the cavity is gradually changing temperature, also changing the cavity loss, we can only measure 9 realizations in a half hour window before the loss between the first and last measurement differ significantly. It turns out that the large number of data points for many modes within the broad frequency bandwidth compensates the lack of realizations and we still get good statistics.

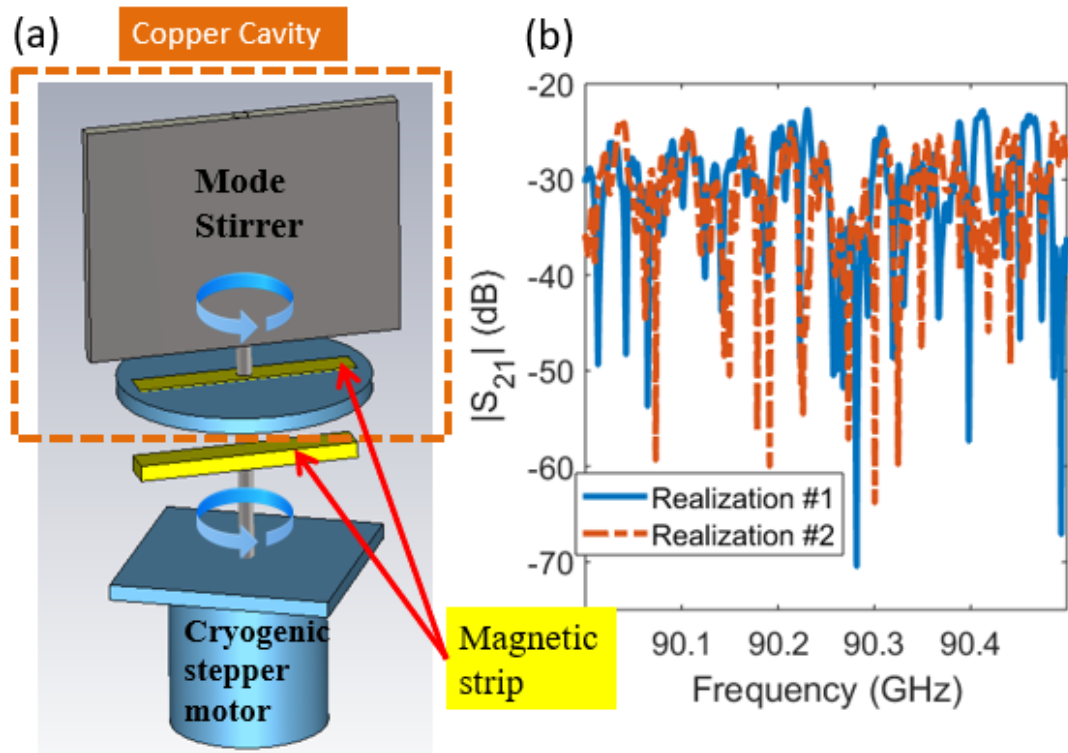


Figure 2.8: Magnetically coupled mode stirrer powered by a cryogenic stepper motor. The magnetic strip outside the cavity (lower yellow bar in the left side) is coupled by static magnetic field with the magnetic strip inside the cavity (upper yellow bar in the left side), eliminating the need for any hole on the wall. The upper right inset is an example of the mode stirrer placed inside the cavity.

2.4 Testing Experiments

In a larger picture, our final goal is to test the RCM prediction of the statistics of the energy coupled into the N^{th} cavity in a cascade of connected cavities using the setup introduced in Section 2.3. This work is in collaboration with U.S. Naval Research Laboratory (NRL). As a first step, our colleagues at NRL measured a full-scale 66 cm X 122.5 cm X 127.5 cm aluminum cavity at 3.7 ~ 5.5 GHz (WR187 band) and 5.5 ~ 8.25 GHz (WR137 band). We measured 2 scaled cavities with $s = 20$, scaling from 3.7 ~ 5.5 GHz to 75 ~ 110 GHz, and $s = 40$, scaling from 5.5 ~ 8.25 GHz to 220 ~ 330 GHz, respectively. After confirming that the scaled-down setup produces the same statistical impedance for the same α as the full-scale setup, we can proceed to investigate the statistical property of the connected cavities.

In this section, we perform a series of experiments that can verify the operation of our experimental setup. Since the combination of the frequency extenders, remote injection and cryogenic environment was never explored before, we take progressive steps to study each component individually. Then later in section 4 we present the single cavity experiment result to confirm that the setup produce the same statistics, and in section 5 we discuss the multiple cavity experiment result.

2.4.1 Overall Plan

Since this experimental setup is rather complex and has not been studied by any research group known to us, we take the following incremental steps towards the final goal making sure that we understand the results at each stage.

1. Obtain good transmission at mm-wave frequencies for the free-space propagation path between two horn antennas.
2. Directly measure the scaled cavity, without the free-space propagation path, perturb the cavity modes using the magnetically coupled mode stirrer and repeat the measurements. Confirm that the collected realizations represent a good ensemble of the cavity. In all following experiments, a “measurement” means collecting an ensemble of data rather than measure the cavity at one single state.
3. Directly measure the scaled cavity, without the free-space propagation path, and calculate its loss parameter α at room temperature. This is called a “direct injection” measurement.
4. Measure the scaled single cavity at room temperature with the free-space propagation path installed and compare the calculated α with direct injection. This is called a “remote injection” measurement.
5. Put the remote injection setup in the cryostat to perform the same measurement at low temperatures. Note that this involves propagating the mm-wave signals through windows on each free-space path. We expect to see a decrease of α with decreasing temperature. We compare the obtained α values to the result of the full-scale setup measurement done by our collaborators at NRL making sure that the scaled setup works well for a single cavity. This is discussed in section [4](#).

6. Extend the scaled single cavity setup to multiple connected cavities. Investigate the statistics of the power coupled into the N^{th} cavity and test the RCM predictions in [3, 24]. This is discussed in section 5

The rest of the section 2.4 discuss items 1 to 4 on this list.

2.4.2 Free-space Propagation Path Measurement

The purpose of this measurement is to determine the best distance between the antenna and the Teflon lens in order to get the optimal transmission through free-space. The two antennas are placed at a fixed distance, about 110 cm apart, and the lenses are placed at a distance of d_1 from the transmitter horn antenna and d_2 from the receiver horn antenna. All elements are aligned to be on a single line and only d_1, d_2 are varied. The average transmission is plotted in Figure 2.9 with the best values of d_1, d_2 enclosed in the yellow dotted circle. For the WR10 band, $d_1 = d_2 = 10.45$ cm and for the WR3.4 band, $d_1 = d_2 = 15.45$ cm.

2.4.3 Collecting an Ensemble of Cavity Data

This experiment tests if the magnetically coupled mode stirrer can effectively perturb the cavity modes in the cryogenic environment. An example of the measured reflection (S_{11}) and transmission (S_{21}) magnitude data for the $s = 20$ cavity is plotted in Figure 2.10 for 5 realizations. Notice that the full frequency range plot for $|S_{11}|$ on the top left shows that all curves follow the slowly varying trend which is the non-statistical system specific feature, while the zoom-in plot on the top right

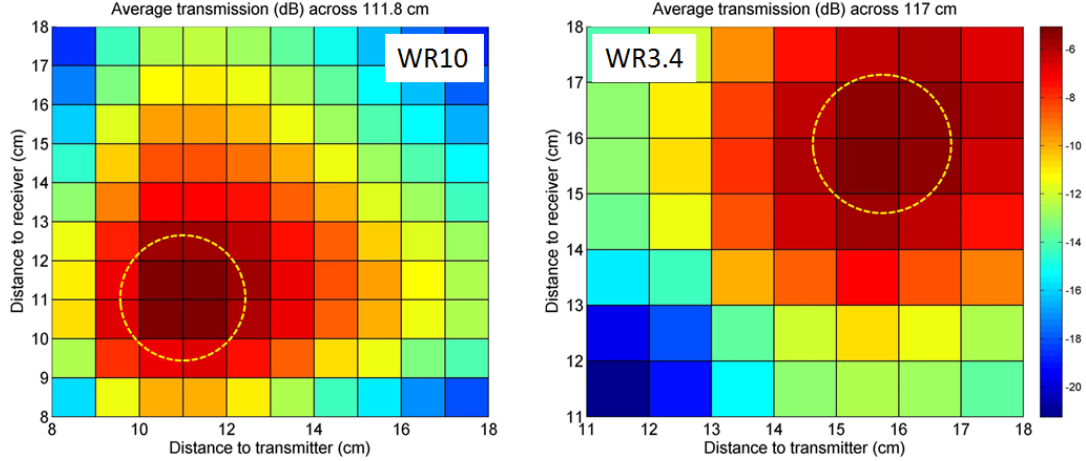


Figure 2.9: The transmission amplitude in dB for free-space propagation measurement. The x-axis and y-axis are the distance between the lens to the transmitter antenna (d_1) and the receiver antenna (d_2) respectively. The yellow dotted circles enclose the region for best d_1, d_2 values for optimal transmission.

shows that each curve differs dramatically from each other, which is the result of the mode stirrer perturbing the cavity modes.

It is clear from Figure 2.10 that the cavity modes are indeed perturbed but we need to further ensure that realizations are uncorrelated with each other and represent a statistically sound ensemble. To do this, we adopt the use of the power ratio Λ defined in Ref. [2] as the ratio of the maximum transmitted power to the minimum transmitted power at each frequency for all mode stirrer positions, i.e. $\Lambda = \max(|S_{21}|^2)/\min(|S_{21}|^2)$. Λ is a function of frequency and should have a large mean and a large dynamic range if the cavity modes are well perturbed and uncorrelated, which gives us a good ensemble of data. To see how Λ distinguishes a good ensemble from a bad one, we plot two Λ spectra calculated from 2 ensembles, each consisting of 9 realizations, and their histograms in Figure 2.11. The Λ in the left figure, which represent a good ensemble, has a mean of about 15 dB and a dynamic range of 40 dB,

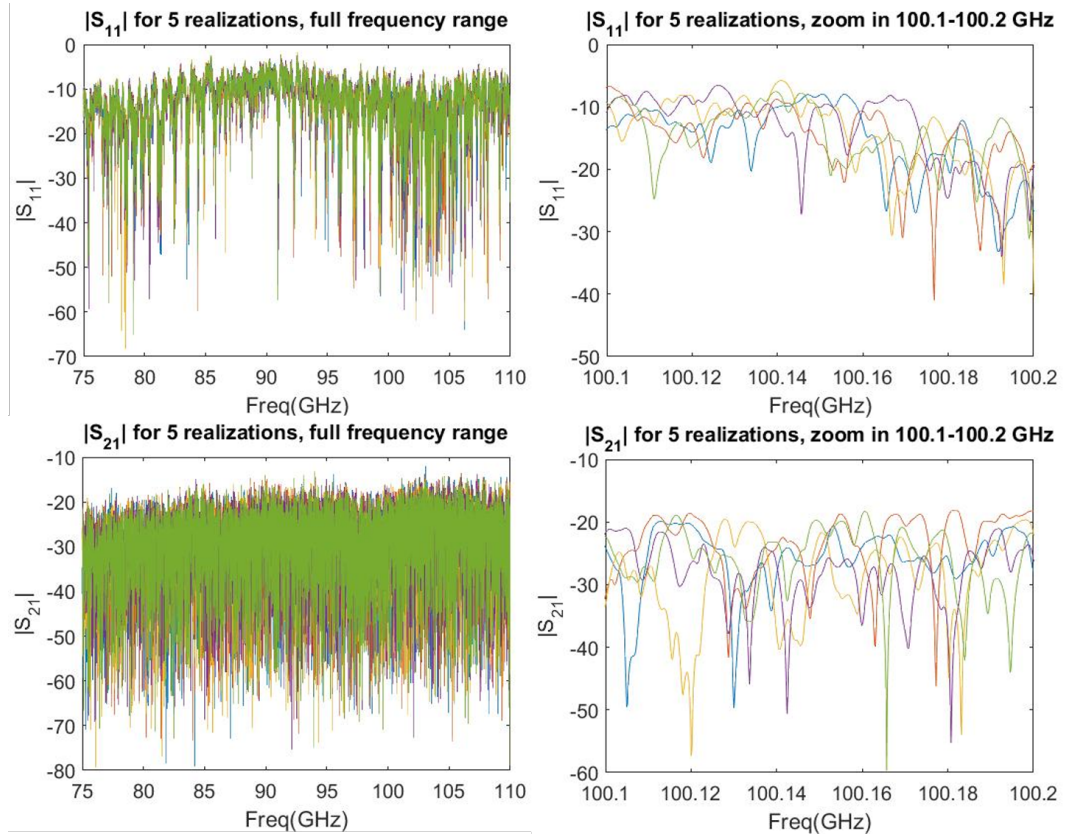


Figure 2.10: Experimentally measured reflection (top two plots) and transmission (bottom two plots) magnitude for the $s = 20$ cavity for 5 realizations created by rotating the magnetically coupled mode stirrer. The left column plots the data in the full frequency range from 75 GHz to 110 GHz while the right column zooms in a 100 MHz window. Each curve is wildly different from others but yet follow the same slowly varying trend which is the non-statistical system specific feature.

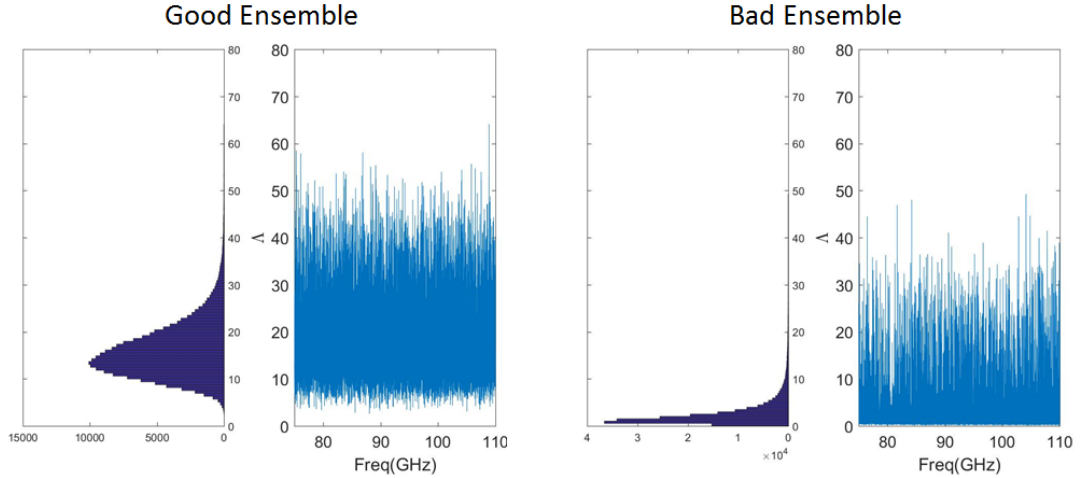


Figure 2.11: Power ratio Λ as a function of frequency and its histogram for a good ensemble (left) and a bad ensemble (right) data. Λ should have a large mean and a large dynamic range if the cavity modes are well perturbed and uncorrelated, which gives us a good ensemble of data.

indicating large field fluctuations as the mode stirrer rotates. On the contrary, the Λ on the right figure has an almost zero mean and 15 dB dynamic range, suggesting high correlation between realizations. In fact, the data in the right figure were taken when the mode stirrer was stuck and not moving.

2.4.4 Direct Injection

The purpose of the direct injection experiment is to get an accurate value for the cavity loss parameter α before applying conductivity scaling and without the influence of the free-space propagation path.

As shown in Equation (2.2) if we only scale the cavity size and measurement frequency, then the loss parameter $\alpha \propto \sqrt{s/\sigma}$. Based on the previous RCM experiment on the full-scale cavity [6], $\alpha(s = 1) \approx 2.05$ for 3.7 ~ 5.5 GHz and $\alpha(s = 1) \approx 5.95$ for 5.5 ~ 8.25 GHz as shown in Figure 2.12. Thus we are expecting

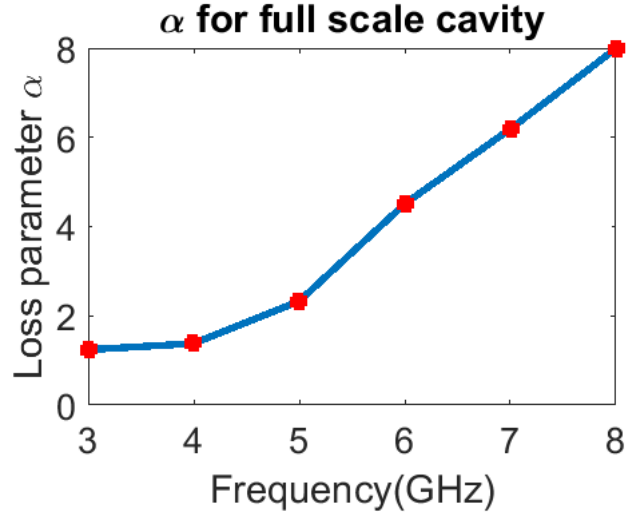


Figure 2.12: Loss parameter α values for the full scale cavity measured by collaborators at U.S. Naval Research Laboratory. Each α value is calculated from experimental data in a 0.1 GHz window at the specified frequency. The data points are taken from Table 1 in [6].

$\alpha(s = 20) \approx \sqrt{20}\alpha(s = 1) = 9.17$ for the WR10 band and $\alpha(s = 40) \approx \sqrt{40}\alpha(s = 1) = 37.6$ for the WR3.4 band. As mentioned in Section 2.2.2, the scaled cavity material is copper (and the full-scale cavity material is aluminum) so there is a scaling up of conductivity $\sqrt{\sigma_{\text{Cu}}/\sigma_{\text{Al}}} = \sqrt{5.96/3.50} = 1.30$. Thus the α we should see for the $s = 20$ (WR10 band) cavity is $9.17/1.30 = 7.05$, and for the $s = 40$ (WR3.4 band) cavity is $37.6/1.30 = 28.9$. Notice that these are just estimates, based on the metal bulk conductivities for pure metal. In experiments, the actual ohmic loss depends on the surface resistance and the penetration depth, which is influenced by the impurity, surface roughness [58, 59], temperature and is frequency-dependent.

The PDF of the normalized impedance for a direct injection experiment on a scaled-down $s = 20$ copper cavity is shown in figure 2.13. By fitting with the RCM predictions for the PDF for various α , which is obtained through a series of Monte Carlo simulations with different α values, we determined that $\alpha = 4.5$ for the direct

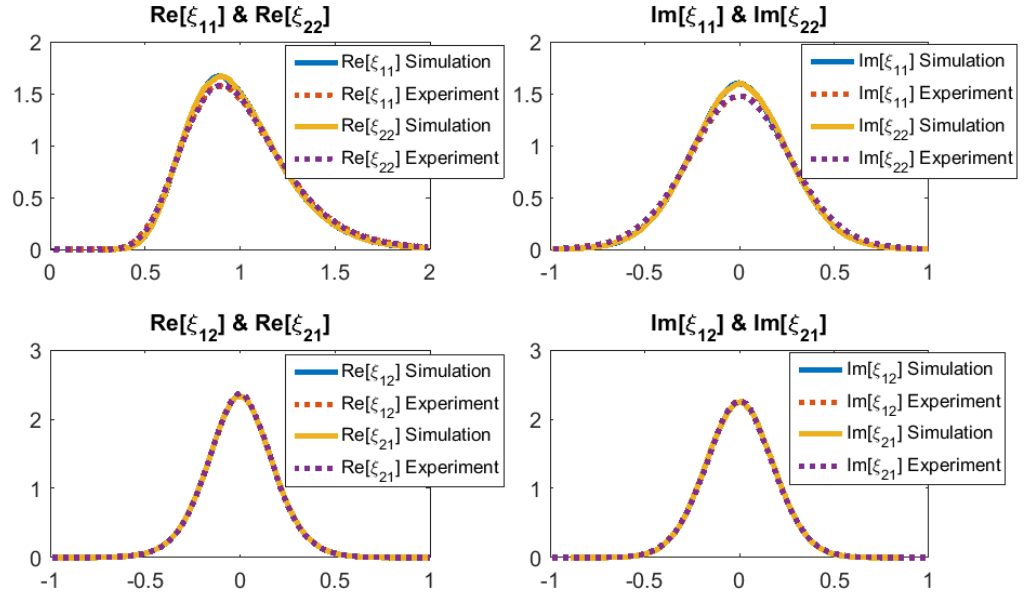


Figure 2.13: Probability Density Function (PDF) of the normalized impedance for a direct injection experiment on a scaled-down $s = 20$ copper cavity (dotted line), in comparison with the RCM Monte Carlo simulation with $\alpha = 4.5$ (solid line).

injection setup. This value is close to what we expect, which is about 7.

It was later discovered from the time-domain method, discussed in section 3.2.2, that this $\alpha = 4.5$ is actually an overall α that includes both the cavity's loss and the loss in the short waveguide section in the cavity wall. The copper cavity has a quarter inch thick wall and the mm-wave enters and exits the cavity through two rectangular openings on the wall, which are essentially two quarter inch long waveguides. The waveguides in the wall add up the total loss and need to be excluded from the total loss, characterized by $\alpha = 4.5$ in the direct injection experiment, to reveal the true cavity loss. This is done by introducing the radiation efficiency η into the RCM, which is discussed in chapter 3.

2.4.5 Remote Injection

The remote injection measurement is similar to the direct injection except that the two free-space propagation paths, one at the transmitter end and one at the receiver end, must be installed, as shown in Figure 2.7. The α value calculated from Equation 1.4 is around 30, much higher than the direct injection α value because of the influence from the lossy free-space propagation path. The RCM normalization procedure in Section 1.5 can only normalize out the system-specific features that are lossless. Without any modification to Equation 1.4, the obtained α represent the overall lossyness, including the cavity and the lossy free-space path. If we consider the lossy free-space path together with the horn antennas as a complex “port” or a composite “antenna”, then this can be generalized into the problem of RCM with lossy ports. The solution is to use the radiation efficiency to quantify the lossyness of the ports and then properly exclude it from the overall α . This is discussed in detail in Chapter 3.

2.4.6 Extension to Multiple Connected Cavities

The experimental setup and the results for multiple scaled cavities are discussed mainly in Chapter 5. As a brief preview, the life-size 3D-printed model of the system and the configuration for a 3-cavity cascade is shown in Figure 2.14. This design is for $s = 20$ and has the advantage of being reconfigurable, extendable and is compatible the remote injection setup in the cryostat.

The backplane is a thin metallic plate, which is vertically attached to the cold

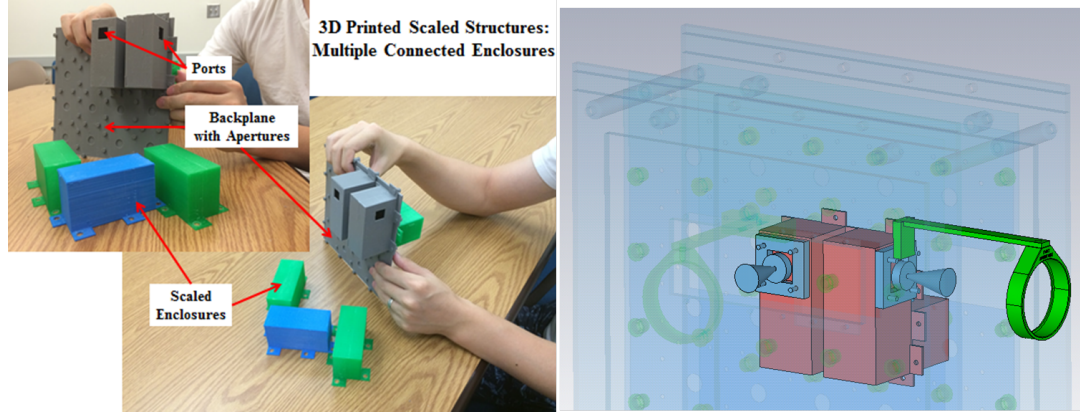


Figure 2.14: 3D-printed model of the multiple connected cavities and the configuration for a 3-cavity cascade drawn in CST.

plate in the cryostat, and has screw holes for mounting the rectangular cavities. It also has apertures to couple the cavities mounted on one side to the ones mounted on the other side. If we view the backplane as a grid, where each grid cell has a circular aperture at its center, then the cavity is a 2-cell block having 5 walls. And once mounted to the backplane, it will have 2 open apertures. There are two special cavities that have a rectangular opening on the side, as highlighted in Figure 2.14 as "ports". The rectangular opening is covered by a special adapter that has the Teflon lens attached to it, positioned at a certain distance to the antenna and is well aligned. The three blocks attached to the backplane in Figure 2.14 is an example of a simple 3-cavity cascade. In the left figure, the 2 gray cavities at the front are the first and third cavity which will have the horn antennas installed on the rectangular apertures. They both couple to the green cavity on the other side through large circular apertures on the backplane. The 3-cavity cascade model is also shown in Figure 2.15 with cavity walls and backplane omitted.

With this grid-cell model we can easily compose any N -cavity cascade and

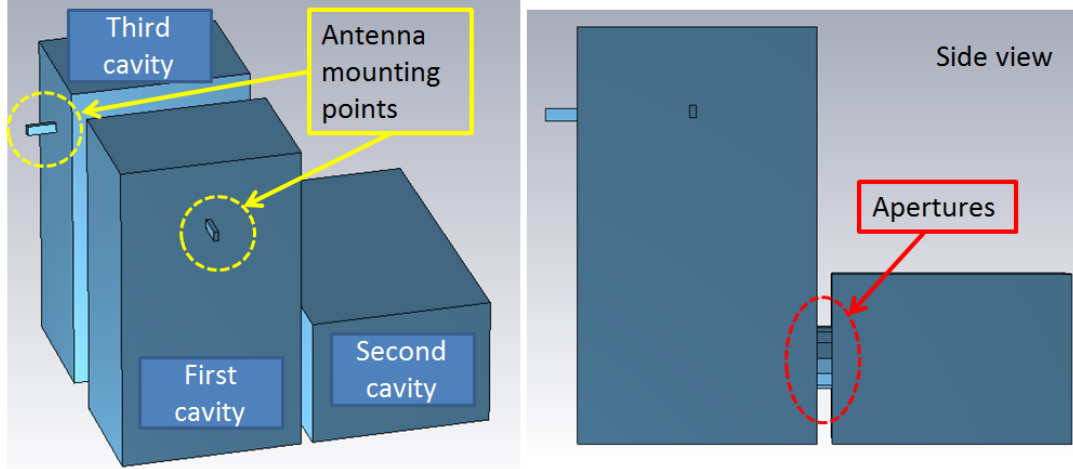


Figure 2.15: The air region of the 3-cavity cascade model with cavity walls and backplane omitted. The wave goes into the first cavity through the antenna mounting point, then couples into the second cavity mounted on the other side of the backplane (not shown) through an aperture. It is then coupled to the third cavity through the other aperture, and gets out through the antenna mounting point on the third cavity.

place it in the remote injection setup to measure its characteristics. For this $s = 20$ scaled cavity size, we can easily put 20 cavities on each side of the backplane, more than enough for the connected cavity analysis. Furthermore, we can put additional backplanes parallel to the existing one to host additional cavities. This design allows us to investigate many interesting coupled cavity configurations beyond the theory prediction.

2.4.7 Further Studies

The remote injection scaled measurement setup described in Section 2.3 combined with the grid-cell cavity design mentioned above opens up the opportunity to study RCM predictions in a network of connected cavities.

In the grid-cell cavity design, cavities are basically 2-cell blocks and thus are

2-port cavities with the apertures acting as the port connecting to other cavities. We can extend the cavities to be 3-cell or 4-cell blocks that covers 1X3 cells or 2X2 cells making them 3-port or 4-port cavities. Their volume can be maintained by changing the height of the cavities. If we consider the cavities as nodes, we can arrange them on the backplane such that they form a network, such as a tetrahedron (3-branch nodes) or a pentagon (4-branch nodes). The linear cascade that we are going to study initially is the case of the simplest network, as illustrated in Figure 2.16. By changing the cavities from 1X2 blocks to 2X2 blocks, we can use the similar setup to study complicated graphs as shown in Figure 2.17. The example network has a total of seven connected scaled cavities that are of different sizes and have anywhere from one to four apertures. Each cavity is represented as a node and each aperture is represented as an edge in the graph. Limited only by the size of the cryostat interior, the number of different networks that we could study with this experimental setup is orders of magnitude larger than that with a conventional full scale cavity setup.

Furthermore, the volume inside the cryostat is so large compared to the scaled-down cavities that we can potentially shrink even larger structures. For example, the cryostat's cylindrical space of diameter $d = 50$ cm and height $h = 50$ cm is equivalent to a full scale cylinder of $d = 10$ meter and $h = 10$ meter at $s = 20$, and $d = 20$ meter and $h = 20$ meter at $s = 40$ which is almost the size of a townhouse or a boat. Studying such large structures directly may be expensive and difficult to manage but it is much easier when the structure is miniaturized.

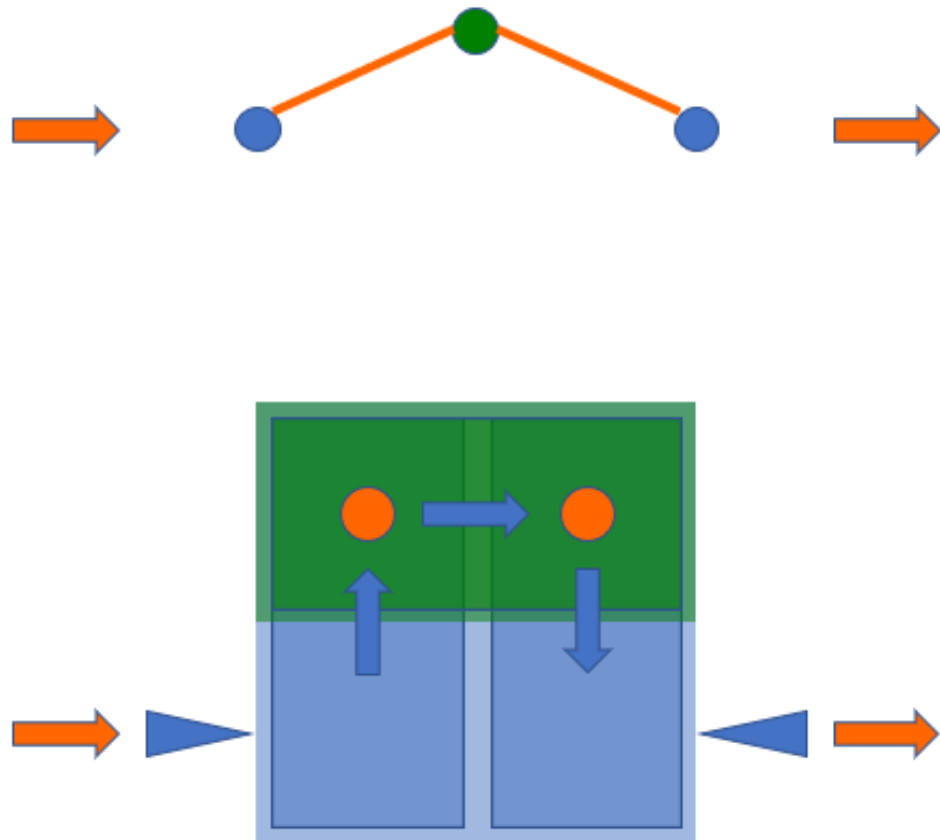


Figure 2.16: A simple cascade of three scaled cavities. Top: the graph of the cascade, consisting of three nodes (scaled cavities) and two edges (apertures connecting two neighbor cavities). Bottom: the configuration of scaled cavities mounted onto the two opposing sides of a central plate. Green rectangles represent scaled cavities on the front side and blue rectangles represent scaled cavities on the back side. Orange circles represent apertures connecting the two cavities on the opposing sides.

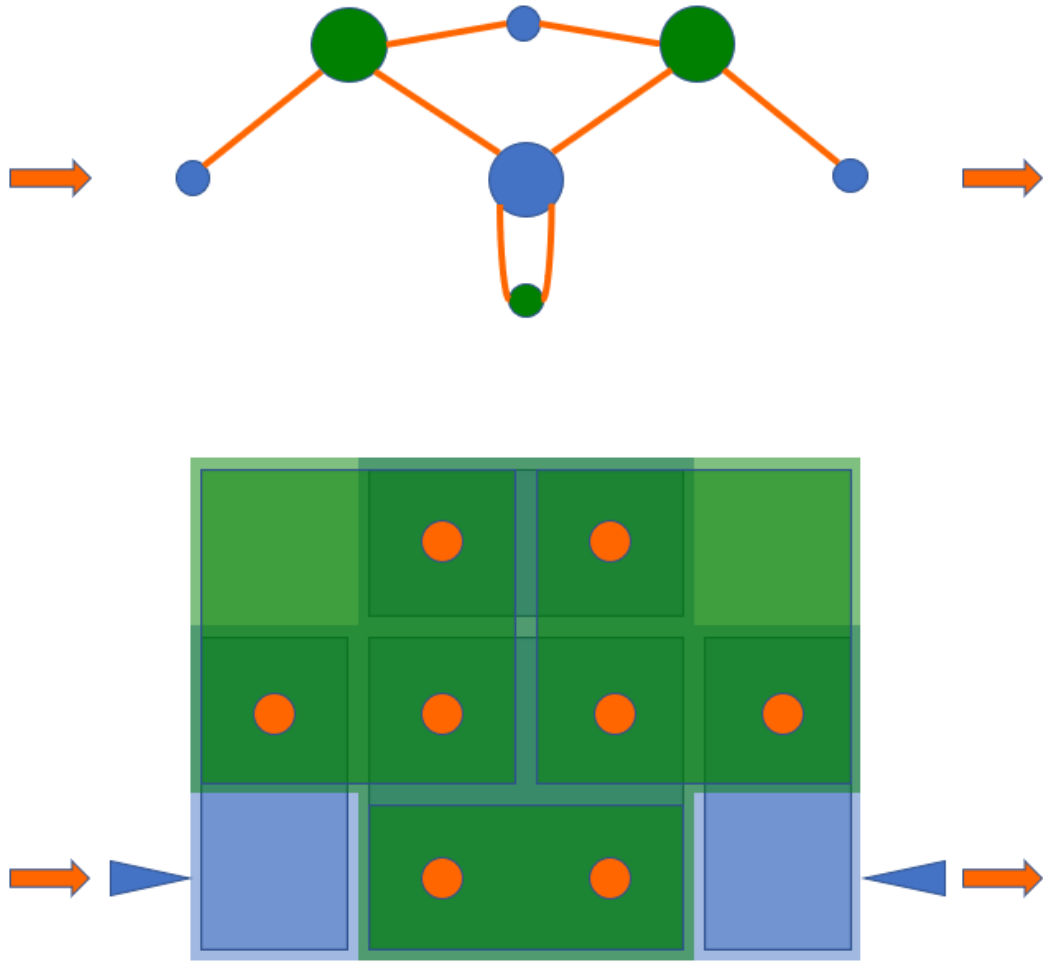


Figure 2.17: A network of seven scaled cavities. Top: the graph of the network, consisting of seven nodes (scaled cavities) and eight edges (apertures connecting two neighbor cavities). Bottom: the configuration of scaled cavities mounted onto the two opposing sides of a central plate. Green rectangles represent scaled cavities on the front side and blue rectangles represent scaled cavities on the back side. Orange circles represent apertures connecting the two cavities on the opposing sides.

Chapter 3: Introducing Radiation Efficiency to the Random Coupling Model

The RCM normalization procedure discussed in Section 1.5 can only normalize out the system-specific features that are lossless. Without any modification to Equation 1.4, the α calculated from fitting the impedance statistical distribution functions represents the overall lossyness, including the cavity and the lossy free-space path. If we consider the lossy free-space path together with the horn antennas as a complex “port” or a composite “antenna”, then this can be generalized into the problem of RCM with lossy ports. The solution is to use the radiation efficiency to quantify the lossyness of the ports and then properly exclude it from the overall α . This was first proposed and explored by Bisrat Addissie in [7] for one-port systems. In this section we summarize the findings, extend to multiple-port systems, verify the modified RCM equation and apply it to the experimental data.

3.1 Radiation Efficiency η and RCM With Lossy Ports

Radiation efficiency η is the ratio of the power radiated by the antenna to the input power delivered to the antenna, with a value between 0 and 1. It describes the lossyness of the antenna with 0 meaning completely lossy (nothing get radiated) and 1 meaning a lossless antenna such that all power delivered to the antenna is radiated. The original RCM assumed loss-less antenna. In the case of a lossy antenna, the RCM needs to take into account the loss contributed by the antenna and separate it from the cavity’s loss in order to get a good estimate of the loss

parameter α for the cavity. The cavity impedance equation is modified from

$$\mathbf{Z}_{\text{cav}} = j\text{Im}[\mathbf{Z}_{\text{avg}}] + \text{Re}[\mathbf{Z}_{\text{avg}}]^{1/2}\boldsymbol{\xi}\text{Re}[\mathbf{Z}_{\text{avg}}]^{1/2}, \quad (3.1)$$

where \mathbf{Z}_{cav} is the measured cavity's impedance, $\mathbf{Z}_{\text{avg}} = \langle \mathbf{Z}_{\text{cav}} \rangle_{\text{realizations}}$ is the ensemble average of the \mathbf{Z}_{cav} , and $\boldsymbol{\xi}$ is the normalized impedance which has the universal statistical properties predicted by the RMT (depending only on the loss parameter α), to this equation

$$\begin{aligned} \mathbf{Z}_{\text{cav}} &= \mathbf{Z}_{\text{avg}} + \mathbf{R}^{1/2}(\boldsymbol{\xi} - \mathbf{I})\mathbf{R}^{1/2} \\ \mathbf{R} &= \boldsymbol{\eta}^{1/2}\text{Re}[\mathbf{Z}_{\text{avg}}]\boldsymbol{\eta}^{1/2}, \end{aligned} \quad (3.2)$$

where $\boldsymbol{\eta}$ is a diagonal matrix with η_{ii} being the radiation efficiency for the i^{th} port. This formula is only valid for high loss systems where the loss parameter $\alpha > 5$. This is because a few assumptions during the derivation in section 3.1.2 will gradually break down as α gets smaller.

This modified RCM expression for \mathbf{Z}_{cav} was first introduced by Bisrat Addissie in [7] for one-port systems, and we extend it here to multi-port systems. The following section discusses how η is incorporated into the RCM original expression for cavity impedance.

3.1.1 \mathbf{Z}_{rad} , \mathbf{Z}_{ant} , \mathbf{Z}_{cav} and \mathbf{Z}_{avg}

It is necessary to first clarify the differences between these frequently seen quantities in RCM equations and some implicit assumptions associated with their definitions.

- \mathbf{Z}_{rad} is the radiation impedance of the ports, which describes the system-

specific features that need to be normalized out from the measured data. It can be obtained by placing the antenna in an anechoic chamber, a cavity with absorbers on the walls to suppress reflection, and measuring its reflection in a free radiating environment. In many RCM papers [23, 63] \mathbf{Z}_{rad} is used instead of \mathbf{Z}_{avg} in Equation (3.1) but the problem is that \mathbf{Z}_{rad} is not readily available or easily measurable in experiments, especially for lossy antennas. It also ignores the short orbit effect which is extensively discussed in [38].

- \mathbf{Z}_{ant} is the input impedance of the antennas, or the ports, which is equivalent to \mathbf{Z}_{rad} if the ports are lossless. However, if the ports are lossy then the relationship between \mathbf{Z}_{ant} and \mathbf{Z}_{rad} is not trivial and we will derive it in the following section making the connection to the radiation efficiency η .
- \mathbf{Z}_{cav} is the measured cavity impedance which includes the slowly varying \mathbf{Z}_{ant} in terms of frequency and the fast frequency-dependent fluctuations due to the cavity modes. In experiments we randomly perturb the cavity modes while keeping \mathbf{Z}_{ant} unchanged, and then measure \mathbf{Z}_{cav} after each perturbation. This process is repeated to collect an ensemble of data. \mathbf{Z}_{cav} is the measurement data and is the starting point for post-experiment RCM analysis.
- \mathbf{Z}_{avg} is the ensemble average of the measured \mathbf{Z}_{cav} . The fluctuating component of \mathbf{Z}_{cav} due to the cavity modes is cancelled out in the averaging since it is randomly perturbed, leaving only the \mathbf{Z}_{ant} and the influence of short orbits [38] which are robust against perturbations and thus are not part of the statistical property. So for practical purposes, we usually use \mathbf{Z}_{avg} in RCM equations

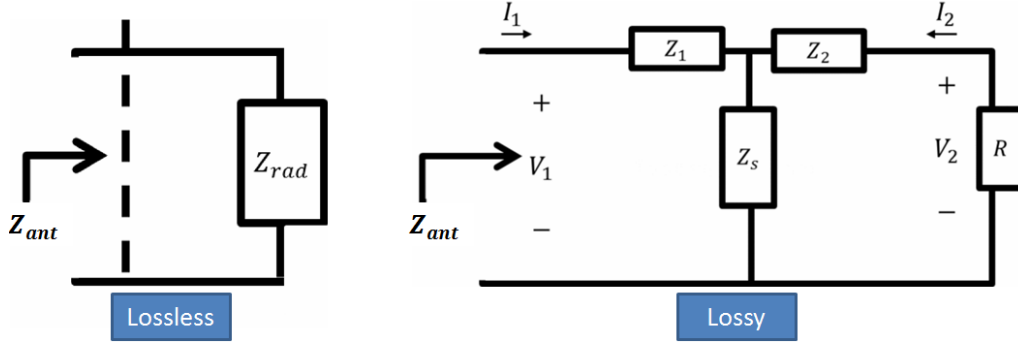


Figure 3.1: The circuit model for a lossless (left) and a lossy (right) antenna. Z_{ant} is the input impedance of the antenna which is approximated by Z_{avg} (which also includes short orbit effect in addition to Z_{ant}) in RCM normalization process, Z_{rad} is the radiation impedance which describes the feature of the port, and R is the real part of Z_{rad} that represent the power loss due to radiation. Figure 4, 5 in [7].

since it explicitly shows how it is calculated with experimental data.

In short, $\mathbf{Z}_{avg} = \langle \mathbf{Z}_{cav} \rangle_{realizations} = \mathbf{Z}_{ant} + \text{short orbits}$, where $\mathbf{Z}_{ant} = \mathbf{Z}_{rad}$ only when antenna is lossless. With lossless ports, where $\mathbf{Z}_{rad} = \mathbf{Z}_{ant}$, we use \mathbf{Z}_{avg} , which includes \mathbf{Z}_{ant} and short orbit effects, to normalize \mathbf{Z}_{cav} , which is how it is written in Equation (3.1). Lossless ports are implicitly assumed in most cases where \mathbf{Z}_{avg} appears in the RCM equation without η . But with lossy ports, where $\mathbf{Z}_{rad} \neq \mathbf{Z}_{ant}$, we need to modify the RCM equation before we can use \mathbf{Z}_{avg} again.

3.1.2 Radiation Efficiency η in One-port Systems

This section is a brief summary of Bisrat's derivations in [7] Section III.

The circuit models for lossless and lossy antennas are shown in Figure 3.1 with a T-network, comprising of three complex impedance Z_1 , Z_2 and Z_s , to represent a general lossy antenna on the right side. Z_{ant} is the input impedance of the antenna which is approximated by Z_{avg} (which also includes the short orbit effect in addition

to Z_{ant}) in the RCM normalization process, Z_{rad} is the radiation impedance which describes the feature of the port, and R is the real part of Z_{rad} that represents the power radiated to free space. Based on the definition of radiation efficiency, we have

$$\eta = \frac{P_{\text{rad}}}{P_{\text{in}}} = \frac{|I_2|^2 R}{|I_1|^2 \text{Re}[Z_{\text{ant}}]},$$

where I_1 and I_2 are the current flowing into the antenna and the current flowing through the radiation resistance R respectively. We have the conservation of voltage across the loop consisting of Z_s , Z_2 and R that gives $0 = (I_1 + I_2)Z_s + I_2(Z_2 + R)$, thus $|I_2/I_1| = |Z_s/(Z_s + Z_2 + R)|$, and

$$\eta = \frac{R}{\text{Re}[Z_{\text{ant}}]} \left| \frac{Z_s}{Z_s + Z_2 + R} \right|^2. \quad (3.3)$$

The input impedance looking into the antenna, when the antenna is radiating into free space, is

$$\begin{aligned} Z_{\text{ant}} &= Z_1 + \frac{Z_s(Z_2 + R)}{Z_s + (Z_2 + R)} \\ &= Z_1 + Z_s - \frac{Z_s^2}{Z_s + Z_2 + R}, \end{aligned} \quad (3.4)$$

If the antenna is put inside a cavity with normalized impedance ξ , a unitless quantity whose PDF is predicted by the loss parameter α , then the radiation resistance R now sees frequency dependent fluctuations due to the coupling with the cavity modes. So we replace R with $R\xi$, a combination of the antenna's slowly varying (in frequency) radiation resistance and the cavity's rapidly frequency dependent

modes, which are described by RMT, leading to

$$Z_{\text{cav}} = Z_1 + Z_s - \frac{Z_s^2}{Z_s + Z_2 + R\xi}.$$

The PDF of ξ depends only on α , which has been studied extensively in previous research. In the high loss regime, the PDFs of $\text{Re}[\xi]$ and $\text{Im}[\xi]$ are both Gaussian distribution centered at one and zero, respectively, and has a variance of $1/\pi\alpha$, i.e. $\text{Re}[\xi] \sim N(1, 1/\pi\alpha)$ and $\text{Im}[\xi] \sim N(0, 1/\pi\alpha)$. Thus for high α values, we can write $Z_{\text{cav}} = Z_1 + Z_s - Z_s^2/(Z_s + Z_2 + R(1 + \delta\xi))$, where $\delta\xi = \xi - 1$ is very close to zero, and expand it with respect to $\delta\xi$ using Taylor series to the first degree, i.e.

$$\begin{aligned} Z_{\text{cav}} &= Z_1 + Z_s - \frac{Z_s^2}{Z_s + Z_2 + R + R\delta\xi} \\ &= Z_1 + Z_s - Z_s^2 \left(\frac{1}{Z_s + Z_2 + R} - \frac{R\delta\xi}{(Z_s + Z_2 + R)^2} \right) \\ &= Z_1 + Z_s - \frac{Z_s^2}{Z_s + Z_2 + R} + \frac{Z_s^2 R \delta\xi}{(Z_s + Z_2 + R)^2} \end{aligned} \quad (3.5)$$

Apply Equation (3.3) and (3.4) to the above expression, then we have

$$Z_{\text{cav}} = Z_{\text{ant}} + \eta \text{Re}[Z_{\text{ant}}] e^{i\phi} \delta\xi, \quad (3.6)$$

where ϕ is the phase of $Z_s^2/(Z_s + Z_2 + R)^2$. Since $\delta\xi = \xi - 1 \sim N(0, 1/\pi\alpha) + jN(0, 1/\pi\alpha)$ has its real and imaginary part both being i.i.d, the phase of $\delta\xi$ is uniformly distributed. Thus $e^{i\phi} \delta\xi$ and $\delta\xi$ have the same statistical properties. So

for all practical purposes, we can simplify the expression for Z_{cav} to

$$Z_{\text{cav}} = Z_{\text{ant}} + \eta \text{Re}[Z_{\text{ant}}] \delta \xi, \quad (3.7)$$

which is the Equation (4) in Ref. [7].

3.1.3 Radiation Efficiency $\boldsymbol{\eta}$ in Multi-port System

To extend the η -adjusted Z_{cav} expression from one-port systems to multi-port systems, we first write η in the matrix form

$$\boldsymbol{\eta} = \begin{bmatrix} \eta_{11} & 0 & \dots & 0 \\ 0 & \eta_{22} & \dots & 0 \\ \vdots & \vdots & \ddots & \vdots \\ 0 & 0 & \dots & \eta_{NN} \end{bmatrix},$$

for a N-port system where η_{ii} is the radiation efficiency for the i^{th} port. Then we write all the scalar multiplications in Equation (3.7) into matrix form to obtain Equation (3.2) at the beginning of the section. The off-diagonal terms are all set to zero because there's no clear physical meaning for them, and that this diagonal form of $\boldsymbol{\eta}$ works pretty well in the analysis of the experimental data.

3.1.4 Scaling Relation Between α and η

For a high loss one-port system with a lossy port, the measured data contains lossiness from two components, the antenna and the cavity, and is quantified by the

radiation efficiency η and the cavity's loss parameter α respectively. Higher η value means a less lossy antenna and higher α value means a more lossy cavity. Given an ensemble of data there must be a pair of η and α values such that the PDF of the normalized impedance ξ , calculated according to Equation (3.2) with the η value, is predicted by the α value, i.e. (η, α) is a RCM description of the data's statistical properties. However if we let $\eta' = \eta + \Delta\eta$, we can still find a certain $\alpha' = \alpha + \Delta\alpha$ such that the ξ' , calculated with η' , also matches with the RCM prediction. In fact, there's a series of such pairs (α_i, η_i) that are all valid RCM descriptions for the same ensemble of data. This is because, without further information about η or α , we have the freedom to distribute the total lossiness of the whole system to the lossy antenna and the lossy cavity in any proportion. More specifically, α/η^2 is a constant for high loss systems which we will show below.

According to Equation (3.2), we have

$$\xi - 1 = \frac{Z_{\text{cav}} - Z_{\text{avg}}}{\eta \text{Re}[Z_{\text{avg}}]} = (\xi_0 - 1)/\eta \quad (3.8)$$

for a one port high loss system where $\xi_0 = (Z_{\text{cav}} - Z_{\text{avg}})/(\text{Re}[Z_{\text{avg}}]) + 1$ is the “unadjusted” normalized impedance. We can estimate the α from the variance of the ξ (Appendix B Method 4 in Ref. [2]) by

$$\begin{aligned} \alpha &= 1/(\pi\sigma_{\text{Re}[\xi]}^2) &= 1/(\pi\sigma_{\text{Im}[\xi]}^2) \\ &= \eta^2/(\pi\sigma_{\text{Re}[\xi_0]}^2) &= \eta^2/\pi\sigma_{\text{Im}[\xi_0]}^2 \end{aligned}$$

Since ξ_0 is independent of the choice of α or η , its variance is a known constant

for a given ensemble. So $\alpha/\eta^2 = 1/(\pi\sigma_{\text{Re}[\xi_0]}^2) = 1/\pi\sigma_{\text{Im}[\xi_0]}^2$ is a constant. It makes sense that a higher η , meaning a more efficient and less lossy antenna, leads to a higher α , meaning a more lossy cavity, because the total lossyness of the system is fixed for a given ensemble of data. Thus to determine the actual pair of (η, α) more information regarding η or α is required.

3.2 Applying Radiation Efficiency η to Experimental Data

The purpose of introducing the radiation efficiency η is to separate the lossiness of the antenna from that of the cavity and to obtain the normalized impedance statistics for the cavity, which is our main interest. In the experimental setup, the electromagnetic wave is remotely injected into the cavity through a free-space propagation path, consisting of the source horn antenna, the collimating teflon lens, the focusing lens at the other end and the receiving horn antenna. This setup, shown in Figure 2.7, is what we called the “remote injection” setup. These free-space paths are lossy and are considered as part of the “antennas”. The two-port cavity has two such lossy paths connected to each port that significantly increase the effective loss parameter α if we consider them as a whole. The measured overall effective α is about 30 while we are expecting an α value of about 5 for the scaled cavity. We’ll show that after applying the right η values to the experimental data, the scaled cavity extracted α becomes about 6 at room temperature, and is 3.6 when cavity is cooled to 10 Kelvin, a much more reasonable result.

To determine α using the RCM normalization process, we first recall the following expression for the normalized impedance ξ from Equation (1.4), which was obtained in Refs. [6, 23],

$$\xi = (\text{Re}[\mathbf{Z}_{\text{avg}}])^{-1/2}(\mathbf{Z}_{\text{cav}} - j\text{Im}[\mathbf{Z}_{\text{avg}}])(\text{Re}[\mathbf{Z}_{\text{avg}}])^{-1/2}$$

where \mathbf{Z}_{cav} is the measured cavity impedance, \mathbf{Z}_{avg} is the ensemble average of \mathbf{Z}_{cav} over many stirrer positions. \mathbf{Z}_{avg} represents the system-specific information, such as the coupling between the ports and the cavity, that the RCM captures and removes from the data to reveal the underlying universal fluctuations of the impedance. Prior work has established that the cavity statistical properties are independent of port location and type [6] and the RCM normalization process works well even for superconducting cavities [64]. However, we note that in Refs. [6, 23], Eq. (1.4) was derived assuming lossless ports, hence for our remote injection setup we first need to modify the normalization Eq.(1.4) to compensate for the loss during the free-space propagation path, which resulted in Eq.(3.2).

There are two distinct loss contributions in our experiment. The first is that intrinsic to the complex enclosure, described by the loss parameter α , which dictates the RMT distribution of impedance fluctuations. The second is due to the power lost in the extended "ports" in our experiment - namely the free-space propagation paths between the mm-wave transceivers and the entrances to the cavity. This latter loss mechanism has no influence on the statistical fluctuations of the enclosure, and is parameterized by η . A proper and consistent partitioning of these losses is required to correctly describe the measured impedance fluctuations over the entire frequency and temperature range of the measurements.

To obtain the η value corresponding to the free-space path, we use a fitting process as described in section 3.2.2. Then in section 3.2.3 we verify that η exclusively quantifies the lossiness of the free-space path, i.e. the lossy antenna, and is independent of the cavity's α . Finally we apply the η values to the experimental

data for the remote injection setup.

3.2.1 Calculating Loss Parameter Through Time-domain Energy Decay Time τ

In 3D, $\alpha = k^2/(\Delta k_n^2 Q) = k^3 V/2\pi^2 Q$ where k is the wave number, $\Delta k_n^2 = 2\pi^2/kV$ is the eigenmodes' mean spacing, $Q = \omega\tau$ [65] is the quality factor, ω is the angular frequency and τ is the averaged energy decay time. Most of the quantities are known directly, but only τ needs some effort to determine.

To estimate τ over a given frequency range, we plot the inverse Fourier transform of the measured S-parameters (from 75 GHz to 110 GHz) on a logarithmic scale versus time for an ensemble of 9 realizations, as shown in Fig.3.2. These plots are equivalent to bandwidth-limited impulse responses in the time domain. The plots for transmission ($|S_{12}|=|S_{21}|$, Fig.3.2 (a)) start with a short delay followed by a exponential decay with a slope of $-1/(2\tau)$. The factor of 2 comes in because τ is the decay time for energy but the y-axis is proportional to the magnitude of voltage. The plots for reflection ($|S_{11}|$, Fig.3.2 (b)) show an initial prompt response from the antenna, which contains information about the antenna's radiation impedance Z_{rad} [7, 66, 67], followed by the same exponential decay. Notice that, even though the 9 curves are somewhat different from each other, their average is very well approximated by a straight line on this log-linear plot. The fluctuations in each curve represent the cavity modes, which are randomly perturbed. Note that this Q is an average over all the modes in the 75 - 110 GHz frequency range.

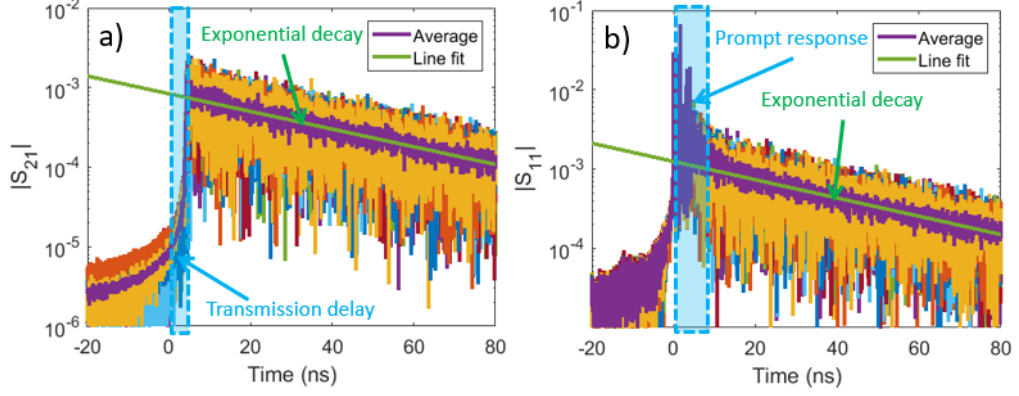


Figure 3.2: The inverse Fourier transform of the measured S-parameters give the value of τ from each fit in log-scale versus time. a) For the case of transmission and b) for the case of reflection of the $s = 20$ scaled enclosure measured through remote injection. Data from 9 realizations at room temperature are plotted with different colors. The purple line is the average, and the green line is the linear fit for the energy decay portion of the average. The slope of the fitted line is $-1/2\tau$, where τ is the energy decay time of the cavity. The time domain response inside the blue dashed box in (b), labeled 'Prompt response', arises from the impedance mismatch between the external transmission channel and the cavity. This information is captured in Z_{avg} .

The same technique is applied to the thousands of S-parameter data sets collected during a cool-down/warm-up temperature cycle, which ranges from room temperature to 15 Kelvin to room temperature, as shown in Fig.3.5 by the blue solid line. It is seen that by choosing a temperature, we can set the cavity α to any value between 3.3 and 5.6. Note that this determination of α_Q is independent of the loss introduced by the free-space propagation paths.

3.2.2 Fitting Radiation Efficiency η

In this setup, the frequency range is 75 - 110 GHz with a center frequency of $f = 92.5$ GHz, the volume is $V = 1.289 \times 10^{-4} \text{ m}^3$ and the quality factor obtained from above is about 8450, giving a loss parameter of $\alpha_Q = k^3 V / (2\pi^2 Q) = 5.6$ (α_Q denotes

calculated from the quality factor) at room temperature. Thus, by using an RCM Monte Carlo simulation, we can obtain a prediction for the universally fluctuating impedance PDFs (Eq. 1.4) of a 2-port system's normalized impedance with $\alpha = 5.6$, as shown in Fig.3.3 with the solid lines. Then we find the best η_{11} and η_{22} values such that the normalized impedances, calculated with $\boldsymbol{\eta} = \begin{bmatrix} \eta_{11} & 0 \\ 0 & \eta_{22} \end{bmatrix}$ according to Eq.(3.2) using the remote injection experimental data, best approximate the PDFs produced by the RCM simulation results.

The best fit values are $\eta_{11} = 0.14$, $\eta_{22} = 0.19$ and the resulting normalized impedance PDFs are plotted in Fig.3.3 as dotted lines. The agreement is good, but not perfect. We believe that the deviations in $\text{Re}[\xi_{11}]$ and $\text{Re}[\xi_{22}]$ statistics (Fig.3.3 (a)) are because Eq.(3.2) only works for high loss cavities ($\alpha \gg 1$) [7], and $\alpha = 5.6$ in our case is barely in this limit. Applying the η correction changes the variance of $\text{Re}[\xi_{11}]$ and $\text{Re}[\xi_{22}]$, but does not change their PDF peak location. Before applying the η correction, the fluctuations of $\text{Re}[\xi_{11}]$ and $\text{Re}[\xi_{22}]$ are narrowly centered around 1 and remain so afterwards, deviating from the peak location in the simulation. (Efforts are underway to further generalize the treatment of lossy ports in the RCM to accommodate lower loss cavities.)

The solid and dotted lines for $\text{Im}[\xi_{11}]$ and $\text{Im}[\xi_{22}]$ in Fig.3.3 lie right on top of each other, as well as the curves for the real and imaginary parts of ξ_{12} and ξ_{21} (omitted in Fig.3.3 for clarity), proving that the fitted $\boldsymbol{\eta}$ successfully separates the effects of the lossy free-space path from the cavity losses. We have applied this $\boldsymbol{\eta}$ correction to all other data sets in the same experiment, assuming that the propagation paths are not perturbed as the temperature varies. The resultant α_{fit}

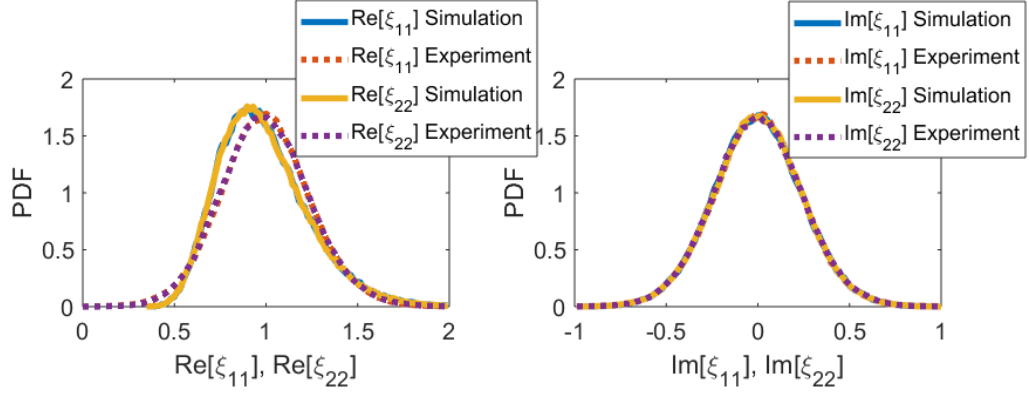


Figure 3.3: Comparison between the normalized impedance PDF for a 2-port system from a RCM Monte Carlo simulation with $\alpha = 5.6$, in solid lines, and that from a normalization process of experimental data with $\eta_{11} = 0.14$ and $\eta_{22} = 0.19$, in dotted lines.

deduced in this manner is plotted in Fig.3.5 as the red dotted line, which agrees well with the α_Q curve calculated from the first method.

To maximize the tunable range of the α values, we also vary the cavity wall material in order to vary ohmic loss. We performed the cool-down experiment with the same miniature cavity with three different wall material conditions: copper wall (α results shown in Fig.3.5), mechanically polished copper wall, and wall covered with aluminum foil. The polishing reduces the surface roughness and thus reduces surface losses [58, 59]. The overall range of achievable α values are shown in Fig.4.3.

Notice that the experimental PDF for the real part of ξ_{11} and ξ_{22} deviate from the simulation result. This is because in the derivation of Equation (3.2) α is assumed to be high enough such that the PDF for the real part of ξ_{11} and ξ_{22} is a Gaussian distribution centered at 1. Introducing $\boldsymbol{\eta}$ only changes the width of the Gaussian curve, and in turn changes α , but not its center, leading to the difference we see in the figure.

3.2.3 η 's Independence From Cavity's α

The previous section shows how to calculate the loss parameter α from time domain power decay time τ , and how to fit the radiation efficiency η from a comparison between the Monte Carlo RCM simulation and the experimental data. But before we move forward, it is necessary to demonstrate that the η values obtained in this way are an accurate and unique representation of the free-space paths in the setup.

To do this, we performed the following experiment. First we setup a one-sided remote injection experiment, in which port 2 of the cavity is directly connected to the source while port 1 is connected to a free-space propagation path before going to the receiver. Thus η_{22} must be equal to 1 and η_{11} is some value between 0 and 1. Then we follow the fitting process discussed in section 3.2.2 to find out the values of $\eta_{11,\text{empty}}$ and α_{empty} when the cavity is empty as it is, and $\eta_{11,\text{absorber}}$ and α_{absorber} when a small piece of microwave absorber is added into the cavity while the free-space path is unchanged. The expectation is that $\eta_{11,\text{empty}} = \eta_{11,\text{absorber}}$ since the free-space path is unchanged, and $\alpha_{\text{empty}} < \alpha_{\text{absorber}}$ since the absorber brings more loss to the cavity.

The experimental result shows that $\eta_{11,\text{empty}} = 0.3329$ and $\eta_{11,\text{absorber}} = 0.3212$ which are pretty close. The loss parameter values are $\alpha_{\text{empty}} = 4.7$ and $\alpha_{\text{absorber}} = 13.3$ which are dramatically different from each other. A comparison between the normalized impedances for the direct injection experiment and the empty remote injection experiment is plotted in Figure 3.4. Notice that the empty remote injection experimental data is processed using $\eta_{11,\text{absorber}}$, and yet it still matches with the

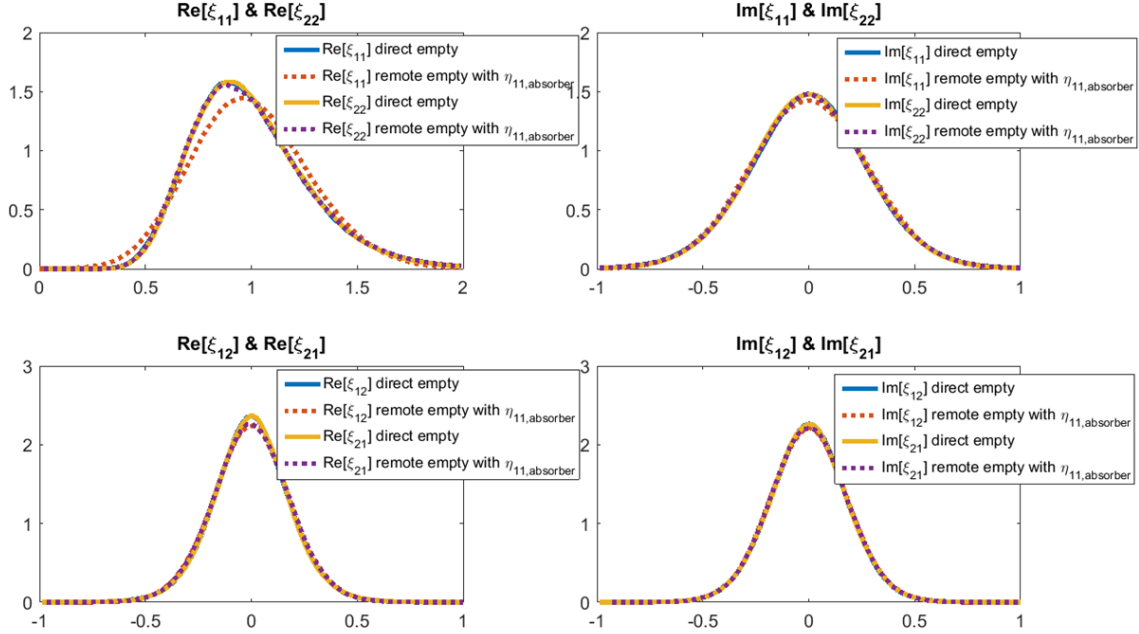


Figure 3.4: The comparison between the normalized impedance PDF from a direct injection experiment with an empty cavity (solid lines), and that from a one-sided remote injection experiment with an empty cavity (dotted lines). The remote injection data is processed using the radiation efficiency $\eta_{11,absorber}$ obtained from the one-sided remote injection with an absorber.

direct injection result pretty well, confirming that the value of η is independent from the cavity α .

3.2.4 Apply η to Experimental Data

Using the fitting process in section 3.2.2, we determined that the η values for the remote injection experiment with unpolished copper cavity are $\eta_{11} = 0.14$ and $\eta_{22} = 0.19$, and calculated the α values during the cool-down and warm-up process, assuming that η does not change during cooling, which is plotted in Figure 3.5 yellow dotted line. It is the same as the middle curve (cyan, labeled as “Cu cool-down” and “Cu warm-up”) in Figure 4.3, which is plotted against temperature

instead of time. For comparison, we also plot the α values if η is chosen to be larger (red dotted line) or smaller (purple dotted line). It is clear that larger η leads to larger α values for the same set of data, which is expected because α/η^2 is constant for a given ensemble data set as discussed in section 3.1.4. The solid blue curve is α_Q calculated from the time domain energy decay time method as described in section 3.2.2. As the solid blue curve and the yellow dotted curve almost overlap each other, the α values from these two methods agree very well. This in turn proves that the η adjustment to the original RCM is valid and the fitting process to determine η is correct.

Notice that the radiation efficiency η_{11} and η_{22} values are unchanged during one cool-down experiment, but they could be different for different cool-downs. For example, we later mechanically polished the $s = 20$ copper cavity's inside wall to a mirror-like finish and repeated the cool-down experiment. This time the radiation efficiency values are $\eta_{11} = 0.162$ and $\eta_{22} = 0.170$, slightly different from the unpolished copper cavity experiment. This is because the η values are largely dependent on the loss during the free-space propagation path, which can be different from one experiment to another since the path is constructed manually before each experiment and is disassembled afterwards. We tried to make each path construction identical but the process to align the antenna and lens is not precisely reproducible.

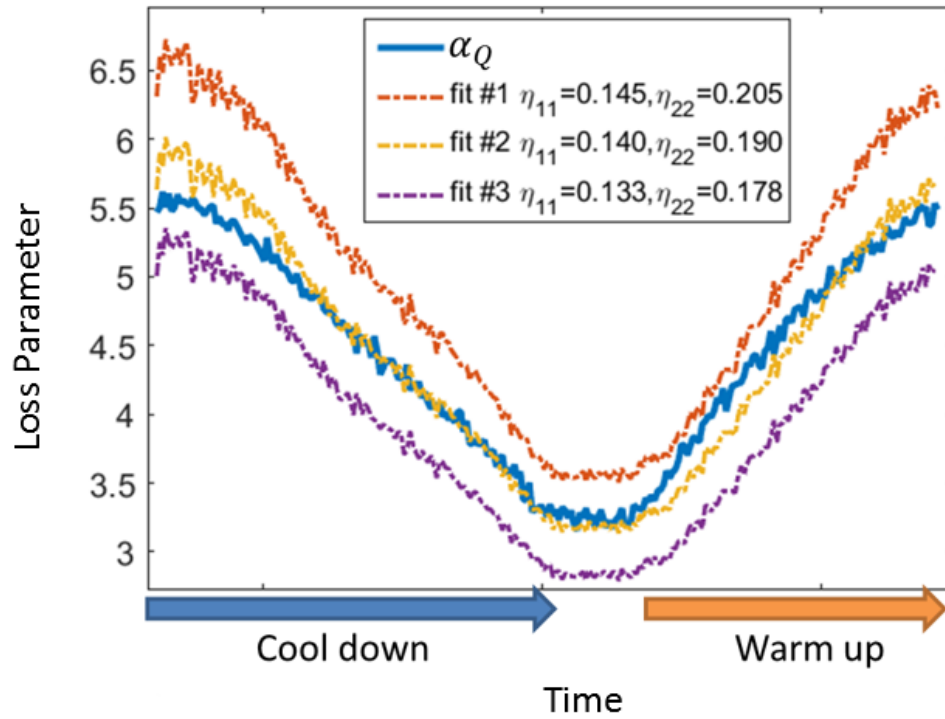


Figure 3.5: A comparison between α values calculated from different methods as a function of time during a cycling of the dilution refrigerator hosting the scaled cavity. Blue solid line: calculated from time domain energy decay time method; Dotted lines: calculated from RCM normalization process with various values of η .

Chapter 4: Single Scaled Cavity Experiment

In Chapter 2 we introduced the scaled cavity experimental setup that can be used to test the Random Coupling Model predictions in a scaled-down cavity. Then we modified the RCM normalization equation in Chapter 3 to include the case of lossy ports (such as the free-space propagation path in the remote injection setup) by adding a radiation efficiency term η . With the proper experimental setup and the analysis tools in place, we can now compare the statistical properties of the full-scale cavity and the scaled-down cavity. Demonstrating the identical statistics between these two cases is the foundation for all future study involving scaled-down cavities.

4.1 Full-Scale Cavity Analysis

The full-scale cavity is a 66 cm X 122.5 cm X 127.5 cm aluminum cavity measured at 3.7 ~ 5.5 GHz (WR187 band). To have a one-on-one comparison with our scaled-up frequency range 75 ~ 110 GHz, we analyzed the data from 3.75 to 5.5 GHz. Our collaborators, Zachary Drikas and Jesus Gil Gil at NRL, measured the full-scaled cavity with various numbers of microwave absorbers inside, from 1/4 absorber up to 16 absorbers, as well as the empty cavity. The resulting α ranges from 1.56 (empty cavity) to 16.86 (16 absorbers), as shown in figure 4.1 left plot. It is almost as if the α values are linearly increasing with the number of absorbers.

4.1.1 Frequency Dependent Loss Parameter

We also divided the whole frequency range into $N = 10$ segments, 175 MHz for each one, to look at the frequency dependent $\alpha_N(f)$ which is plotted in figure 4.1 right plot. $\alpha_{N=10}(f)$ is increasing with frequency f , indicating higher loss at higher frequency, which is expected. Notice that for the case with 16 absorbers the higher end of the frequency range hits the upper bound for the simulation $\alpha_{\max} = 20$ so it appears to be flat. The actual α value should continue to increase beyond 20.

An interesting observation in the $N = 10$ case is that if we take the mean of the frequency dependent α values, i.e. $\alpha_{N=10,\text{avg}} = 1/10 \times \sum_{i=1}^{10} \alpha_{N=10}(f_i)$, and compare it with the frequency averaged $\alpha_{N=1}$ in the $N = 1$ case, we find that $\alpha_{N=1} = \alpha_{N=10,\text{avg}}$. The only exception is for the case with 16 absorbers where the higher frequency α values goes higher than the RCM simulation range, which is $\alpha_{\max} = 20$, so it is capped. Since α is inherently frequency dependent, in some sense the calculated α is always an average over a certain frequency range, large or small. This result confirms that calculating $\alpha_{N=1}$ from data in a single large frequency range is equivalent to taking the average of $\alpha_N(f)$ values calculated from N smaller frequency bands that subdivide the large range. This is true even if $\alpha_N(f)$ ranges from 7 to 15 and yet $\alpha_{N=1}$ is equal to $\langle \alpha_N(f) \rangle$. My colleague Ziyuan Fu demonstrated a similar frequency averaging effect for microwave graphs, as explained in Ref. [68]

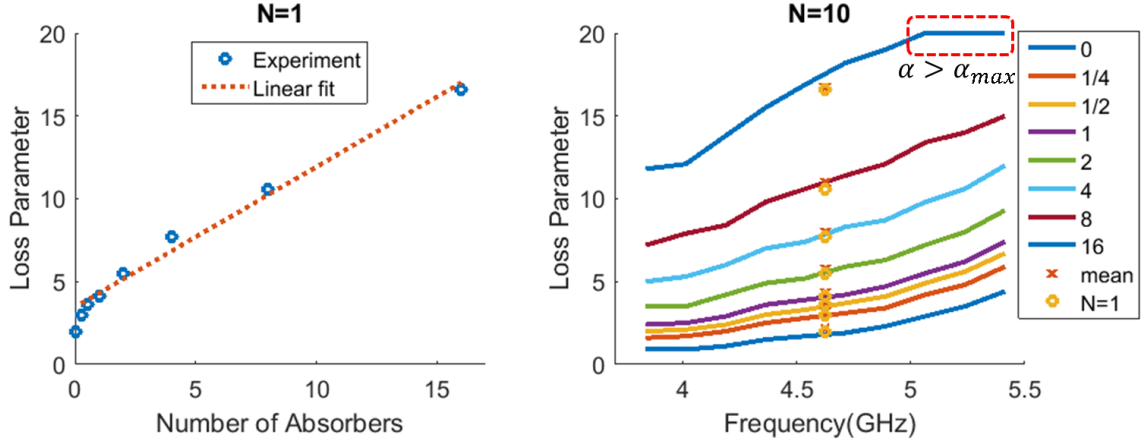


Figure 4.1: The full-scale cavity α measured by Zachary Drikas and Jesus Gil Gil at NRL with various number of absorbers inside. The left side plot is the average α for the whole frequency range, i.e. number of frequency segments $N = 1$. The right side plot is the α for $N = 10$ frequency segments.

4.1.2 Fitting Error

It is worth looking at the α fitting process and the error to understand how well the RCM prediction matches with the experimental data and how reliable the above result is.

In many publications about the Random Coupling Model, such as in Refs. [3, 23], a guideline is provided to generate the normalized impedance ensemble by purely numerical calculations according to the Random Matrix Theory and the Random Coupling Model. A Matlab script implementing such a process is presented in Appendix A. The result is a library that maps a certain α value to its corresponding normalized impedance statistics, in this case 8 PDF curves for the real and imaginary parts of the fluctuating ξ_{11} , ξ_{12} , ξ_{21} and ξ_{22} .

Then we normalize the experimental data according to equation 1.4, or 3.2 for systems with lossy ports, to obtain the PDFs for the cavity's normalized impedances,

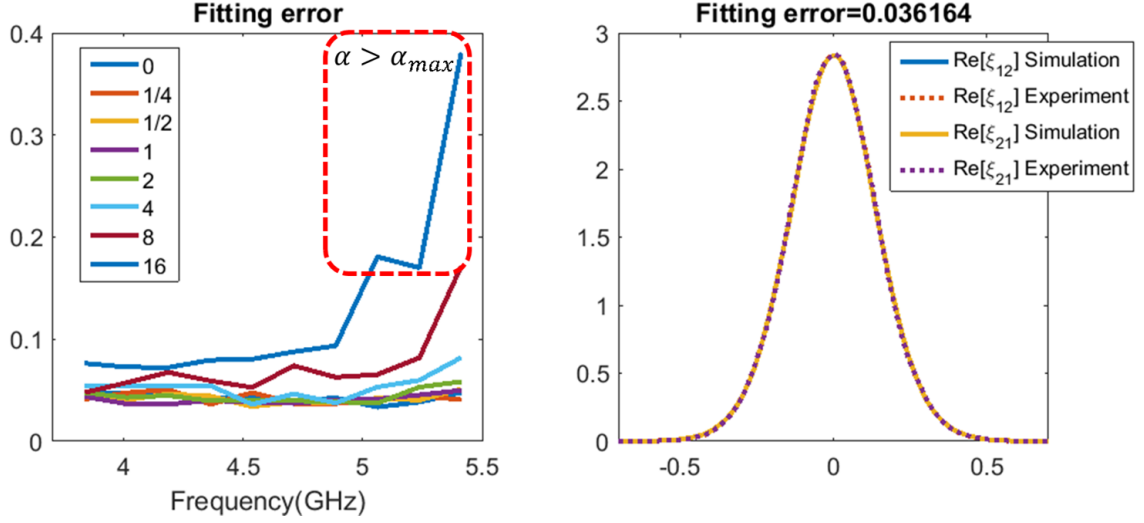


Figure 4.2: The fitting error for calculating the $\alpha_{N=10}(f)$ values for the full-scale cavity is mostly around 0.05. The few high error data points are for $\alpha > \alpha_{max}$ over the limit of the simulation α range. The right plot shows a typical case of the comparison between the PDF curves for the 5th frequency segment where the fitting error is 0.036164.

$f_{\xi, \text{experiment}}$. We compare these PDFs with the RCM simulation result, $f_{\xi, \alpha, \text{simulation}}$ which depends on the α value that are specified, and find out which α 's PDFs curves best matches with the experimentally obtained ones, giving us the fitted α value, i.e.

$$\alpha_{\text{fit}} = \arg \min_{\alpha} (f_{\xi, \text{experiment}} - f_{\xi, \alpha, \text{simulation}}).$$

The fitting error is $f_{\xi, \text{experiment}} - f_{\xi, \alpha_{\text{fit}}, \text{simulation}}$ and is plotted in figure 4.2 left plot. Most of the fitting error values are around 0.05 with a few exceptions for the 16 absorbers case in the higher frequency segments where $\alpha > \alpha_{max}$ is over the limit of the simulation α range. If we look at a typical fitting case, such as the 5th frequency segment where the fitting error is 0.036164, the PDF curves actually look pretty identical, confirming that the experimental data and the simulation result matches very well.

4.2 Miniature Cavity Analysis

The major difference in analyzing the full-scale and the miniature cavity data is the use of the radiation efficiency η . The miniature cavity experiment uses the remote injection setup which has a lossy free-space propagation path for the mm-wave and thus requires the RCM to include an additional term η to offset that extra loss. The theory and the experimental validation of the modified RCM is discussed in Chapter 3. In general, to analyze miniature cavity experimental data, we need to do the following:

1. Calculate the time-domain energy decay time τ then calculate the loss parameter α_Q by $\alpha = k^3V/2\pi^2Q$ where k is the wavenumber, V is the volume and $Q = \omega\tau$ is the quality factor, as discussed in 3.2.1.
2. Find the best η_{11} and η_{22} values such that the experimental normalized impedance PDFs measured with remote injections setup at room temperature match with the theoretical PDFs predicted by RCM for α_Q , as discussed in 3.2.2.
3. Apply the obtained η_{11} and η_{22} to all the data measured during the cool-down process to calculate the experimental normalized impedance statistics for the entire temperature range.

The data set for each temperature has a certain α value associated with it, giving us a library of data that can match systems with a wide range of α . On top of the temperature tuning, we also varied the miniature cavity wall material to include three different cases, aluminum, unpolished copper and mirror-like copper, to vary

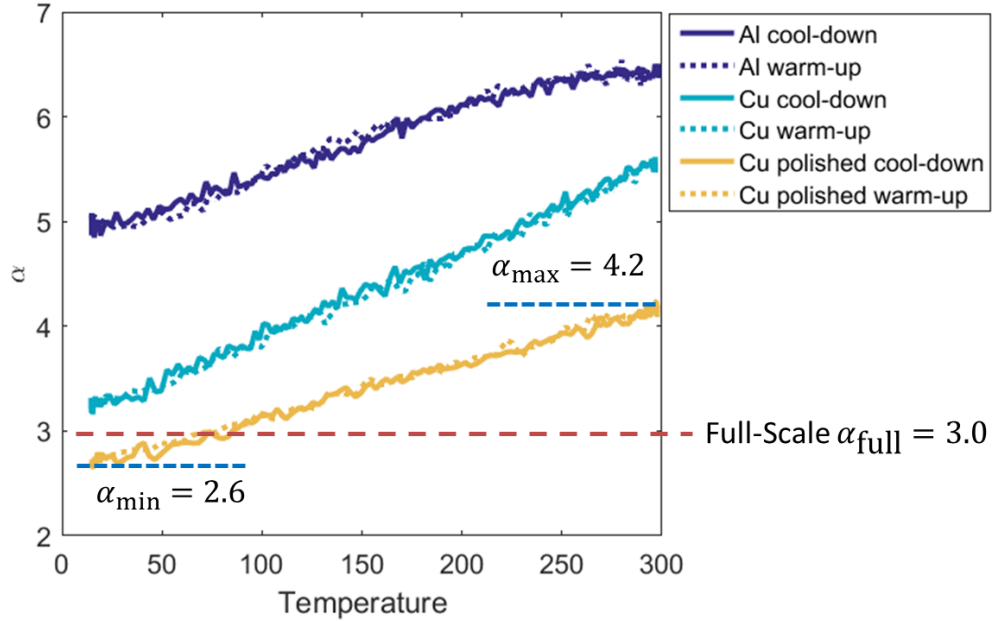


Figure 4.3: The tunable range of α values by using different wall material and varying temperature. The least lossy wall material is polished copper, which gives a range of $2.6 \leq \alpha \leq 4.2$, including the α_{full} for full-scale cavity with 1/4 absorber in its range. The plotted α is calculated from the time-domain energy decay time τ .

the surface resistance. The resulting α has a range of $2.6 \leq \alpha \leq 6.4$ as plotted in figure 4.3. The least lossy wall material is polished copper, which gives a range of $2.6 \leq \alpha \leq 4.2$, including the α_{full} for full-scale cavity with 1/4 absorber in its range.

4.2.1 Frequency Dependency of η and α

Similar to what's done in section 4.1.1, we divide the whole frequency range of 75 ~ 110 GHz into $N = 10$ segments and look at the frequency dependency of various parameters. Notice that the bandwidth for each segments is now 3.5 GHz, 20 times the bandwidth in the full-scale analysis due to the frequency scaling.

First, let's look at the radiation efficiency η_{11} and η_{22} . From equation 3.3, η is

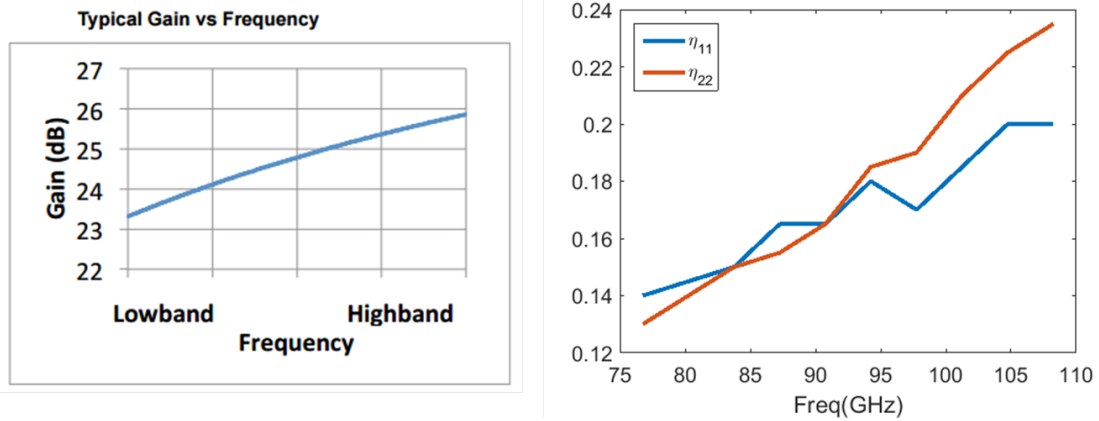


Figure 4.4: The horn antenna has higher gain at higher frequency band which results in higher radiation efficiency. Left plot taken from Virginia Diode, Inc documentation Nominal Horn Specifications [8].

also inherently frequency dependent. In our remote injection setup, the main factor of the port loss is the antenna and lenses' focusing ability and the alignment (which remains mostly unchanged during each cool-down experiment). Other minor factors include loss in the horn antenna and the dielectric loss in the Teflon lenses. At higher frequencies, the horn antenna has higher gain, according to the horn antenna vendor Virginia Diode, Inc's documentation which is shown in figure 4.4 left plot. So we expect higher η values close to 110 GHz. The calculated η values matches with our expectation very well, which is plotted in figure 4.4 right plot.

Then we plot the loss parameter α_τ , calculated from the time-domain energy decay method, and α_{fit} , calculated by fitting the normalized impedance with RCM simulation as discussed in section 4.1.2 for the full-scale cavity, as a function of frequency. The result, shown in figure 4.5, shows that higher frequency leads to higher α which is consistent with the full-scale case in figure 4.1. During the cool-down, the surface resistance of the metal wall keeps dropping and thus α lowers,

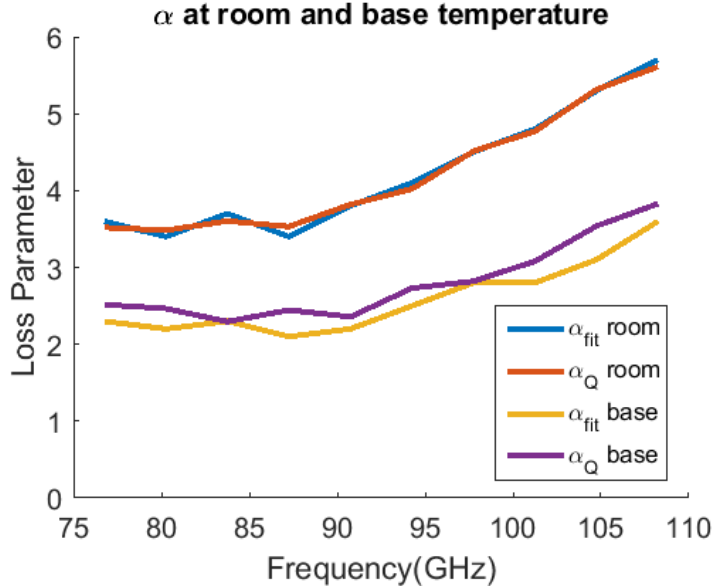


Figure 4.5: The frequency dependent loss parameter for the miniature cavity calculated from the time-domain energy decay time method, α_Q , and from fitting with RCM simulation results, α_{fit} .

until it reaches the base temperature that gives the lower bound of α .

4.3 Comparison Between Full-Scale and Miniature Cavity

The goal of the comparison is to make sure that the miniature cavity have the same statistical properties as the full-scale cavity, not only that they have the same α values but also has the same PDFs for the normalized impedances. For a single cavity, there's a known one-to-one relationship between the α and the PDFs, but it is not so clear what the PDFs should be for a network of cavities, such as a cascade of cavities. So having matching PDF curves is more relevant than having the same α values.

To compare the full-scale and the miniature cavity, we first choose a certain frequency range that we would like to look at. Then we normalize the measured

impedance in this range for the full-scale cavity. For the miniature cavity, there are two things that we can tune to calculate the normalized impedance, the wall material (aluminum, copper or polished copper) and the temperature (from 297 to about 10 Kelvin). By choosing the appropriate material and temperature, we can always find a set of miniature cavity experimental data that has the same statistics with the full-scale cavity.

Here are a few cases that illustrate how the miniature and the full-scale cavity have the same statistical properties.

4.3.1 Full-Scale Cavity with 1/4 absorber for $N = 1$ Frequency Segment

The loss parameter for the full-scale cavity with 1/4 absorber for the whole frequency range 3.75 ~ 5.5 GHz is $\alpha_{\text{full}, N=1} = 3.0$. From figure 4.3, $\alpha_{\text{full}, N=1}$ is within the range of the α values for the polished copper wall case near 100 Kelvin. After looking at the experimental data measured around that temperature, we find the best match at 103 Kelvin and the PDF for the normalized impedance $\text{Im}[\xi_{21}]$ is plotted in figure 4.6. These two PDFs agree with each very well, and they also match with the RCM predictions for $\alpha = 3.0$.

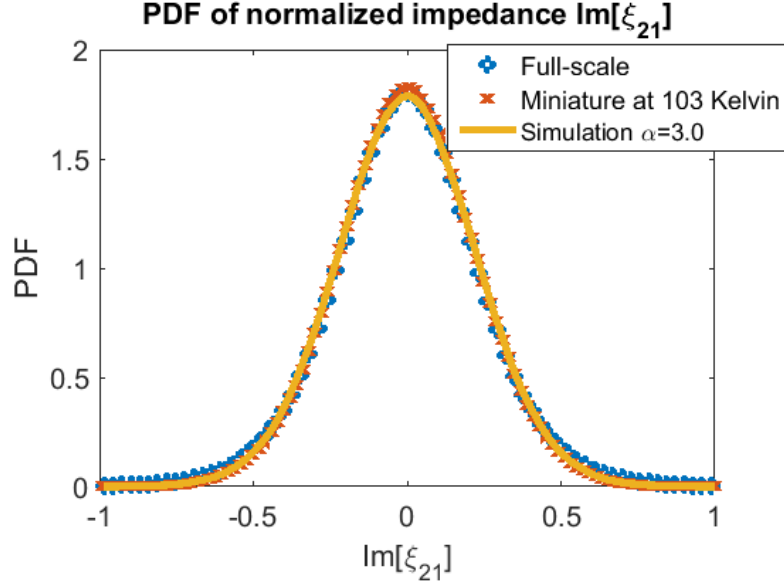


Figure 4.6: The comparison of PDFs for the normalized impedance $\text{Im}[\xi_{21}]$ for the full-scale cavity with 1/4 absorber, the miniature cavity at 103 Kelvin and the RCM simulation with $\alpha = 3.0$. The experimental data is selected from the whole frequency range ($N = 1$), i.e. 3.75 ~ 5.5 GHz for the full-scale cavity and 75 ~ 110 GHz for the miniature cavity.

4.3.2 Full-Scale Cavity with 1/4 absorber for $N = 10$ Frequency Segments

We divide the whole frequency range into $N = 10$ segments, each has a bandwidth of 175 MHz for the full-scale cavity and 3.5 GHz for the miniature cavity. The process is pretty much the same as the $N = 1$ case, only repeat it 10 times, one for each frequency band. In figure 4.7 we select the 5th, 8th and 10th frequency bands out the the 10 bands and plot the matching results. Each frequency band has a different α value (2.83, 4.19 and 5.82) and thus needs a different temperature (130, 217 and 297 Kelvin) to match with the full-scale statistics. They all match very well.

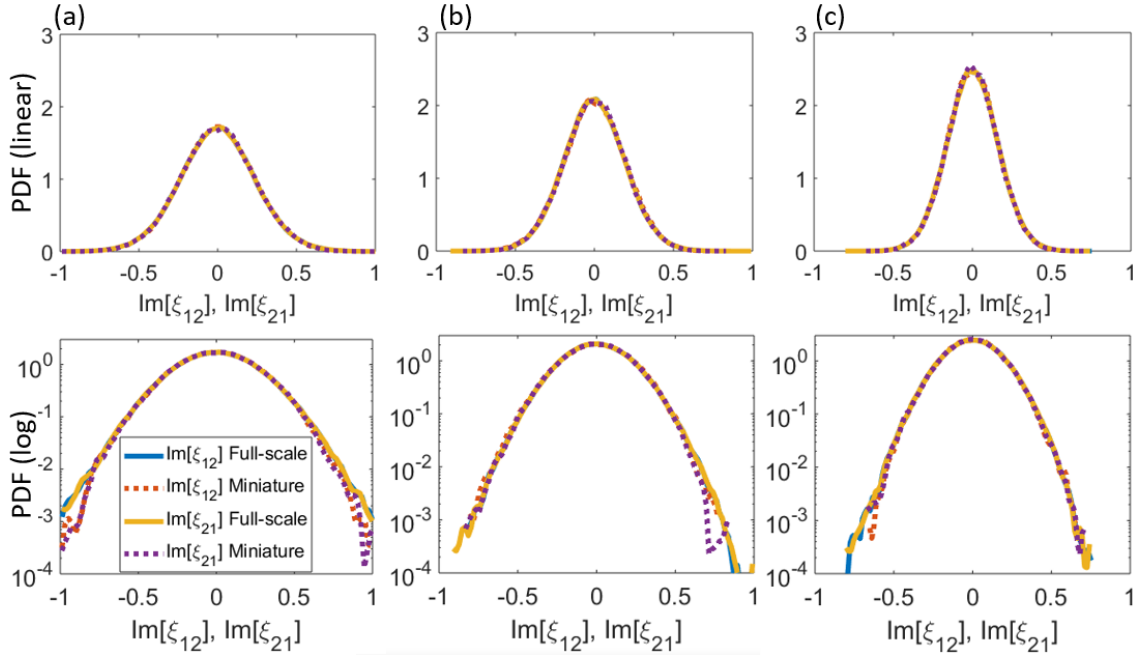


Figure 4.7: Comparison of the probability density function (PDF) for the imaginary part of the normalized impedance ξ_{12} and ξ_{21} between the full-scale cavity (solid line based on data) and the miniature cavity (dotted line based on data) for three different frequency bands (of the full-scale cavity) at different temperatures (of the scaled cavity). Top row shows the PDFs in linear scale while the bottom row shows the same PDFs in log scale. (a) $\alpha = 2.83$ within $[4.45, 4.625]$ GHz at 130 Kelvin, (b) $\alpha = 4.19$ within $[4.975, 5.15]$ GHz at 217 Kelvin and (c) $\alpha = 5.82$ within $[5.325, 5.5]$ GHz at 297 Kelvin. Notice that in each plot, all four curves collapse into one because they match each other very well.

4.4 α Range Limitation

As discussed in Chapter 3, the application of the radiation efficiency η is only valid for high α systems where $\alpha > 5$. As shown in figure 4.3 the miniature cavity's α is barely on the border. And for the frequency-dependency analysis result in figure 4.5 the α in the lower frequency range is definitely too small to be applicable for the radiation efficiency treatment. This is part of the reason why we only showed the PDF comparison for the upper half frequency bands in figure 4.7.

To have a better understanding of the effect of the radiation efficiency η at low α , we need to look at all the 8 PDF curves, the real and imaginary part of ξ_{11} , ξ_{12} , ξ_{21} and ξ_{22} .

4.4.1 Difference in $\text{Re}[\xi_{11}]$ and $\text{Re}[\xi_{22}]$

For the third plot in figure 4.7, the loss parameter is $\alpha = 5.82$ and its full 8-curve comparison is shown in figure 4.8. It is clear that the real part of ξ_{11} and ξ_{22} have big deviations, as also seen in figure 3.3 and 3.4. This is because $\text{Re}[\xi_{11}]$ and $\text{Re}[\xi_{22}]$ are supposed to be Gaussian distributions centered at one with equal variance $\sigma_{\text{Re}[\xi_{11}]}^2 = \sigma_{\text{Re}[\xi_{22}]}^2$ related to α by $\alpha = 1/(\pi\sigma_{\text{Re}[\xi_{11}]}^2)$. Adding the radiation efficiency into the equation only changes the variance of the distribution to $\sigma_{\text{Re}[\xi_{11}]}^2/\eta^2$, as stated in equation 3.8. So after the scaling by η , the adjusted PDF of $\text{Re}[\xi_{11}]$ and $\text{Re}[\xi_{22}]$ is still centered at one, as shown in figure 4.8 upper left plot. But the actual PDF is tilting more and more towards zero as α decreases and is no longer a Gaussian distribution, thus creating this difference between the experimental curves

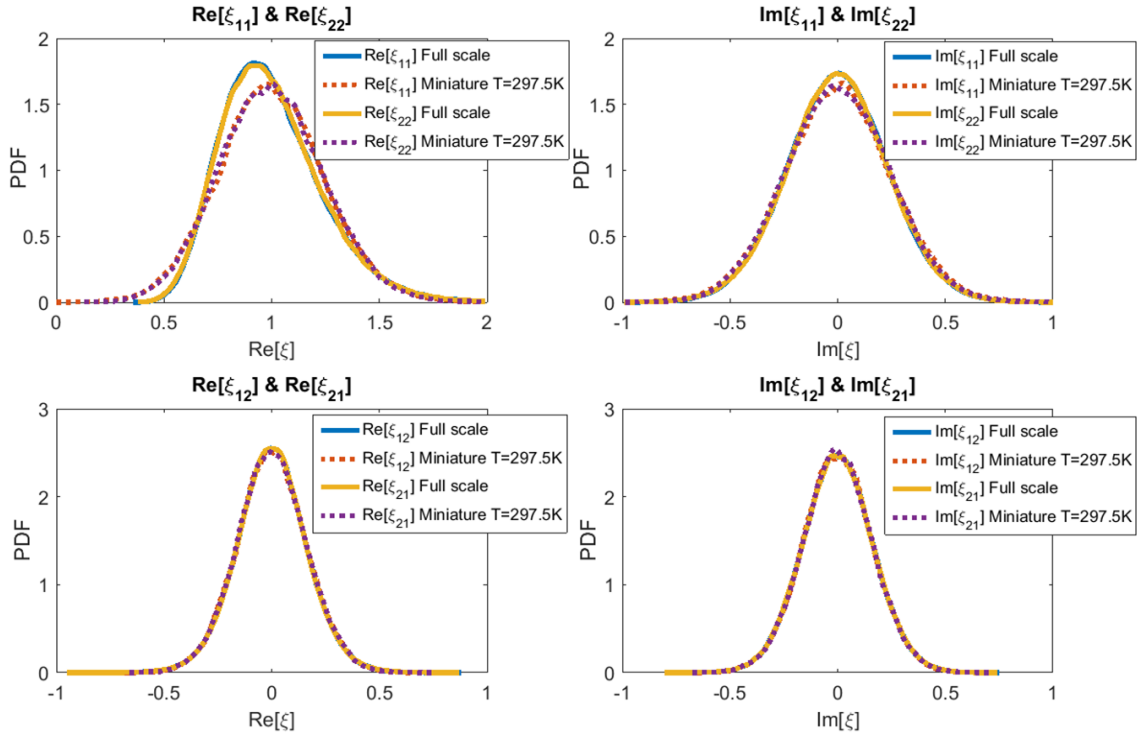


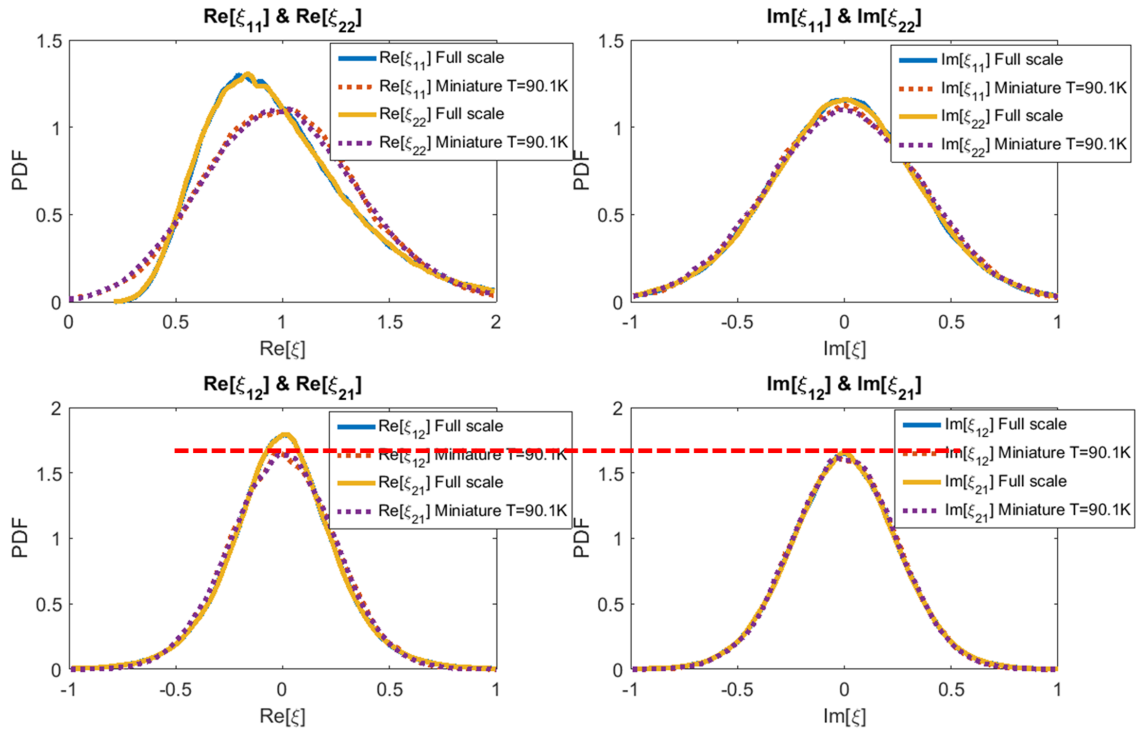
Figure 4.8: The comparison of all 8 PDFs for the normalized impedances, the real and imaginary part of ξ_{11} , ξ_{12} , ξ_{21} and ξ_{22} , for the full-scale cavity with 1/4 absorber and the miniature cavity. The experimental data are selected from [5.325, 5.5] GHz, the 10th segment of the $N = 10$ frequency segments, for the full-scale cavity and is selected from 297 Kelvin and [106.5, 110] GHz for the miniature cavity.

and the RCM simulation curves.

4.4.2 Difference in $\text{Re}[\xi_{12}]$, $\text{Re}[\xi_{21}]$ and $\text{Im}[\xi_{12}]$, $\text{Im}[\xi_{21}]$

Another effect of the radiation efficiency η is that the real and imaginary part of ξ_{12} and ξ_{21} are identical in the high α limit but start to be different in the low α cases. To see this, we look at the 4th of the $N = 10$ frequency segments in the full scaled cavity and compare its statistics with the miniature cavity at 90.1 Kelvin, as shown in figure 4.9.

We see that again the $\text{Re}[\xi_{11}]$ and $\text{Re}[\xi_{22}]$ are different, and we also see that



SS

Figure 4.9: The comparison of all 8 PDFs for the normalized impedances, the real and imaginary part of ξ_{11} , ξ_{12} , ξ_{21} and ξ_{22} , for the full-scale cavity with 1/4 absorber and the miniature cavity. The experimental data are selected from [4.275, 4.45] GHz, the 4th segment of the $N = 10$ frequency segments, for the full-scale cavity and is selected from 90.1 Kelvin and [85.5, 89] GHz for the miniature cavity.

the $\text{Re}[\xi_{12}]$ and $\text{Re}[\xi_{21}]$ are also different. Specifically, $\text{Re}[\xi_{12}]$, $\text{Re}[\xi_{21}]$ and $\text{Im}[\xi_{12}]$, $\text{Im}[\xi_{21}]$ are identical for the miniature cavity, but they are not for the full-scale cavity. This is because, similar to the case of $\text{Re}[\xi_{11}]$ and $\text{Re}[\xi_{22}]$, the miniature cavity's statistics of ξ_{12} and ξ_{21} are also scaled linearly according to η . In the high loss limit, the theoretical distribution of $\text{Re}[\xi_{12}]$, $\text{Re}[\xi_{21}]$, $\text{Im}[\xi_{12}]$ and $\text{Im}[\xi_{21}]$ are all the same, Gaussian distributions with the same variance and centered at zero. As α decreases, however, the real and imaginary parts starts to deviate from each other, as shown in figure 4.10. When $\alpha = 8$ the real and the imaginary parts are identical, but they start to differ when $\alpha = 5$ or even lower. In the extremely low loss case of $\alpha = 0.1$, $\text{Re}[\xi_{12}]$ and $\text{Im}[\xi_{12}]$ are completely different, with $\text{Re}[\xi_{12}]$ narrowly distributed around zero while $\text{Im}[\xi_{12}]$ widely distributed with large variations.

Thus the application of η is only good for high loss cases where $\alpha > 5$ and starts to break down when α get smaller.

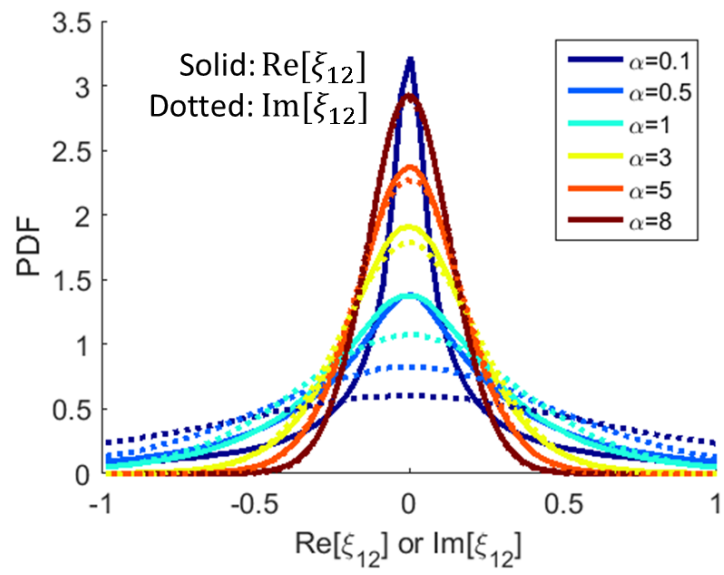


Figure 4.10: The distribution functions of the real (solid line) and the imaginary (dotted line) part of the normalized impedance ξ_{12} calculated from the RCM simulation for various α . The real and the imaginary part distribution functions are identical when $\alpha = 8$ but start to differ when $\alpha = 5$ and lower.

Chapter 5: Multiple Scaled Cavity Experiment

So far, I have discussed the scaled cavity experimental setup in Chapter 2, how to account for the lossy ports with radiation efficiency in Chapter 3 and the experimental results and analysis for a single scaled cavity in Chapter 4. Now I take the exciting step of extending the scaled experiment to multiple interconnected scaled cavities.

Since I only finished the design and construction of the experimental setup before I left the University of Maryland College Park, and the actual work of conducting and analyzing the experiment was continued by Shukai Ma, I'll focus on the design and construction process for most of the chapter. In section 5.3, I present a brief review of Shukai's findings as published in Ref. [9, 69]

5.1 Experimental Design

Evidently, the multiple connected-cavity experimental setup is much more complex than that of the single cavity experiment, mostly because of the additional components. Moreover, there are several considerations that added to the challenge, which we will discuss in detail in section 5.1.1:

- Efficient use of space and material.
- Flexible configuration of various numbers of interconnected cavities.
- Consistent control of cavity mode perturbation for all cavities.
- Antenna and lens alignment.
- Cost efficient construction.

5.1.1 Design considerations

5.1.1.1 Cost efficient construction

This might be an obvious constraint: the project has a clear budget and schedule. This is not to say that we need to sacrifice quality for cheaper or quicker options, but rather to look for alternative construction methods that produce equivalent or similar results and that don't strain our resources. Many design decisions below will highlight such choices.

5.1.1.2 Efficient use of space and material

This is not an issue in the single cavity experiment since the larger copper box ($s = 20$ scaling) occupies only about 6.5 cm X 6.5 cm X 3.5 cm in space positioned inside a spacious BlueFors BF-XLD400 dilution refrigerator with a cylindrical sample space of 50 cm in diameter and 50 cm in height. But with multiple cavities, we need to be aware that the antenna and lens require certain clearance with the cryostat windows to properly focus the mm-waves and that the mounting hardware also takes up considerable space around our cavities. If we are not careful, the number of cavities we can fit in there could be very limited. Or worse, having purchased all the parts and components only to find out that the antenna can't fit in, or the cryostat shielding won't close. Therefore It is crucial to have a complete computer 3D model, as shown in figure [5.1](#), with enough clearance at all sides during the design.

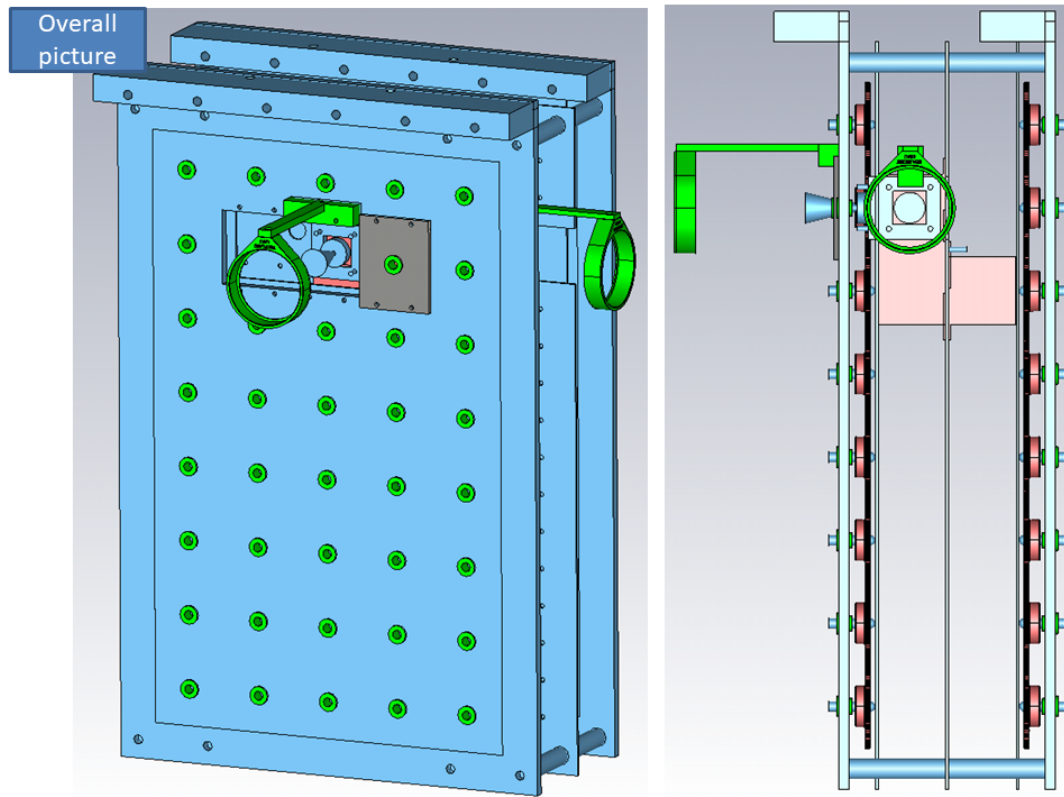


Figure 5.1: The complete computer 3D model for the multiple interconnected scaled cavity experiment setup. The details of each component visible here are discussed below.

Another aspect is the material mass. Cooling down a larger mass of material takes a longer time to reach steady state temperature. In the single scaled cavity experiment, the whole process of cooling down then warming up takes about a week to complete, which might not seem too bad given the large amount of experimental data we are collecting. However, the long turnaround time means that any error, such as a failed stepper motor causing the perturber to not rotate, would toss out the entire previous week's effort. One week is perhaps the sweet spot for taking enough measurements while keeping a reasonable turnaround time. We could deploy thermal straps to connect the cryostat base plate and sample to facilitate better thermal transfer.

To use space and material efficiently, we made these design decisions:

- Use much thinner material for the box walls as compared to the single scaled cavity and construct the 6-sided box with plates and tiny screws, as shown in figure 5.2. We explored the option of using sheet metal to form an enclosure, similar to folding a paper box, but closing the seams at the corner without affecting the copper box properties is too difficult. We avoided hollowing out a solid copper block mainly due to the excessive machining time and material waste. It could end up giving us a rigid copper box but removing that much material takes a long time, and therefore leads to bigger machine shop bills, making it cost prohibitive, especially considering the fact that we probably want to make a dozen or more of such boxes.
- Use rabbet joints at corners to trap electromagnetic waves inside. As a result

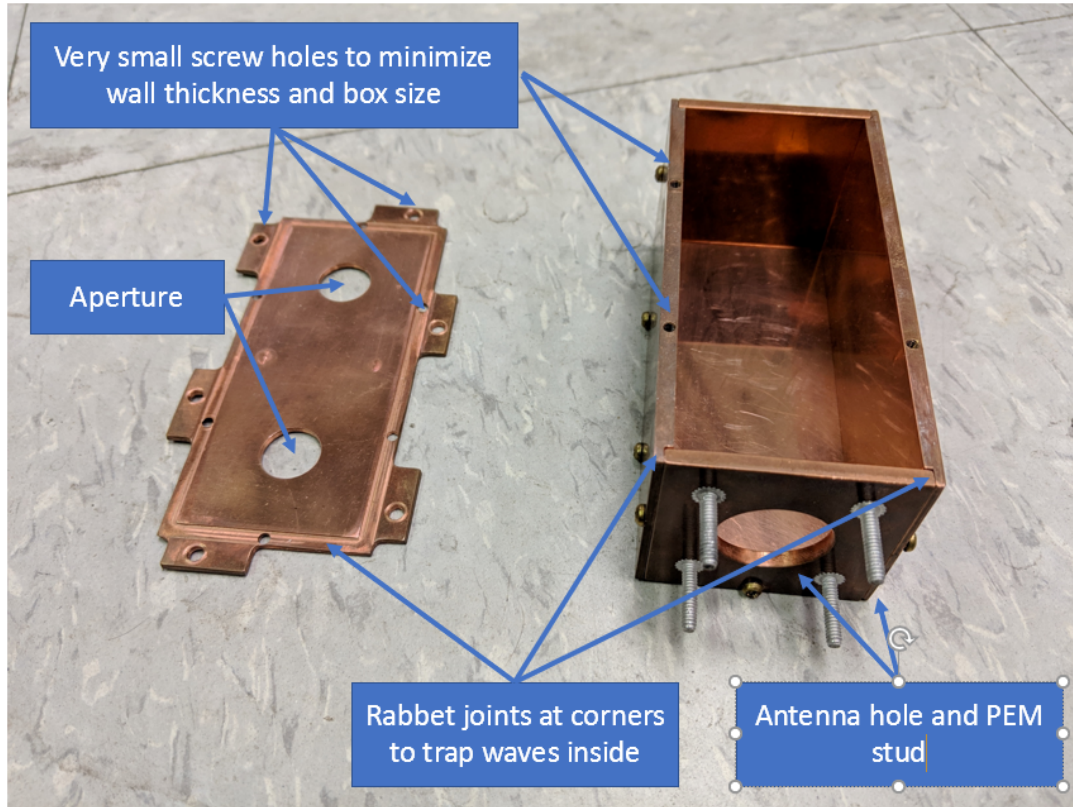


Figure 5.2: Scaled interconnected cavity design with aperture, antenna mounting hole and mounting screws.

of constructing a box from plates and screws instead of a one-piece box, there are seams at the corners that could allow the millimeter waves to leak out if they are simple butt joints. Adding the rabbet, a matching recess at each joining wall, will make it much harder for the mm-wave radiation to escape. This is applied both at the side corners as well as the bottom and top corners, as highlighted in figure 5.2.

- Use PEM studs as antenna mounting screws to maintain a smooth inner wall surface. A PEM stud is a type of fastener that does not require drilling a through hole on the wall to put the screw through. This is very useful for our case since we would like the inside walls to be consistently smooth and

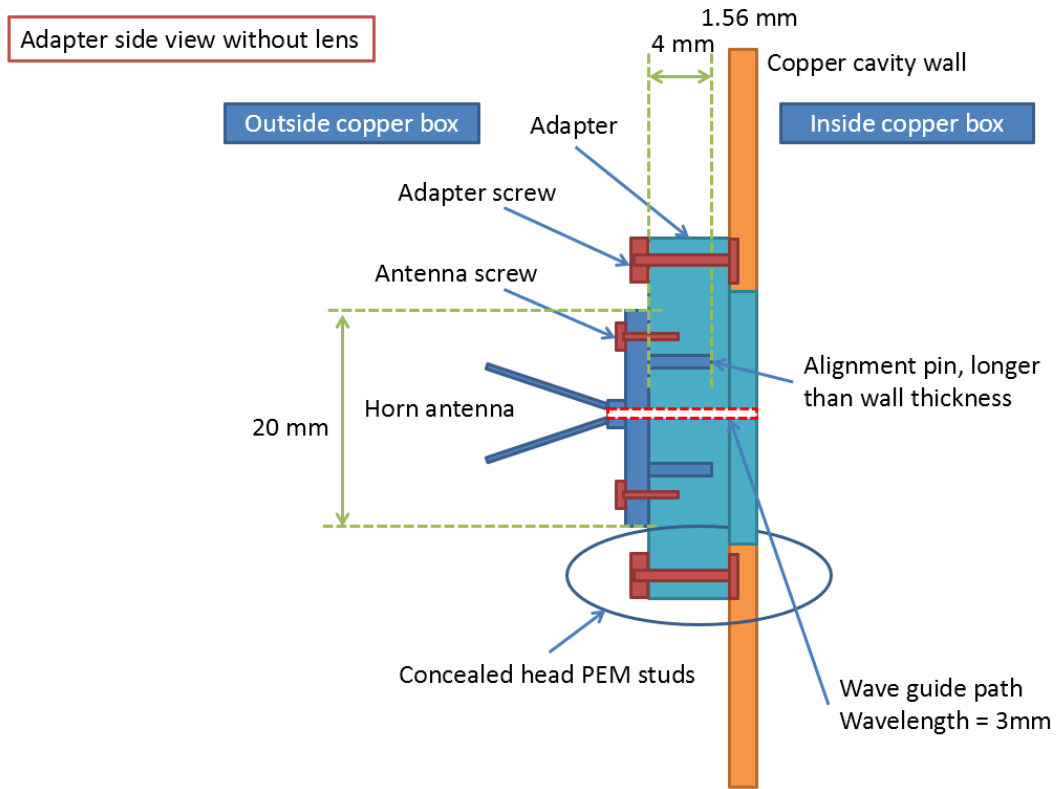


Figure 5.3: Cross section of copper box wall showing the antenna mounting arrangement. The antenna is mounted to the box with an adapter plate. Concealed PEM studs are used to avoid having protruding screws or nuts in the box interior.

featureless for all boxes. Figure 5.3 shows how the antenna is mounted to the box without protruding screws into the interior.

- All scaled cavities are attached to a common center plate, which also represents the aperture plate connecting each cavity. The center plate serves both as the mounting plate for the boxes and also the aperture that allows electromagnetic waves to travel between cavities. The center plate is constructed from a single piece of copper plate by drilling clear holes on it for screws and apertures. It is very straightforward to construct, and we can make multiple copies of the plate with different aperture sizes, providing different coupling between cavities. A

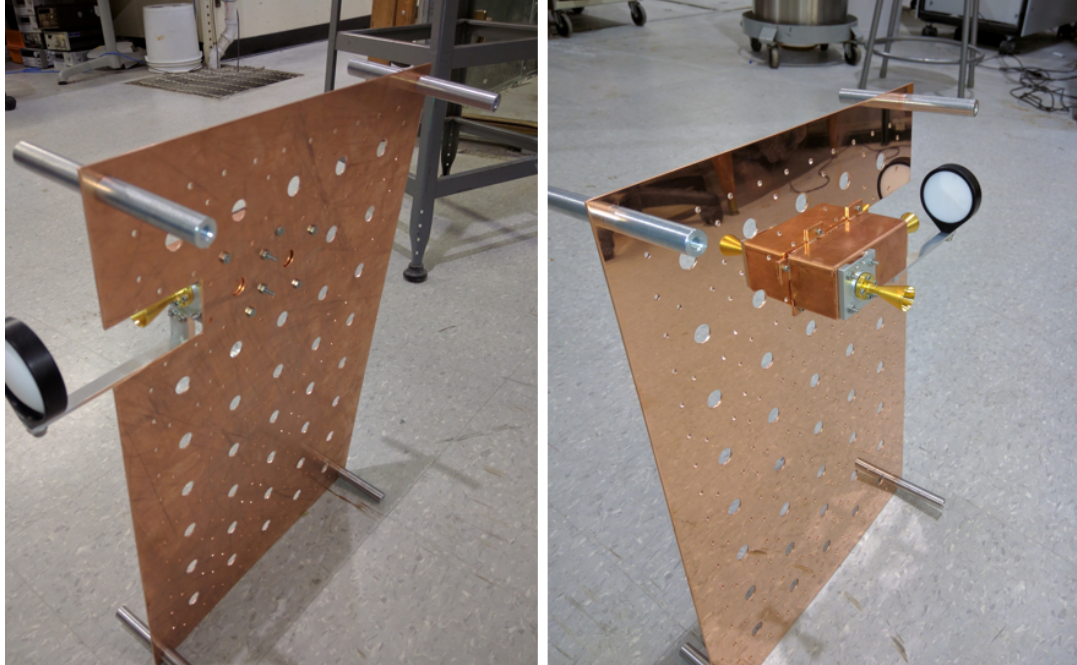


Figure 5.4: One scaled cavity with two antenna installed is mounted on the central plate. Notice that the aperture is covered up since this is a single cavity configuration.

special insert plate is needed for the box at the end of the cavity cascade to cover up unused apertures. Figure 5.4 shows a single cavity configuration where two antennas are mounted onto one cavity and the apertures are covered up.

- An insert plate (shown in figure 5.5 and shown as the left plate in figure 5.2) to connect the 5-sided box and the center plate. It has aperture openings to match the ones on the center plate and two PEM studs to allow boxes to be mounted on the other side of the center plate if needed. See figure 5.6 for how the PEM studs get through the clear screw holes of the box on the opposite side.

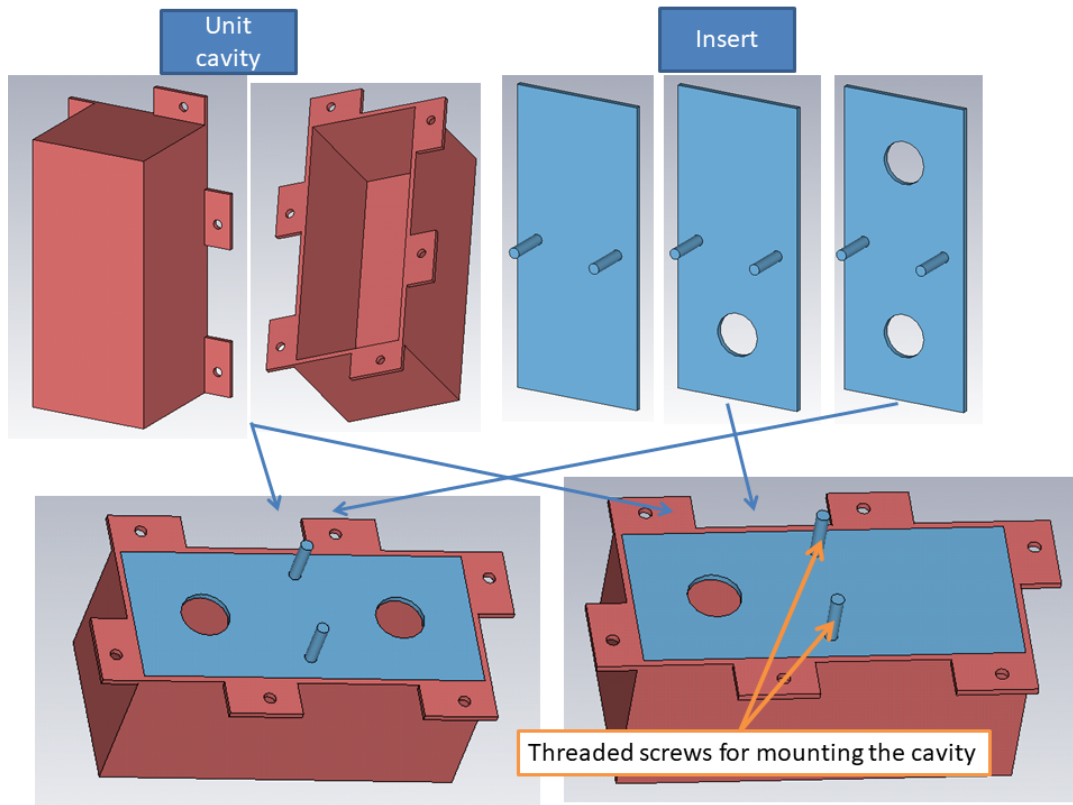


Figure 5.5: The 3D models of one unit box with different insert configurations. Insert plates, shown in the upper right, can have two apertures (allowing the box to be coupled with two other boxes), one aperture (allowing the box to be coupled with another box as the end of a cascading chain of boxes) or no aperture at all (for a single cavity configuration).

5.1.1.3 Flexible configuration

It may be easy to construct a setup of, say, $N = 5$ interconnected cavities, but it would only provide us a single case study as opposed to the targeted theoretical work in figure 2.1 where N varies from 2 to 7. What if we'd like to change the size of the cavities, or the size or shape of the apertures? Having the ability to configure the experimental setup (such as the number of cavities) without changing other parameters (such as aperture size or cavity size) is both crucial to the experiment result analysis and also helpful in preventing the construction cost from exploding with all the combinations.

That is why the design is notably a modular design at its core from the very first draft. As shown in figure 5.6 for a 3-cavity cascade model, all 3 unit boxes are constructed the same way, mounting onto the center plate from opposite sides and in different orientations, connected through the apertures to form a cascade. Each box is identical to the other ones and is symmetric, ensuring close to identical wave properties across all 3 boxes and also allowing two boxes from opposite sides to share screw holes and to be mounted using fewer screws.

The modular design also allows us to:

- Easily add more cavities into the cascade by adding more unit boxes on opposite sides of the center plate. At its maximum capacity, we could have a cascade with more than two dozen unit boxes.
- Increase box size from 1X2 unit to 2X2, 2X3 or even a larger size by simply

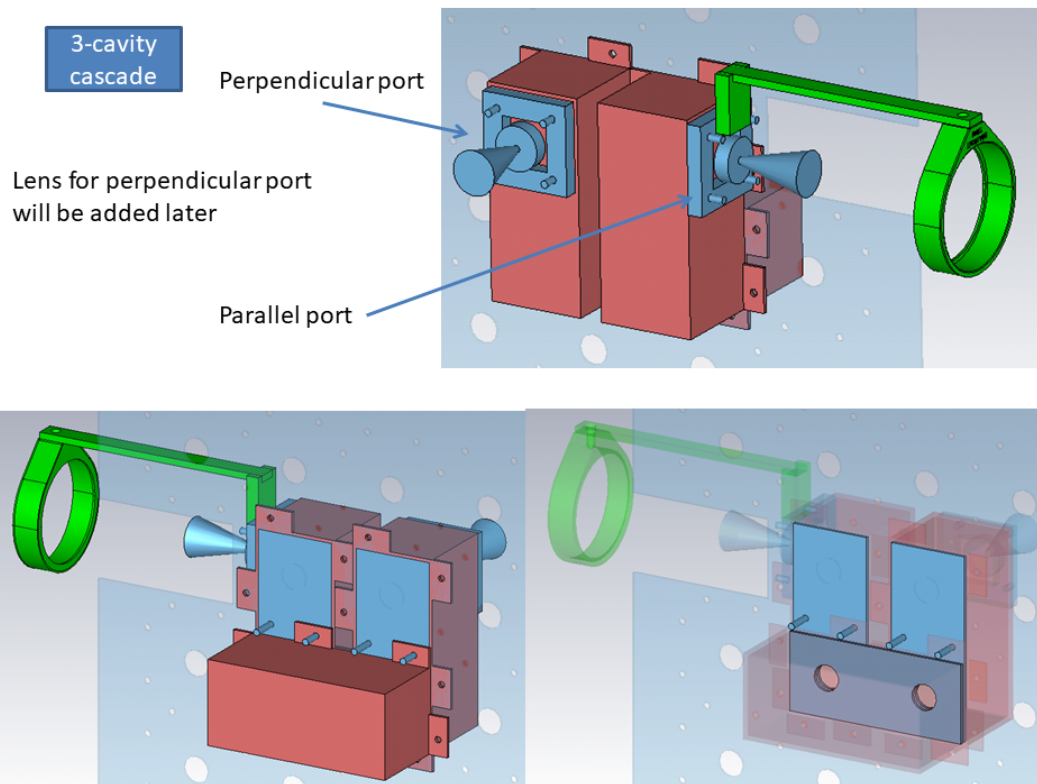


Figure 5.6: 3D model for a 3-cavity cascade setup. 3 unit boxes are mounted to opposite side of the center plate, connected through the apertures to form a cascade. Electromagnetic waves come in from a receiving antenna, passes through all 3 boxes in the cascade and go out through the other antenna.

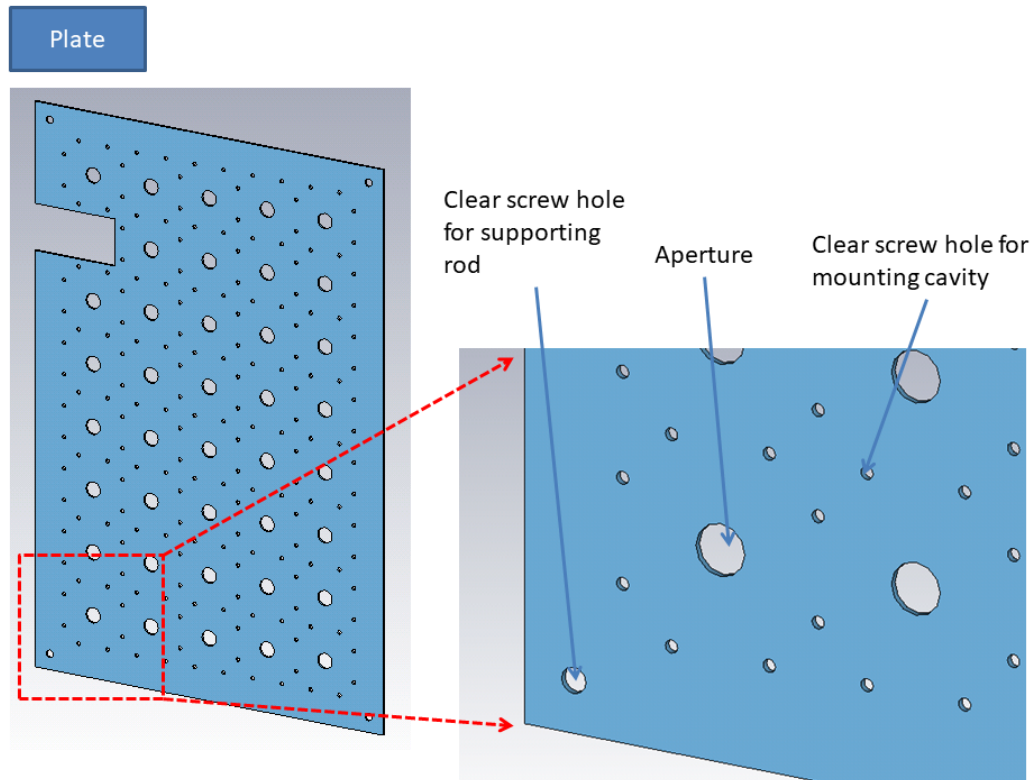


Figure 5.7: Center plate model with apertures and clear screw holes. The notch at the top of the plate is to accommodate the antenna and lens.

swapping out the walls. Notice that the walls are simple copper plates with rabbet at the end and a few screw holes, so they are easy and cheap to make, especially in bulk.

- Change the aperture size by swapping out the center plate for another design, or partially cover the apertures to modify their size and shape. Figure 5.7 shows one center plate design and can be easily modified to have different aperture sizes.

5.1.1.4 Perturbers

The perturbers follow the same principle as in the single scaled cavity experimental setup, i.e. using coupled magnetic stripes inside and outside the cavity to rotate a metal foil stirrer by a motor. However, the challenge here is how to rotate $N > 1$ perturbers when we can only fit in one stepper motor inside the cryostat.

Our solution is to use an array of gears to carry the rotation to all perturbers, as shown in figure 5.8 for the model and figure 5.9 for the real assembly. Each gear has an embedded magnetic strip that is coupled to the stirrer inside the cavity. The gear assembly requires their own support plate to be mounted into the cryostat while keeping at a close distance from the cavities to maximize magnetic coupling. We choose teflon as the gear shaft so that it runs smoothly without needing any lubricant. The gear itself is an off-the-shelf product made of plastic.

5.1.1.5 Antenna and lens alignment

An easy to overlook fact is that the windows on the cryostat shields and outer wall are fixed, which means that the antenna and lens must be installed along the same lines as in the single scaled cavity experimental setup. That's why in the design 3D model in figure 5.10, there are two connector plates at the top of the gear assembly plate to attach the samples to the cryostat base plate while at the same time adjusting the height of the antennas and lens to be aligned with the windows.

Another design is that the width of the connector plates is determined so that we can mount the front-facing antenna at either side of the center plate while

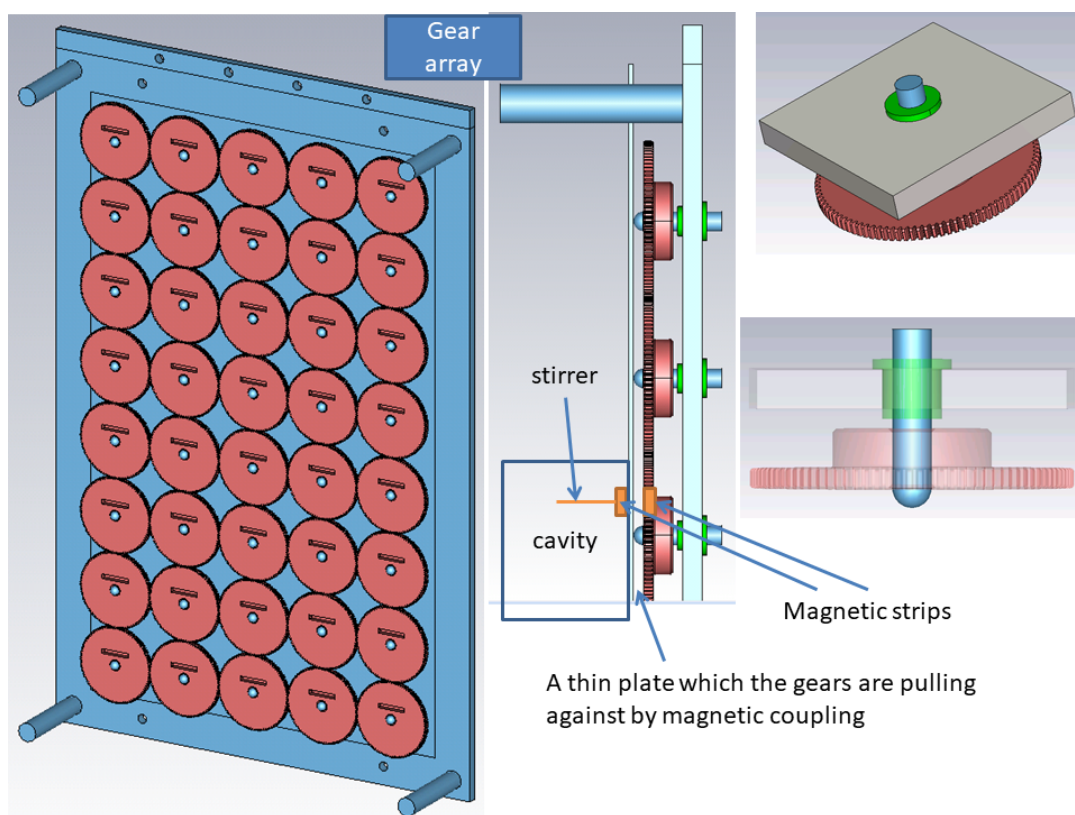


Figure 5.8: Perturber assembly 3D model.

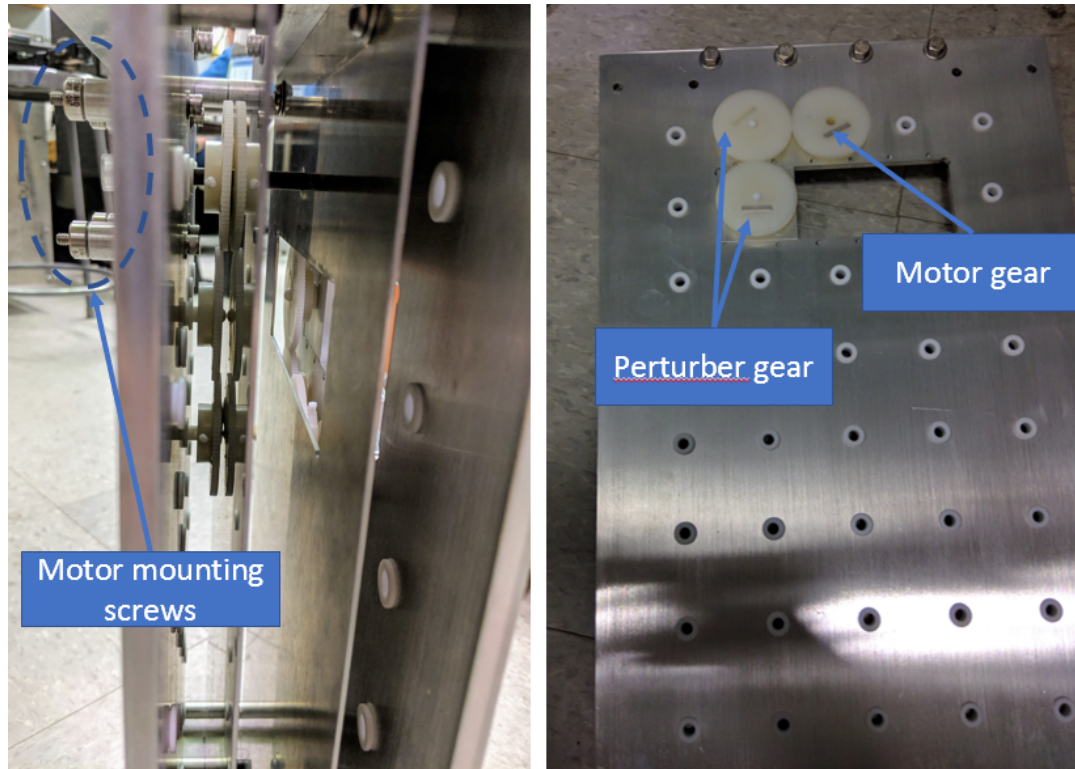


Figure 5.9: Perturber assembly.

keeping the alignment intact. Mount the front-facing antenna at the left side of the center plate (as shown in figure 5.10 upper right) then mount the gear assembly on the connector's right side. Now if we need to switch the front-facing antenna to be mounted on the right side of the center plate, then mount the gear assembly on the left side of the connector. In both cases, the front-facing antenna is always centered.

Notice a few details about antenna and lens:

- The left facing antenna has a clear opening through the gear assembly to fit in, while the front-facing antenna has a notch in the center plate to fit in.
- The two antennas will be on opposite sides of the center plate for the case of an even number cavities, whereas they will be on the same side for the case of

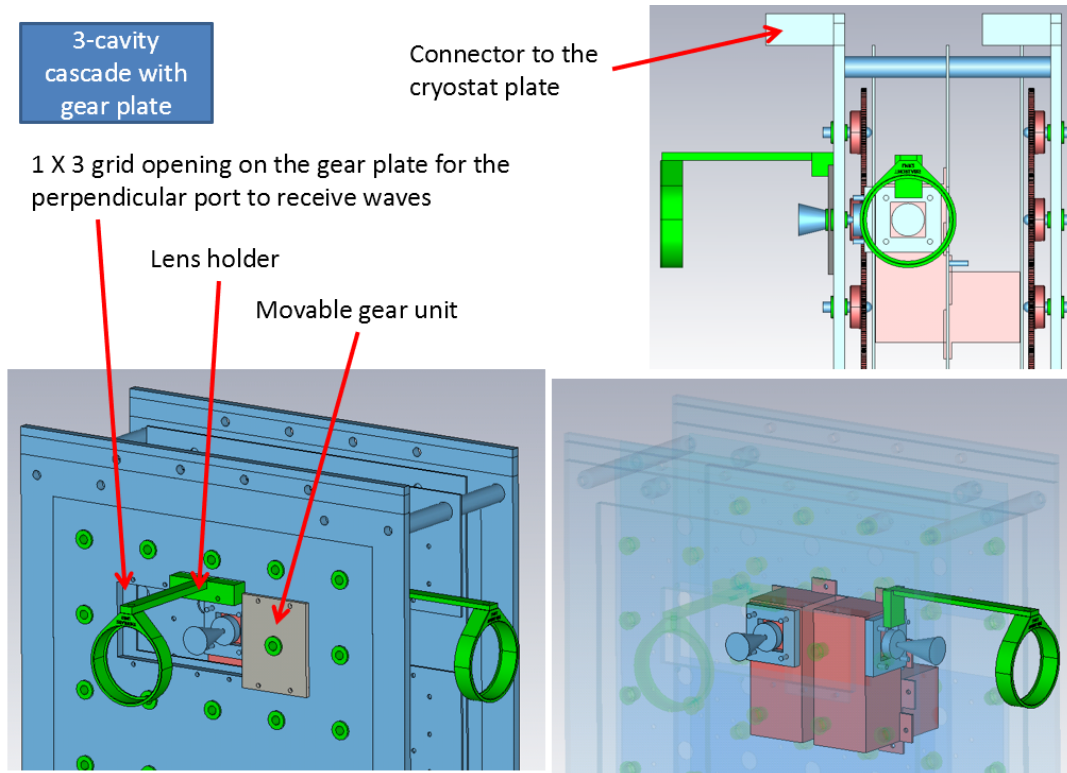


Figure 5.10: Another view of a 3-cavity cascade setup. The 1X3 opening, the lens and antenna are aligned with the cryostat window to ensure maximum transmission of mm-waves. The grid of small green slots are for rotating gears (shown as red gears in upper right figure) to rotate magnetically coupled perturbers inside the cavity. A special plate can be installed within the 1X3 opening to mount gear if needed.

an odd number cavities (as shown in figure 5.10 for 3 cavities).

- The two antennas must always be positioned to align with the second row opening in the gear plate, in order to be aligned with the cryostat windows at the correct height. The dimensions, including the margin of the gear plate, the thickness of the connector plate to the cryostat, are carefully designed to ensure this alignment of the cryostat window, the gear plate opening and the antenna.
- The first row of gears is designed to be connected directly to the stepper motor.
- There is a 1X3 grid opening at the second row of gears, allowing mm-waves to enter through lens and be received by the antenna. To install gears inside the grid opening, which is required in some configurations to ensure we have one rotating perturber inside each cavity, we designed a special movable gear unit that can be mounted onto, or removed from, the grid opening as needed. Notice that we cannot have a perturber right under the antenna inside the cavity.

5.1.2 Assembled setup

To summarize, the assembled cavities have the following components:

- 5-sided rectangular copper unit cavities. (Fig. 5.5)
- Cavity inserts with 0, 1, or 2 apertures. (Fig. 5.5)
- Center plate with clear screw holes and apertures

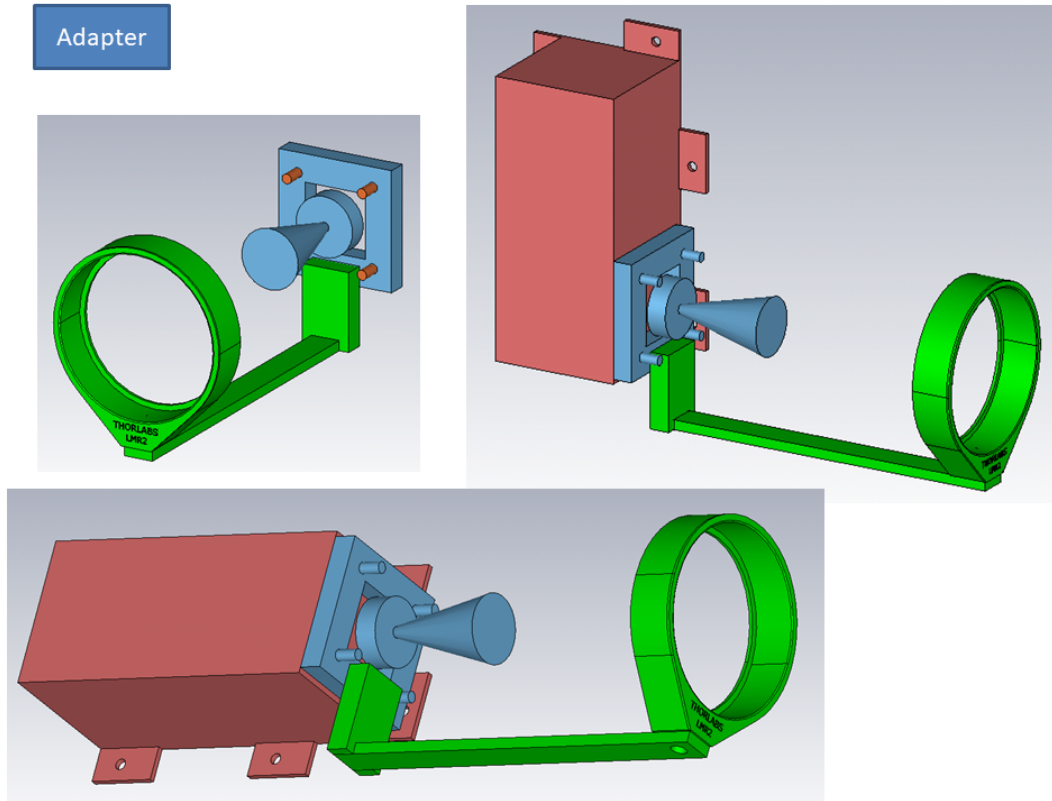


Figure 5.11: Antenna adapter model. An adapter plate (rectangular blue plate) is required to mount the antenna (blue cone) and the lens holder (green) onto the cavity (red box). The antenna and lens can be installed onto the adapter plate first, as shown in the upper left figure. Then the adapter plate is mounted onto the cavity by PEM studs (small red cylinder in upper left figure), which do not require screw holes or any protrusion into the cavity.

- Gear assembly. (Fig. 5.8)
- Antenna adapters (figure 5.11)
- Stepper motor adapter (figure 5.12)

5.2 Lessons Learned

During the design and construction of the experimental setup, there were many lessons learned that might be useful for future projects.

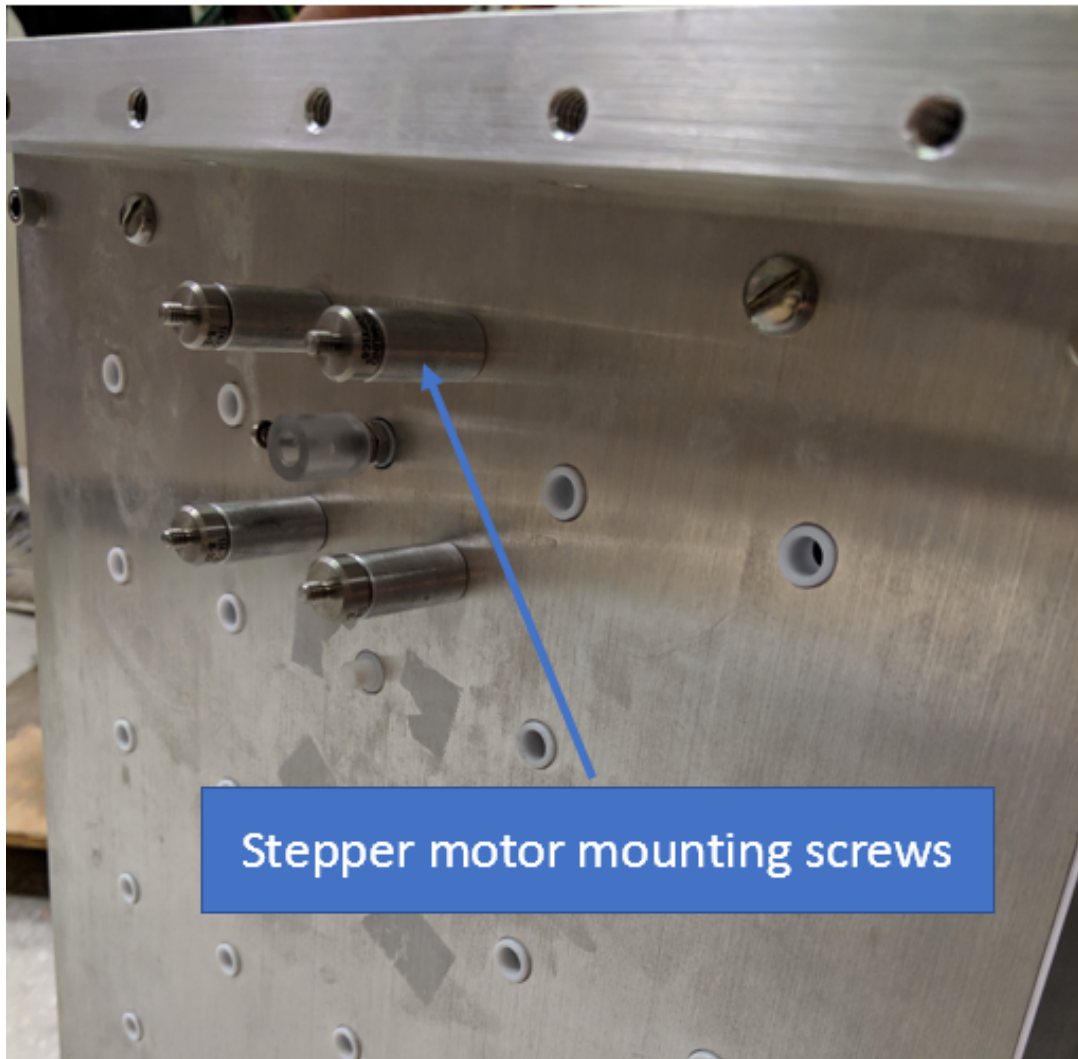


Figure 5.12: Stepper motor mounting location.

5.2.1 Design assistance tools

The multiple interconnected scaled cavity experiment setup has many parts, each with its individual design considerations, and putting them together could be a head-spinning exercise prone to mistakes. We utilized the following tools to avoid many of the mistakes and to help clarify the design decisions to other people.

5.2.1.1 CST modeling tool

The majority of the design is completed in CST using its 3D modeling functionality. There are many other computer aided design (CAD) tools out there, such as Autodesk AutoCAD, Solidworks, Sketchup, etc., but CST is a necessary tool for electromagnetic simulations that we already frequently use in the lab, which can handle the same level of modeling task for this project. For example, in addition to creating basic shapes like block, sphere, cylinder, etc., CST can also:

- Define lengths of objects using variables and equations. For example, we can define the radius of the circular aperture as $R = 1$ cm, then draw out the center plate with all the apertures in it with reference to R . If we wish to change the aperture size, we can simply change the variable to $R = 2$ cm and the design can be refreshed to reflect the updated design. R can even be defined using other variables, like the length of the unit box, for instance. Internally, CST calculates the actual values and redraw the shapes from the beginning of the history. Each step, including drawing or mutating objects (rotate, move, mirror, etc.) can all use variables and equations in place of actual numbers.

This allows us to quickly modify our design (such as changing unit box size) without starting all over again drawing each parts from the beginning, which could be very frustrating (I've been there).

- Group objects to define re-usable components. With so many parts involved, it is necessary to employ the principle of divide and conquer. We can start by drawing out the basic simpler components, such as the unit box (figure 5.5) or center plate (figure 5.7), and save them as custom components. Then we can start composing the bigger assembly using the custom components as building blocks, greatly simplifying the modeling process. Also the unit box can be used in other models in order to simulate the cavity modes in CST simulations, knowing that the simulation geometry is the same as the experimental setup.
- Easy communication through pictures and 3D files. The presentation of the setup, either in meetings, proposals or papers, is equally important as the experimental result itself. A few pictures from the CST 3D model with its distinctive color coding and hide/show/transparent settings can easily convey the idea across to the audience that words cannot match. The models can also be imported or exported with standard 3D model files, which makes it possible to import the product model with intricate parts, such as the antenna lens and perturber gears, or export it so the machine shop experts need less consultation and have better understanding.

5.2.1.2 3D printed models

3D printing is a great way to enable fast prototyping. It is fast, taking less than a day from start to finish as opposed to weeks or months of lead time for metal machining, and convenient, only requiring a 3D model file without the need to have back and forth discussions with the machinist. It is a preview of the setup that allows issues to be uncovered and fixed that would otherwise be difficult to visualize.

Playing around with a few unit boxes together with a center plate with apertures on it, as shown in the left of figure 2.14, can help us realize how the cascade is forming and how the parts are connected, which could reveal issues ahead of time. It is also a good prop for in-person presentations or talks that generates interaction, interest and better communication.

Mounting the 3D-printed model boxes onto the center plate, I noticed that some of the 6 screws on the box side walls will protrude into the box on the other side. To remedy this, we added the insert plate with PEM studs (shown in figure 5.5) so that the box inside stays flush and the box on the opposite side has screws to fasten onto.

5.2.2 Methods to Construct a Metal Box

The cavities, which are rectangular copper boxes, are the center of the show. As discussed in Chapters 2 and 4, and shown in Figure 4.3, the surface material and its smoothness have a big impact on the quality factor of the cavity. Hence to achieve a higher Q , we want to have a copper box with smooth interior walls that can be

polished and cleaned easily.

We used to construct metal boxes by milling out a bulk metal, essentially hollowing out most of the material by peeling it off layer by layer on a milling machine. This takes a long time and wastes a considerable amount of material, but is not a big concern when we only need to construct one such box. The milling process leaves marks on the interior wall that increase surface roughness on a microscopic scale. It is smooth to the touch but at hundreds of GHz frequency range the roughness will reduce the quality factor significantly [58, 59]. So polishing the interior surface is required after milling. However the interior corners of the one-piece metal box are difficult to reach for polishing.

The method we choose to construct the multiple interconnected cavities is to use metal plates fastened together with screws and rabbet joints. Since the plates can be cut directly from commercially available sheet copper with pre-polished surfaces, the walls are smooth without any milling marks. The center plate is also made from sheet copper that has a mirror like factory finish on them (figure 5.13). Some milling is done to make the rabbet joints but those surfaces won't be exposed to electromagnetic waves. Furthermore, the plates can be easily cleaned or polished if necessary when they are disassembled. Removing the dust and grease on the surface regularly contributes to consistent high quality measurements across different experimental runs. The only drawback is the additional effort working with the tiny screws.

Another alternative that we tested and eventually abandoned is folding sheet metal to form a box. Although the sheet metal folding process is supposed to be

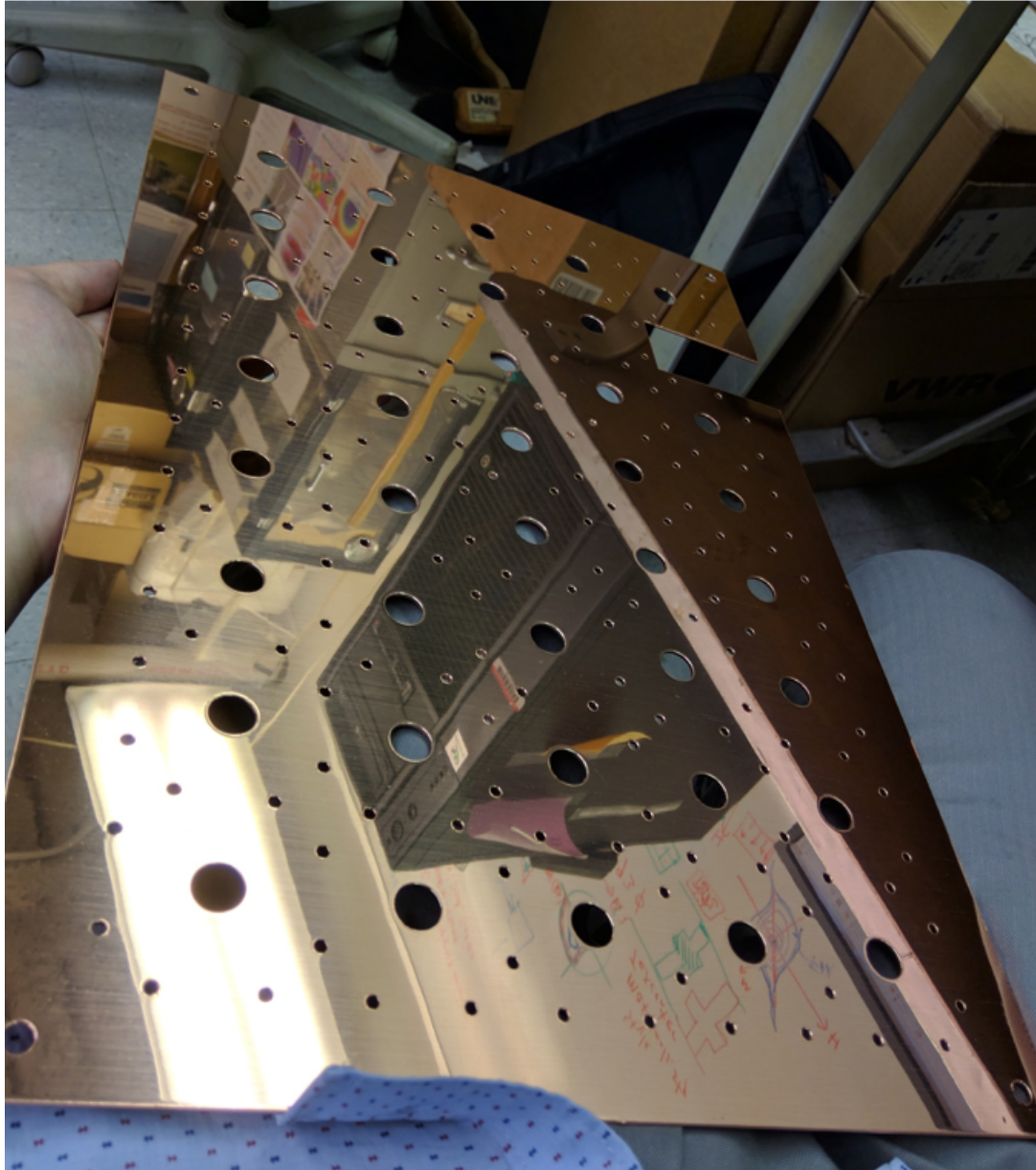


Figure 5.13: Smooth mirror-like finish from sheet copper. The part comes with a protective plastic film that can be peeled away to reveal the metal surface that is free of milling marks.

easier and cheaper than drilling or tapping screw holes, the resulting box either has a visible seam at the corner or has considerable amounts of solder in an attempt to close the seams. In our test, the sheet metal box exhibit higher than expect loss and we cannot find a good fitting radiation efficiency according to the analysis process described in section [3.2.2](#), indicating possible inhomogeneous loss.

5.2.3 External vendors

The University of Maryland College Park has an excellent team of machinists that can provide consultation and quality work with convenience. There is also student machine shop that students can get training and make simple parts. But external vendors are a good compliment to what we have on campus with sometimes better cost or time efficiency.

I started with a google map search to find nearby machine shops or sheet metal workshops. A reliable modern workshop should at least have professional CNC machines and good customer reviews. A lesson from my experience with the local sheet metal company is that one should try to talk to the technicians that will design and make your parts, in addition to the sales representatives or managers. The non-technicians may not fully grasp the implications of your requirements and inflate their capabilities to secure a potential customer, whereas a technician or expert in the field can give realistic opinions on the challenges.

If the parts are self explanatory with a CAD file and don't have stringent requirements, then it is possible to find online vendors that will make and ship the

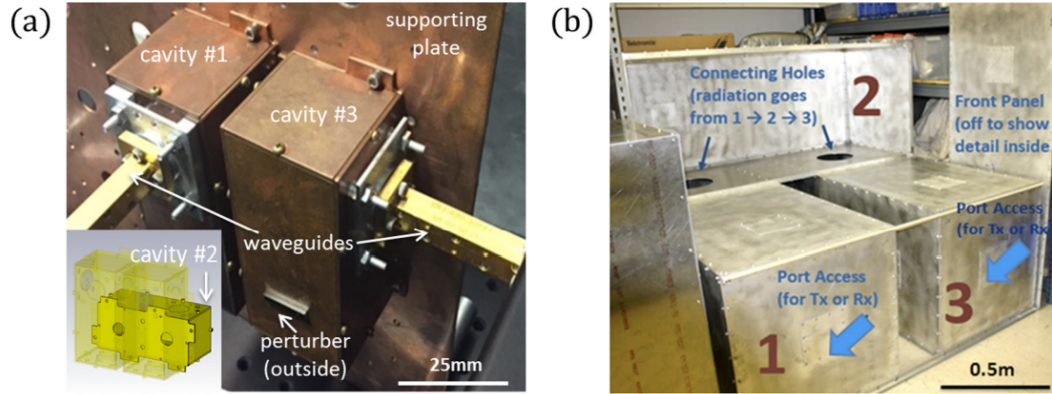


Figure 5.14: A side by side comparison for a 3-cavity cascade setup with the scaled-down cavities on left and full scale cavities on the right. Figure 6 in [9]

parts from other states or even globally, without in-person consultation. Keep in mind that these vendors may not produce quality precision parts, and plan accordingly.

5.3 Experimental Results

The multiple interconnected scaled cavities were put into action by my successor Shukai Ma, and he published two papers describing the work [9, 69]. It is obvious from the comparison in figure 5.14 that the scaled-down cavities are much easier to reconfigure and extend the number of cavities than the full scale version.

As for the experimental results, Shukai analyzed the statistics of the trans-impedance, defined as $Z_t = U_{RX}/I_{TX}$ where U_{RX} is the induced complex voltage at the receiving port and I_{TX} is the complex current at the transmitting port, and the induced voltage on a 50 Ohm load attached to the last cavity. It was shown in Ref. [9] that their statistics are almost identical between the scaled-down and full-scale cavity cascade (figure 3 and 4 in Ref. [9], respectively). As depicted in

Figure 5.15, the experiment results for the induced voltage PDF matches pretty well between scaled (short dotted lines) and full-scale (long dotted lines) cavities with various configurations, from a single cavity to a 3-cavity cascaded. As explained in the paper, the differences come from the difference in aperture thickness compared to the wavelength, as confirmed by CST simulations.

Overall, the experimental results confirm that the scaled cavities are a convenient way to study in a laboratory setting the complex coupled systems that would otherwise be difficult to construct, configure, and extend at full scale. The RCM is proven again to be a useful statistical model to predict the wave properties for single or coupled multiple wave-chaotic cavities.

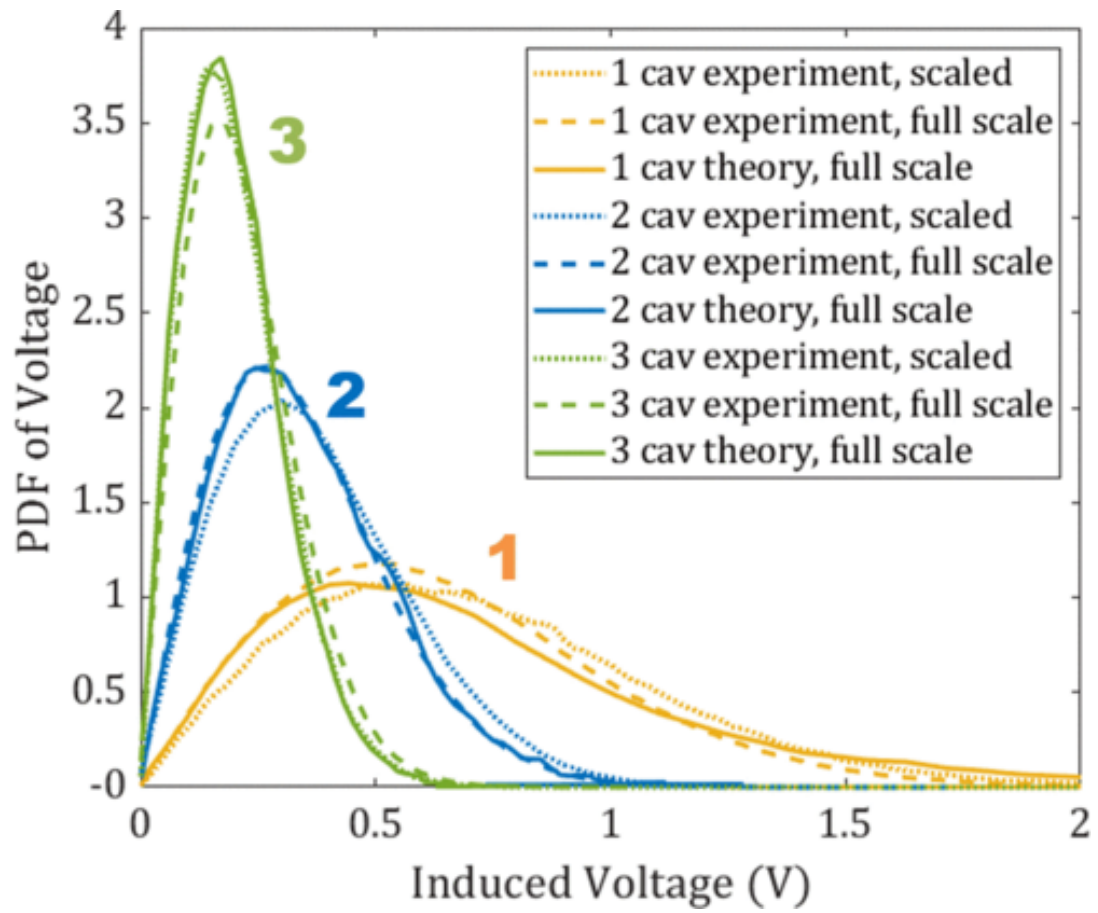


Figure 5.15: Comparison of the PDF of the induced voltage on a 50 Ohm load attached to the last cavity between the scaled cavity cascade and its full-scale counterpart. Figure 4 in [9].

Chapter 6: Focusing Waves at Arbitrary Locations in a Ray-Chaotic
Enclosure Using Time-Reversed Synthetic Sonas

Time reversal methods are widely used to achieve wave focusing in acoustics and electromagnetics. Past time reversal experiments typically require that a transmitter be initially present at the target focusing point, which limits the application of this technique. In this chapter, I propose a method to focus waves at an arbitrary location inside a complex enclosure using a numerically calculated wave excitation signal. I use a semi-classical ray algorithm to calculate the signal that would be received at a transceiver port resulting from the injection of a short pulse at the desired target location. The time-reversed version of this signal is then injected into the transceiver port and an approximate reconstruction of the short pulse is created at the target. The quality of the pulse reconstruction is quantified in three different ways, and the values of these metrics are shown to be predicted by the statistics of the scattering-parameter $|S_{21}|^2$ between the transceiver and target points in the enclosure over the bandwidth of the pulse. I experimentally demonstrate the method using a flat microwave billiard and quantify the reconstruction quality as a function of enclosure loss, port coupling and other considerations.

6.1 Introduction

Wave focusing through a strongly scattering medium is an intriguing research topic in the fields of optics, acoustics and electromagnetics [70–72]. Its potential applications include medical imaging, ultrasound therapy, communications, and nondestructive testing. In optics, wavefront-shaping has been used to spatially focus light both through and inside strongly scattering media [70, 73, 74]. One can also achieve

focusing in the temporal domain using a time-reversal mirror (TRM). The time reversal technique was first developed in acoustics [75–81]. Much work has been done to study the underlying theory and possible applications in target identification, detection and imaging [82–89]. A TRM can work both in open systems with a strongly scattering medium placed between the target and transceiver ports [90,91], or in closed reflecting walled systems (‘billiards’) supporting ballistic propagation of waves in which the wavelength is much smaller than the billiard size [92–95]. In fact, a relatively simple single-channel TRM can be efficiently implemented in ray-chaotic billiard systems [92], and the experiments discussed here are performed in such billiards.

Previous time reversal experiments typically employ two steps [90, 92–94]. First, in the time-forward step, one injects a short pulse at the target port and collects the resulting long-duration transmitted signal (called the “sona”) at the transceiver port. In the time backward step, one time-inverts the previously collected and recorded sona signal and sends it back into the system through the transceiver port, hopefully resulting in a time reversed short pulse at the target port. Since an active source must be present at the target location to create the initial signal, and because the sona is unique to that location, this process must be repeated for any location upon which one desires to focus waves. As shown in previous work [96–98], one can relax this constraint to some extent by placing a passive nonlinear object at the desired target location and using its higher harmonic nonlinear response as a unique “beacon” for later time-reversal. In acoustics, several methods [99, 100] have been developed to shift the location of the reconstruction,

but these are either limited to small shifts (10% range shift of the focal spot) or to the special geometric case of acoustic waveguides. In both of these cases one must still have a source located at a representative target location to produce a baseline sona signal.

One concern about the time-reversal process is the reliability of a time-reversed sona signal to create a reconstruction as the scattering environment evolves and changes over time. For example the reconstruction quality of electromagnetic waves in a three-dimensional billiard was shown to be quite sensitive to the dielectric constant of the gas filling the enclosure [101]. In fact, this extreme sensitivity of the reconstruction to details in the scattering environment has been exploited as a new sensor technology [102, 103]. In this chapter I wish to create robust reconstructions at arbitrary locations that are less sensitive to details. This is one of the motivations to rely on the presence of stable geometrical properties of the billiard that give rise to robust “short orbits” that connect the wave-entry and wave-focusing points [95, 102].

Here I present a *synthetic sona* method for focusing electromagnetic waves at an arbitrary location in a ray-chaotic billiard using an extension of the time reversal technique. I choose a ray-chaotic system because its ergodicity ensures that all rays launched into the system will visit all points on the billiard boundary. It is also the most challenging situation for our wave focusing technique because small errors in the initial ray trajectory will accumulate exponentially in time. Our method is successful, but has limitations due to wave propagation loss, port coupling mismatch, finite mode density of the billiard, and the existence of chaos in the ray limit. I discuss the effects of these factors by presenting experimental results on

both high-loss and low-loss billiards, different antennas and frequency ranges (to modify coupling), and modifications of the cavity that vary the boundaries and modal structure. In general, I find that the synthetic sona method can produce good time-reversal focusing at an arbitrary location in lossy ray-chaotic billiard experiments with well-coupled antennas.

The synthetic sona method requires numerically calculating the sona collected at a receiving port that is generated by a source at the target port. Here I utilize semiclassical methods to do this. Compared with other numerical methods, such as finite-difference time-domain (FDTD) computation of billiard scattering properties, the semiclassical method is more efficient when the wavelength is much smaller than the system size. When going to smaller wavelengths, most numerical methods require a finer grid which significantly increases the computational cost. In contrast, the semiclassical method has the same computation complexity in all frequency ranges.

In the following, I first describe my experimental setup and procedures, including the calculation of a synthetic sona signal, performing a time-reversal experiment in the time domain and also in the frequency domain. Then I introduce several metrics to measure the reconstruction quality, and I discuss factors that limit the reconstruction quality, such as loss and mismatched port coupling.

6.2 Experiment

6.2.1 Calculation of Synthetic Sona

The construction of the synthetic sona starts with a calculation of ray orbits [95] in the billiard. Specifically, limiting consideration to ray paths below a specified length limit, a ray tracing code is used to obtain the trajectories of rays that start from the target point, bounce off of the walls, propagate ballistically between bounces, and arrive at the transceiver port. Each bounce on the billiard wall follows the law of specular reflection, and I do not consider scattering from the ports. Then, for each trajectory i , the orbit length L_i , number of bounces n_i , and ray bundle divergence factor D_i [95, 104, 105], are used to calculate a scaled and time-delayed version of the input signal, $g(t)$, which is usually a short (on the order of the typical ballistic propagation time between bounces in the billiard) Gaussian pulse. Summing up contributions from all N trajectories of length less than the upper limit gives the synthetic sona signal $s_{\text{syn}}(t)$. In practice the calculation is performed in the frequency domain first, $S(\omega) = \sum_{i=1}^N G(\omega)e^{-j\omega L_i/c}(-1)^{n_i}\sqrt{D_i}$, where $S(\omega)$ and $G(\omega)$ are the Fourier transforms of $s_{\text{syn}}(t)$ and $g(t)$ respectively. Then an inverse Fourier transform of $S(\omega)$ into the time domain gives $s_{\text{syn}}(t)$. Figure 6.1 shows an example of a calculated synthetic sona from four simple orbits linking the target port and transceiver port in a 2D billiard. The above calculation does not include propagation loss. If we assume that the loss is uniform and results in an amplitude decay of $e^{-t/\tau}$ with amplitude decay time τ , and also assume that τ is approximately frequency-

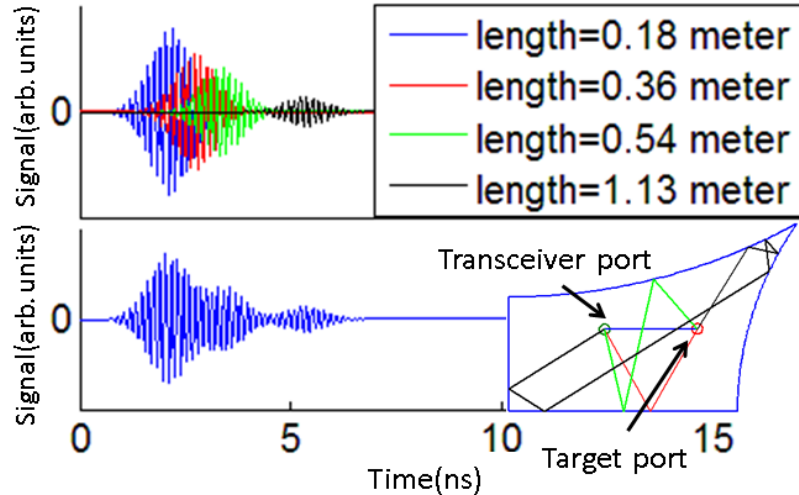


Figure 6.1: Calculation of a brief synthetic sona from four simple orbits in a representative 2D 1/4-bow-tie billiard. We first calculate a scaled and time-delayed version of the input signal, which is a Gaussian pulse modulation of a 7 GHz carrier signal in this example. These waveforms are summed to obtain the synthetic sona shown at the bottom. The two ports are 17.5 cm apart.

independent, then we can apply an exponential window function to the synthetic sona to simulate the effect of propagation loss [106].

6.2.2 Experimental Setup

For our microwave time reversal experiments [94, 107], the billiard is a quasi-2D, ray-chaotic cavity. That is, it is thin in one dimension (z) so that, at the frequencies of interest, the modes of the cavity have electric fields $\mathbf{E} = E_z(x, y)\hat{z}$ [108]. One of the cavity shapes that we employ is depicted in the lower right inset of Figure 6.2 and is referred to as a symmetry-reduced ‘bowtie’ shape [109–111]. We also utilize a superconducting Pb-coated cut-circle shape [112–117] at 7.01 K to create a billiard with minimal loss.

For comparison, we also employ a method based on the technique used in pre-

viously published time-reversal experiments. We generate a short Gaussian modulation pulse of a given carrier frequency, $g(t)$, inject it into the billiard through the target port, and a signal $s(t)$, called the *sona* signal, is measured at the transceiver port (see Fig.6.1 inset and Fig.6.2(a)). This sona signal is recorded and then time reversed. The time reversed waveform is then regenerated as a signal which is sent back into the billiard through the transceiver port. The signal $r(t)$ is then measured at the target port and, as desired, is found to approximately reconstruct the original Gaussian short pulse. The antennas used for the broadcast and receiving port have two-dimensionally isotropic radiation patterns, and are short metal pins extending from the center conductor of the end of coaxial transmission lines at port holes in the upper plate of the two-dimensional cavity [111]. The antenna has a 3dB bandwidth from 6.7 GHz to 11.9 GHz. Due to the variation in eigenmode amplitude at the transceiver and target points [116,117] and propagation loss, $r(t)$ not only contains a time reversed Gaussian pulse replica, but also has temporal sidelobes (see Figure 6.2(b)) which are symmetric about the reconstruction, to good approximation.

The envelope of $g(t)$ is a Gaussian of width $\sigma_t \approx 0.5$ ns modulating a carrier of frequency 7 GHz, which, due to the modulation, corresponds to a spectral width $\sigma_f = 1/(2\pi\sigma_t) \approx 0.32$ GHz in the frequency domain. The areas of the cavities used in the experiment are $A = 0.115\text{m}^2$ and 0.04m^2 for the bowtie and cut-circle cavity, respectively. The corresponding typical ballistic flight times are about 1.3 ns and 0.7 ns. The Gaussian pulse was truncated to a total duration of about $6\sigma_t = 3$ ns. To accumulate many runs of this basic process, we periodically broadcast $g(t)$ with a period $T = 500$ ns $\gg \sigma_t$. The background noise level is about 2mV, and we set

the input power to its maximum such that the sona signal $s(t)$ has a typical peak voltage of 150mV, much higher than the noise floor. $s(t)$ decays to the noise level within about 100 ns for the case of the bowtie cavity, because of ohmic loss in the upper and lower cavity plates and leakage through the ports.

We carry out the synthetic sona calculation procedure for all orbits with orbit length less than $10\sqrt{A}$, where A is the billiard area, a total of 1.2×10^5 orbits for the bowtie billiard. We inject the time reversed synthetic sona (Fig.6.2(c)) into the microwave billiard to obtain the result at the target port shown in Fig.6.2(d). Figure 6.2 (a) and (b) are the sona and the time-reversed reconstruction in the measured time-reversal scheme. The reconstruction signal shows a peak, which is the reconstructed Gaussian pulse, and symmetric sidelobes around the peak. Figure 6.2 (c) and (d) are the calculated synthetic sona (corresponding to orbits up to four meters long, or 15 ns) and its reconstruction at the target port in the microwave billiard. There is a significant peak in the reconstruction, but the sidelobes are now unbalanced. Nevertheless, this result demonstrates focusing at the target port in the experimental microwave billiard using a purely synthetic sona.

6.2.3 Frequency Domain Experiment

The time domain experiment setup described above takes at least 30 seconds to complete one time-reversal process with completely automated instrument control, and this imposes a constraint when we wish to systematically vary the carrier frequency of the input pulse. A sweep of carrier frequency from 1 GHz to 20 GHz takes

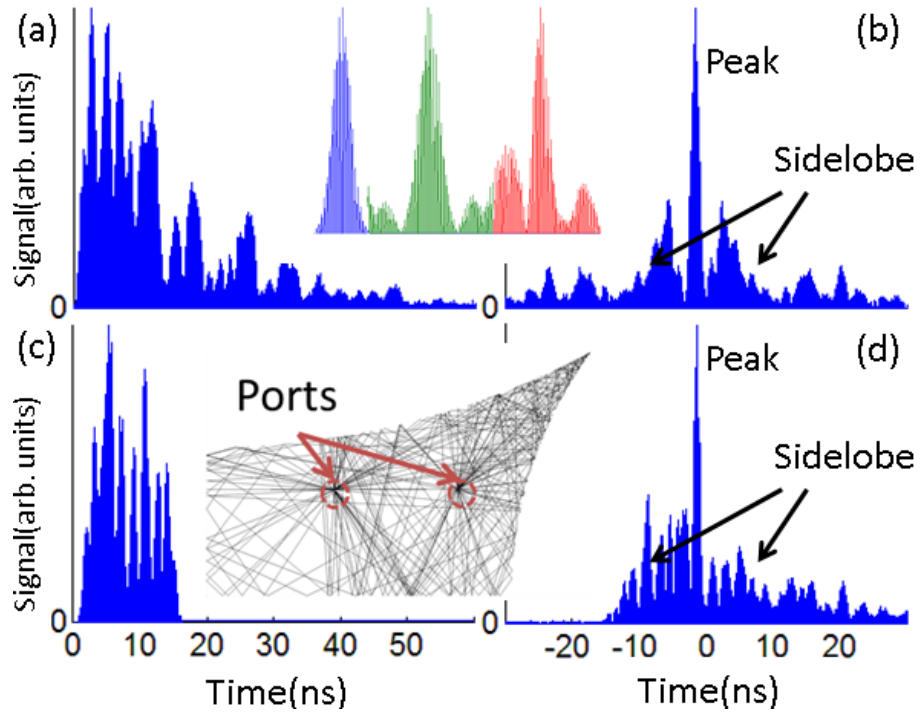


Figure 6.2: (a) Physically measured sona, and (c) synthetic sona signal calculated from orbits less than $4\text{ m} (= 10\sqrt{A})$ in length, and their time reversal reconstruction signals, (b) and (d), respectively. Only the upper half of the signals are plotted since they are essentially symmetric about the time-axis. The upper inset shows closeups of the initial Gaussian pulse (left, blue), the measured sona reconstruction (middle, green) and the synthetic sona reconstruction (right, red). The bottom inset plots some of the orbits used to calculate the synthetic sona. The horizontal and vertical straight walls of the billiard have lengths of 43.18 cm and 21.59 cm , and the two ports are 17.5 cm apart.

hours, during which the cavity state may change due to temperature fluctuations or other time-dependant perturbations [101–103, 118]. This problem can be addressed by switching to frequency domain measurements where the scattering parameter (S-matrix) of the system is measured only once and is then used to calculate the time-domain responses. The systems are linear and reciprocal, thus $S_{21}(\omega) = S_{12}(\omega)$ and $S(\omega) = G(\omega)S_{21}(\omega)$, $R(\omega) = S_{TR}(\omega)S_{21}(\omega)$ where $S(\omega)$, $G(\omega)$, $R(\omega)$ and $S_{TR}(\omega)$ are the frequency spectrum of $s(t)$, $g(t)$, $r(t)$ and $s(-t)$, respectively. The time domain sona and reconstruction signal can be obtained by calculating the inverse Fourier transform of $S(\omega)$ and $R(\omega)$. The output signal obtained in this way is the same as the one measured in the time domain experiment, albeit with much less noise. The signal-to-noise ratio of a $S_{21}(\omega)$ measurement is more than 30 dB while the time domain measurement (which measures $s(t)$ and $r(t)$ directly) has a constant background noise of about 2mV when the maximum peak voltage for $s(t)$ is 150mV. Later we will use this frequency domain version to explore the dependence of synthetic sona reconstructions on the center frequency of the Gaussian $g(t)$.

6.3 Analysis

6.3.1 Reconstruction Quality

It has been shown by Derode, Tourin and Fink [81, 93] that the reconstruction peak-to-noise ratio in a one-channel time reversal experiment scales as $\sqrt{\Delta f/\delta f}$ where Δf is the effective bandwidth and δf is the correlation frequency of the reverberated field. In our bowtie cavity experiment, for example, the bandwidth

is about $2\sqrt{2\ln 2}\sigma_f = 0.75$ GHz and the correlation frequency is governed by the Heisenberg time (the inverse of the mean spacing between eigenmodes), which is about 14.5 ns at 7 GHz. Hence the peak-to-noise ratio should be $\sqrt{0.75 \times 14.5} = 3.3$, and the value observed in experiment is 2.78 in Fig 6.2(b), comparable with expectations.

Reference [117] demonstrates that the reconstruction peak-to-noise ratio scales linearly with ΔT , the length of sona used for time-reversal, when ΔT is small, and it saturates for larger ΔT . In our case the loss is significant. The sona signal decays to noise level in about 100 ns while the recording time is 500 ns, thus we are already in the saturation region. Recording for a longer time only adds more background noise.

Here we discuss other factors that also influence the quality of a synthetic sona time-reversal reconstruction, for example, the propagation loss and port coupling mismatch. In order to examine the effect of these factors and compare reconstructions under different conditions, we first quantify the reconstruction quality using the following three metrics:

- The *peak-to-peak voltage* V_{pp} of the reconstructed Gaussian pulse.
- The *focus ratio* is the average power of the reconstructed short Gaussian pulse divided by the average power of the entire reconstructed signal. The focus ratio measures how the reconstructed pulse stands out from the sidelobes and noise. For the case of perfect reconstruction, i.e., no sidelobes and noise, this quantity is equal to $(E/6\sigma_t)/(E/T) = T/6\sigma_t$ in the experiment described

above, where E is the energy of the signal.

- The *transfer ratio* is the energy in the entire waveform that is received at the target port divided by the energy in the injected time-reversed sona signal. This metric quantifies how efficiently energy is being transferred from the transceiver port to the target port.

6.3.2 Effects of Loss and Mismatched Port Coupling

Here we discuss two main factors that affect reconstruction quality: propagation loss and port coupling mismatch. Intuitively, a system with higher loss should lose more information during the transmission between the two ports, hence the reconstruction should be of lower quality. However, we have also observed that the time-reversal reconstruction in the superconducting cavity can be worse than that in a similar cavity in the normal state, mainly because of antenna coupling issues. Hence propagation loss and port coupling mismatch both affect reconstruction quality, and we now discuss them.

6.3.2.1 Effect of Loss on Reconstruction

We find that to a good approximation the sona signal envelope decays exponentially in time as $e^{-t/\tau}$, where τ is the (assumed frequency-independent) sona amplitude decay time. In particular, for the normal and superconducting cases $S_{\text{normal}}(t) \approx \mathcal{S}_{\text{normal}}(t)e^{-t/\tau_{\text{normal}}}$ and $S_{\text{sc}}(t) \approx \mathcal{S}_{\text{sc}}(t)e^{-t/\tau_{\text{sc}}}$, where $S(t)$ is the exponentially decaying sona signal and $\mathcal{S}(t)$ is the sona signal with an infinite decay time. Furthermore

$\mathcal{S}_{\text{sc}}(t)$ and $\mathcal{S}_{\text{normal}}(t)$ are experimentally found to be approximately the same, with a cross-correlation coefficient of 0.92. Based on these results, in the case of the measured sona method, higher loss will result in a scaled down sona signal with faster decay rate, and, as we will next show, a scaled down reconstruction signal with smaller sidelobes; the reconstruction will thus have a smaller V_{pp} and transfer ratio, but a higher focus ratio.

Let $h(t) = h'(t)e^{-t/\tau}$ be the impulse response between the transceiver port and target port of the enclosure. In the case considered here the cavity is air-filled and waves travel nondispersively with velocity approximately $c = 1/\sqrt{\mu_0\epsilon_0}$; thus $h'(t) = \sum_j A_j \delta(t - t_j)$, $t \in (0, \infty)$, where A_j and $t_j > 0$ are the amplitude and the travel time along ray orbit j connecting the transceiver port and the target port (with the convention $t_{j+1} > t_j$). The sona signal is $s(t) = g(t) * h(t)$, where “*” denotes convolution, and the reconstruction signal is $r(t) = s(-t) * h(t) = g(-t) * h(-t) * h(t)$, where $g(t)$ is the initial input signal. Thus,

$$r(t) = \int g(-t') f(t - t') dt',$$

where $f(t) = h(-t) * h(t) = \sum_{j,j'} A_j A_{j'} e^{-(t_j+t_{j'})/\tau} \delta(t + t_j - t_{j'})$ is an array of Delta functions symmetric around $t = 0$, which explains the balanced sidelobes around the peak in Fig.6.2(b). Thus

$$r(t) = \sum_{j,j'} A_j A_{j'} g(t_{j'} - t_j - t) e^{-(t_j+t_{j'})/\tau},$$

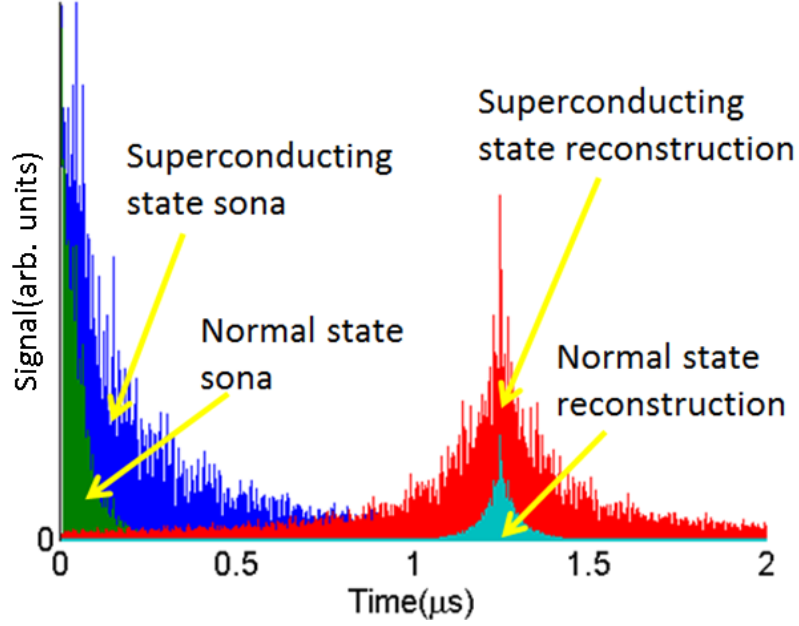


Figure 6.3: Measured signals in cut-circle cavity in the measured sona time-reversal process. The sona signal in the cavity normal (green, shorter in time) and superconducting (blue, longer in time) states, and time-reversal reconstruction in the cavity normal (cyan, lower amplitude) and superconducting (red, higher amplitude) states. The sonas are generated by injection of a Gaussian pulse with $6\sigma_t = 3\text{ns}$, modulating a 7 GHz carrier signal. Data is taken at 6.4 K (superconducting state) and room temperature (normal state).

and lower loss (larger τ) leads to stronger reconstruction with larger V_{pp} , as expected.

Also a larger τ leads to slower decay on both sides of the peak, making the focus ratio smaller.

To better demonstrate the effect of loss on sonas and reconstructions, we compare the sona and the reconstruction measured in the cut-circle cavity in the normal and superconducting states, as shown in Fig.6.3. It is clear that the superconducting state sona, with $\tau_{sc} = 153\text{ ns}$, has a much longer duration than the normal state sona, with $\tau_{normal} = 50\text{ ns}$. The superconducting state reconstruction has a higher V_{pp} but the focus ratio drops from 305 in the normal state to 158 in the superconducting state.

For synthetic sona reconstruction, we replace the measured $h(t)$ from the time forward step with $h^{(s)}(t) = \sum_j A_j^{(s)} \delta(t - t_j^{(s)})$, where $t_j^{(s)}$ and $A_j^{(s)}$ are the calculated time delay and amplitude for the j^{th} short orbit, respectively. Then, similar to $f(t) = h(-t) * h(t)$, we have $f^{(s)}(t) = h^{(s)}(-t) * h(t) = \sum_{j,j'} A_j^{(s)} A_{j'} e^{-(t_j^{(s)} + t_{j'})/\tau} \delta(t + t_j^{(s)} - t_{j'})$. Since the synthetic sona has a finite duration of T_s , $t_j^{(s)}$ must be in the range of $(0, T_s)$. So the prior-in-time sidelobe ($t < 0$) can only extend to $t = -T_s$. Hence, the sidelobes in the synthetic sona reconstruction are unbalanced, consistent with the result shown in Fig.6.2 (d). If the synthetic sona duration is much shorter than the decay time $T_s \ll \tau$ then the left sidelobe, with length of T_s , will appear to be much shorter than the right sidelobe, which has decay time τ , and thus leads to very poor reconstruction. Unbalanced sidelobes may also be seen in other situations, for example in one-bit time reversal [119] where only the sign of the sona signal is recorded.

To summarize, higher loss (smaller τ) results in a scaled down reconstruction signal with smaller sidelobes; the reconstruction will have a smaller V_{pp} and transfer ratio, but a higher focus ratio. The synthetic sona reconstruction has unbalanced temporal sidelobes due to finite synthetic sona duration.

6.3.2.2 Mismatched Port Coupling

Port coupling can be varied by using a different antenna or using different carrier frequencies for a given antenna. The former modifies the radiation impedance of the port entirely, and the latter uses the fact that radiation impedance is a function of

frequency [111, 120]. Both effects lead to a different billiard transfer function $S_{21}(\omega)$, which is the ratio of the complex transmitted wave amplitude to the incident wave amplitude between the transceiver port (1) and the target port (2). Define the mean transmission $\mu \equiv \langle |S_{21}|^2 \rangle_{\text{avg}}$ averaged over a $6\sigma_f = 2$ GHz frequency range surrounding the center frequency of the Gaussian pulse, and $\sigma_n \equiv \sigma(|S_{21}|^2)/\mu$ where $\sigma(|S_{21}|^2)$ is the standard deviation of $|S_{21}|^2$ in the same frequency range as μ . μ and σ_n measure the amplitude and fluctuations of the transmission spectrum $|S_{21}|^2$, respectively. We expect μ to have a linear relationship with V_{pp} because $V_{pp} = r(0)$, $r(t) = g(-t) * h(-t) * h(t) = \int G(-\omega)e^{-i\omega t}|S_{21}|^2 d\omega$, thus setting $t = 0$ leads to $V_{pp} \approx c\mu$ where c is a voltage scaling factor.

Figures 6.4(a) and (b) plot μ and σ_n as a function of pulse center frequency, together with the normalized V_{pp} , and the focus ratio for a series of measured reconstructions performed at the corresponding center frequencies. Figure 6.4 (a) is for the measured sona, and Fig.6.4 (b) for the synthetic sona reconstructions. We find that μ and σ_n predict the trend of V_{pp} and focus ratio, respectively, in the physically measured sona method. The mean transmission μ has a peak around 7 GHz because the antenna is most efficient in that frequency range. For the synthetic sonas μ has a high correlation with V_{pp} , although V_{pp} has stronger fluctuations compared to the case of a physically measured sona.

Since this sweep over center frequency is done in the frequency domain as discussed in section 6.2.3, the calculated $s(t), r(t)$ is almost noise-free. To see the influence of noise on the reconstruction quality, we add Gaussian random noise with 2 mV standard deviation, the typical background noise in our time-domain

experiment, to the synthetic sonas and the reconstruction signals calculated using the measured $S_{21}(\omega)$. Fig.6.4 (c) and (d) show that when noise is added, V_{pp} and focus ratio follow μ in both the measured sona and synthetic sona cases. This is because the average power in the reconstruction signal is mostly determined by the noise power, which is set to a constant, and the focus ratio is now proportional to average power in the reconstructed Gaussian pulse, which is proportional to V_{pp} . Hence μ becomes the only controlling factor in this case.

In summary, knowledge of the mean value of transmission between the transceiver and target ports is an excellent predictor of reconstruction quality for both the physically measured sona and the synthetic sona methods. The higher the mean of $|S_{21}|^2$ in the given bandwidth of the pulse, the higher the quality of the reconstruction.

6.3.3 Synthetic Sona Duration Constraint

The synthetic sona duration is limited first by the computation cost and accumulation of error in the short orbit calculation. Since the number of orbits increases exponentially with orbit length, while the influence of each orbit decreases exponentially due to loss, it is more efficient to only calculate synthetic sonas with orbits within a length limit, depending on the computational budget. The ray-chaotic property of the billiard ensures that no ray is trapped inside the cavity without eventually reaching a port, but it also makes errors accumulate exponentially, at a rate determined by the largest Lyapunov exponent for the nonlinear map describing the ray trajectories. Hence the later part of the synthetic sona may contain more

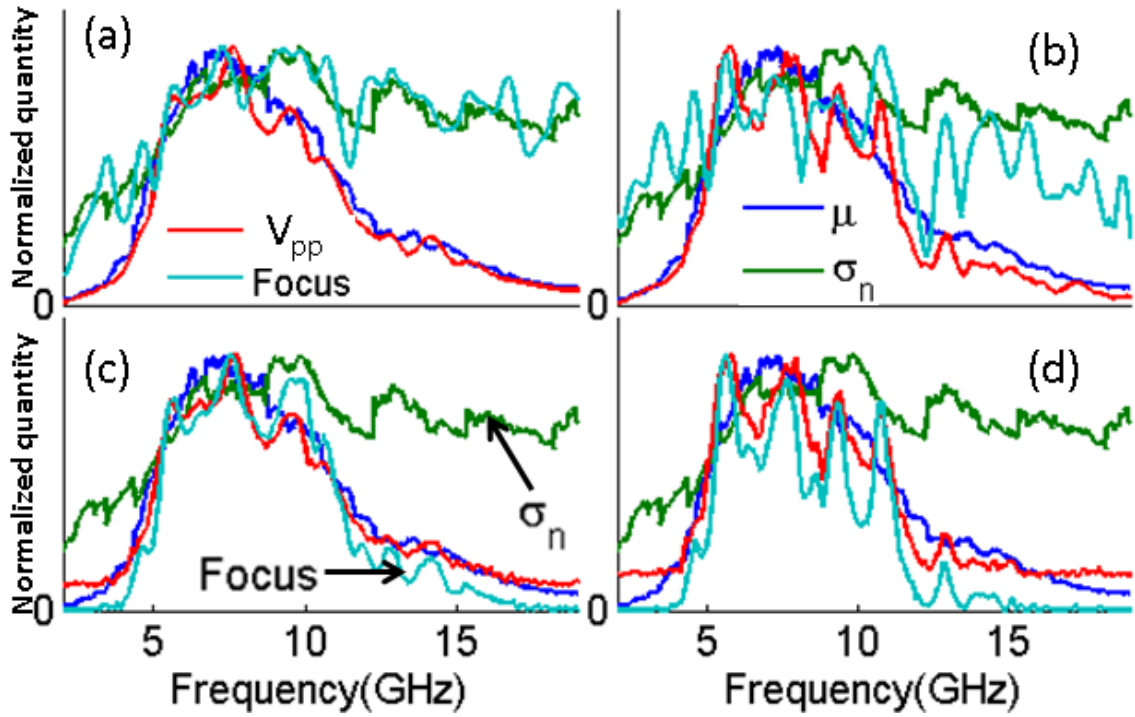


Figure 6.4: Reconstruction quality (V_{pp} and focus ratio) and $|S_{21}|^2$ statistics (μ and σ_n) measured in the 1/4-bowtie billiard as a function of carrier frequency: (a) (b) when no noise is added; (c) (d) when 2mV Gaussian random noise is added to the sonas and reconstructions. (a) (c) use the physically measured sona method, while (b) (d) use the synthetic sona method. All quantities are plotted normalized to their maximum values.

error than the earlier part.

To see the effects of accumulating errors, we create variations of the bowtie cavity by adding inserts to alter the scattering geometry of some of the walls. The differences between the geometry information of the actual inserts and the one assumed in the synthetic sona calculation are larger than that of the empty bowtie case. To determine the appropriate duration of the synthetic sona, we apply a windowing function to the full synthetic and measured sonas and plot the reconstruction quality (normalized to its saturation value) versus the sona duration in Fig.6.5. The windowing function has a 1.5 ns Gaussian-shaped rise and fall, to avoid introducing higher frequency components. For the measured sona method, both V_{pp} and the focus ratio increase monotonically and eventually saturate when a longer sona duration is utilized. The saturation occurs when most of the sona signal with significant amplitude is used for time-reversal. The application of the windowing function is equivalent to changing ΔT as discussed in section 6.3.1 and this behavior agrees with the findings in Ref [117]. But for the synthetic sona method, the focus ratio is highest when the synthetic sona duration is around $4\sqrt{A}/c(=4.5 \text{ ns})$ for the bowtie with inserts, where c is the speed of light. This is because the shape of the inserts is known with less certainty than that of the empty bowtie, so the accumulation of error is more rapid. The later part of the synthetic sona contributes more to the sidelobes rather than to the reconstruction peak. The V_{pp} of synthetic sona reconstruction also saturates eventually when all synthetic sona duration is utilized.

The synthetic sona duration is limited, but in order to have a good reconstruction the synthetic sona should be close to the $1/e$ amplitude decay time, τ . We

have shown in section 6.3.2 that the duration of the earlier-in-time sidelobe (prior to the reconstruction peak) is determined by the synthetic sona duration, and the decay time of the later-in-time sidelobe (after the peak) is determined by τ . If the synthetic sona is significantly shorter than τ , then the reconstruction will have a small focus ratio with large sidelobes on the later side of the reconstruction, but very little sidelobe on the earlier side, causing it to look more like a sona signal rather than a reconstruction. For the bowtie billiard, the synthetic sona length is 15 ns which is close to $\tau = 14$ ns, so it works well. But if we change to a less well-coupled antenna or decrease the propagation loss such that the decay time τ is much longer, the reconstruction quality drops significantly. This is confirmed with time-reversal experimental results from the superconducting cut-circle cavity which has a very long decay time $\tau_{sc} \approx 153$ ns in the superconducting state and $\tau_{normal} \approx 50$ ns in the normal state. The synthetic sona reconstruction in the superconducting state resembles a typical sona signal with a prominent sidelobe after the peak, while in the normal state it has balanced sidelobes, and thus better focus ratio. The focus ratio is 758 in the normal state with well-coupled antenna, 308 when changed to a less well-coupled antenna, and 123 when it is in the superconducting state with a less well-coupled antenna. For comparison, the focus ratio of an ideal reconstruction without sidelobe and noise in this experimental setup, as defined in section 6.3.1, is $T/6\sigma_t = 3333$.

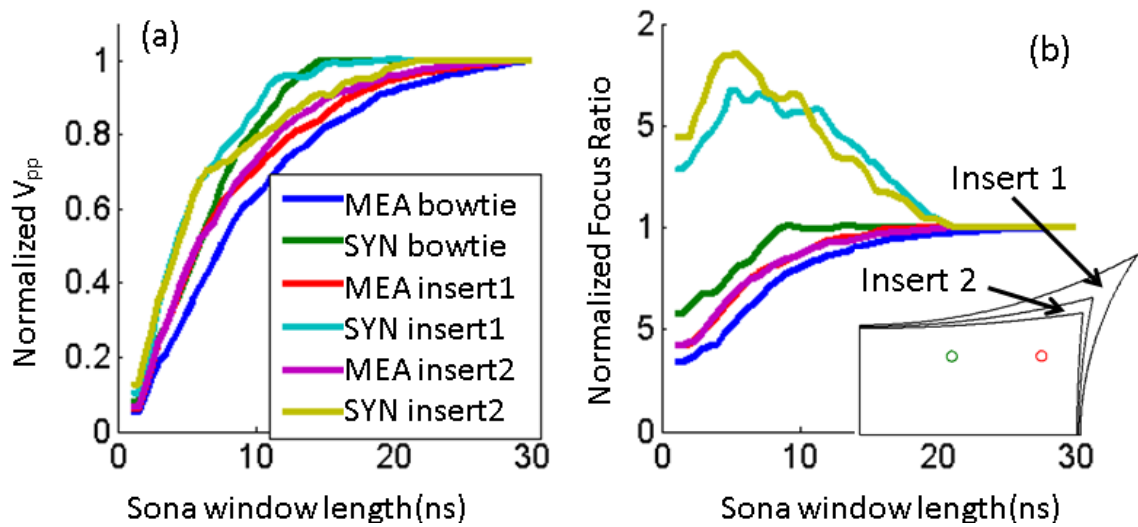


Figure 6.5: Normalized reconstruction quality (normalized to its saturation value) for the physically measured and synthetic sona methods when a windowing function is applied to the sona before being time reversed, so that only the beginning part of the sona is used for the time backward step. The peak-to-peak voltage of the reconstruction is shown in (a) while the focus ratio is shown in (b). “MEA” and “SYN” refer to the physically measured and synthetic sona methods, respectively. “insert1” and “insert2” are two variations of the bowtie cavity geometry when inserts are added, as shown in the inset.

6.4 Conclusion

In this chapter I have shown that focusing of electromagnetic waves at an arbitrary location inside a ray-chaotic billiard can be achieved by using time-reversed synthetic sonas, calculated from the cavity geometry and location of the wave input and focusing points. The focusing quality is quantified and is influenced by cavity loss and port coupling. To achieve a high quality synthetic sona reconstruction with the optimal focus ratio, the billiard should be fairly lossy, and the synthetic sona duration should be close to the $1/e$ sona amplitude decay time, although it is limited by the computation cost and accumulation of error. In many practical applications, the systems are lossy (less reverberating), allowing for the synthetic sona to potentially work well. If the reconstruction amplitude or energy transfer is of more concern, then lower loss and better-coupled antennas (large mean transmission μ) are required.

Chapter 7: Exciting Reflectionless Unidirectional Edge Modes in a
Reciprocal Photonic Topological Insulator Medium

Photonic topological insulators are an interesting class of materials whose photonic band structure can have a band-gap in the bulk while supporting topologically protected unidirectional edge modes. Recent studies [10, 121–125] on bianisotropic metamaterials that emulate the electronic quantum spin Hall effect using its electromagnetic analog are examples of such systems with relatively simple and elegant design. In this chapter, I present a rotating magnetic dipole antenna, composed of two perpendicularly oriented coils, that can efficiently excite the unidirectional topologically protected surface waves in the bianisotropic metawaveguide (BMW) structure recently realized by Ma, et al. [10], despite the fact that the BMW medium does not break time-reversal invariance. In addition to achieving high directivity, the antenna can be tuned continuously to excite reflectionless edge modes to the two opposite directions with various amplitude ratios. We demonstrate its performance through experiment and compare to simulation results. This work is also published in Ref. [126].

7.1 Introduction

Topological insulators [127, 128] are a class of materials that are insulating in the bulk and are conducting only on the edge or surface. These materials have attracted much research effort because of the robust transport properties of the edge states in the presence of impurities and disorder in the material. One example of such a system is the integer quantum Hall effect (QHE) in two-dimensional semiconductors, discovered by von Klitzing in 1980 [129], where edge states are unidirectional

and reflectionless. The electronic QHE systems require very low temperatures and strong magnetic fields and thus are difficult to realize. However its electromagnetic counterpart, photonic systems that emulate the spin of electrons and the effects of magnetic field or spin-orbit interaction, have recently enjoyed an explosion of interest [124, 130–139].

Three main types of electromagnetic analog systems have been presented so far: magnetic photonic crystals [140, 141], coupled resonators and waveguides [132, 137, 138, 142] and bi-anisotropic metamaterials [10, 121–125]. In this project, we are interested in exciting and measuring the topologically protected surface waves (TPSWs) in the bi-anisotropic metawaveguide (BMW) structure recently realized by Ma, et al. [10]. This metawaveguide supports photonic modes that have the same topological nature as the electronic states in graphene with strong spin-orbit coupling, as described by the Kane-Mele Hamiltonian [143, 144]. A more distinguishing feature of this BMW is that it does not require broken time-reversal symmetry, as utilized in previous studies [130, 141, 145], thus bringing a new genre of topological insulators. Furthermore, the BMW structure is based on the quantum spin-Hall effect, and can be scaled to higher frequencies, far beyond the regime where ferrite-based non-reciprocal systems will work. Here I demonstrate for the first time excitation of a uni-directional TPSW in this reciprocal medium.

7.2 Design and Simulations

The design of the quantum spin Hall analog BMW structure follows three steps [121, 124] and in this section we discuss the geometry and the simulation result for each step.

- Graphene-like lattice. The structure begins with a parallel plate waveguide filled with cylindrical metal rods regularly arranged in a hexagonal graphene-like lattice that connect the upper and lower plates. The dimensions, such as the rod radius, height and lattice spacing, are carefully tuned such that the transverse electric (TE) and magnetic (TM) propagating electromagnetic modes are degenerate at the K (K') point in the Brillouin zone, where there is a Dirac point in the photonic band structure. This degeneracy is essential to creating a spin-like degree of freedom, which can be interpreted as the phase relationship between TE and TM modes of the metamaterial, in-phase for the spin-up and out-of-phase for the spin-down states.
- Adding symmetry-breaking air gap. In the second step, a symmetry-breaking air gap between the metal rods and the top plate is introduced, creating bi-anisotropy and forming a band-gap at the K(K') point that provides the photonic insulating behavior in the bulk.
- Forming a TPSW-supporting interface. Finally, combining two such Quantum Spin Hall (QSH) BMW structures, one with an air gap on the top plate and another one with an air gap on the bottom plate, forms an interface

that supports the TPSWs. The TPSWs exhibit reflectionless unidirectional propagation in first-principles simulation using COMSOL, and also in a recent experiment [123].

In the following section, we experimentally demonstrate the launching of unidirectional TPSWs on such an interface by means of a rotating magnetic dipole antenna. It was suggested in [10] that the BMW is also chiral, i.e. it enables unidirectional excitation of TPSWs by a circularly polarized electric or magnetic dipole. While other chiral photonic waveguides have been recently realized [146], the proposed BMW would represent the first example of a chiral photonic circuit with topological protection against back-reflections without the use of ferrite or synthetic gauge fields to break time-reversal symmetry.

7.3 Experiment

A BMW with an interface between two topologically nontrivial domains is constructed as in Ref. [10, 123] with waveguide height $h_0 = 36.8\text{mm}$, rod diameter $d_0 = 12.7\text{mm}$, period $a_0 = 36.8\text{mm}$, air gap size $g_0 = 5.5\text{mm}$. The structure diagram is shown in Figure 7.1, which is the Figure 1 in Ref. [10]. The designed center frequency for the bulk insulating band-gap is around 6.08 GHz, as shown in Fig. 7.2 (a). It has been shown in simulation that TPSWs propagate along the interface with high transmission ($T > 0.9$) over nearly the entire bulk band-gap [10], and also in experiment that the TPSWs are observed to boost the transmission by nearly 30 dB between 5.87 GHz and 6.29 GHz compared to the bulk transmission [123]. The

source antenna used in [123] is a linear dipole antenna which excites both left-going and right-going TPSWs. Our goal is to excite TPSWs that only propagate towards one direction and to further control the directivity and relative amplitude of the excited waves, and also to demonstrate that a circularly polarized (CP) dipole placed inside an air gap of the BMW structure excites a unidirectional guided wave.

In order to efficiently excite the TPSW in the BMW structure, the source must be placed at a location where the edge mode field is most intense and it must generate a field profile that matches with the edge mode at that location. By inspecting the numerically calculated intensity profiles of the magnetic field projected onto the circularly polarized basis in Fig. 7.2 (b) - (e) for the spin-up and spin-down eigenmodes belonging to the two valleys of the Brillouin zone, the 5.5mm air gap between the metal plate and cylinder rod was identified as the best place to locate the source. At that location the field profile is a rotating magnetic dipole around the center frequency of 6.08 GHz. The right circularly polarized (RCP) component of the magnetic field is maximized for the forward-propagating spin-up eigenmodes, and vanishes for the backward-propagating spin-down eigenmodes. This implies chirality, i.e that an RCP magnetic dipole should excite only forward TPSWs. The spin-up and spin-down surface modes have opposite handedness for the rotating magnetic field at this location [10]. As shown in Fig. 7.2, a RCP magnetic dipole only excites the right-going modes. The direction of propagation is locked to the spin state, allowing for uni-directional TPSW propagation depending on the sense of rotation of the magnetic dipole antenna. Mechanically rotating a loop antenna at a rate on the order of 10^9 revolutions per second is too difficult to achieve. Instead,

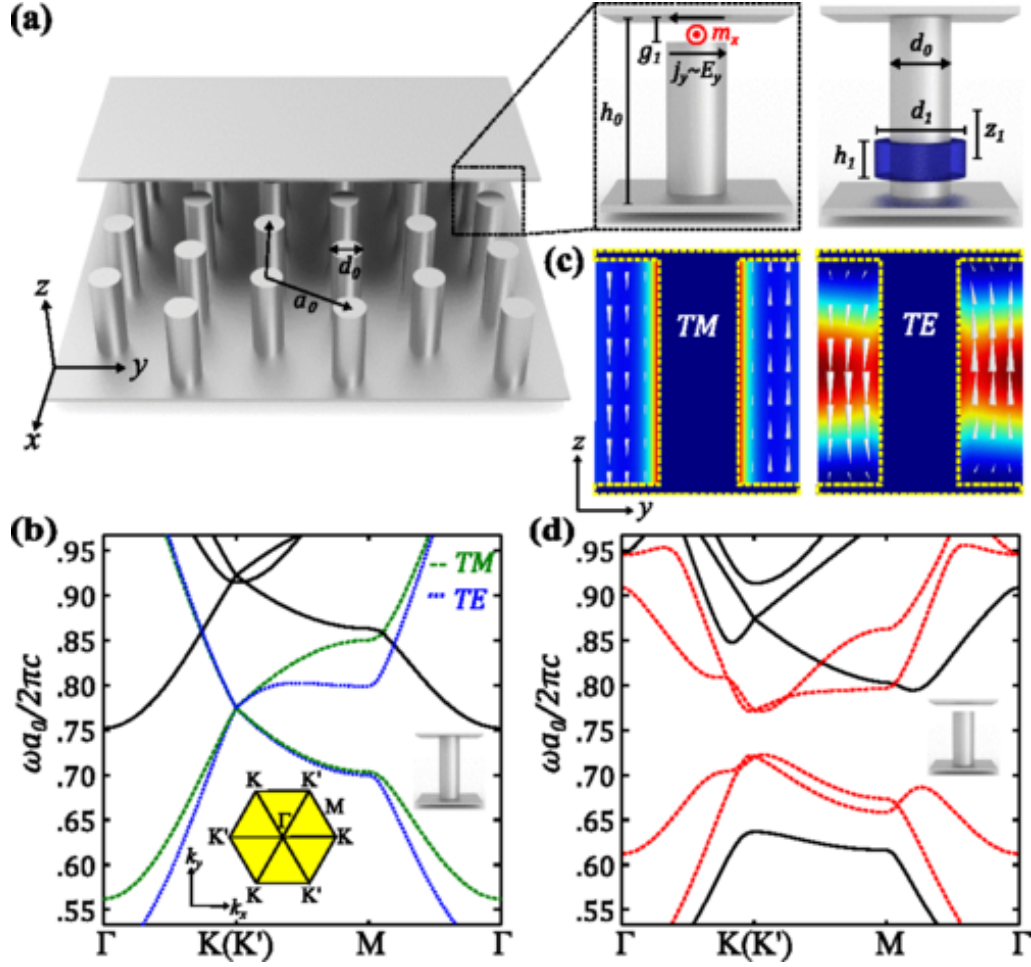


Figure 7.1: Figure 1 in Ref. [10]. BMW as a photonic topological insulator. (a) Schematic of the BMW. Part of the top metal plate is removed to reveal the bed-of-nails structure below. The enlarged regions on the right illustrate the origin of the bianisotropic response. Right inset: an equivalent way to produce bianisotropy by adding an asymmetrically placed metallic volume (washer) around the rod. (b) PBS of spin-degenerate metawaveguide with TE and TM modes forming doubly degenerate Dirac cones at K points. (c) Field profiles of the degenerate TE and TM mode at the K point. Colors: energy density. Arrows: electric field for the TM mode and magnetic field for the TE mode. Yellow dashed line: metallic border. (d) PBS with the band gap induced by the bianisotropy of the metawaveguide. Dashed lines in (b) and (d): TE and TM bands of interest.

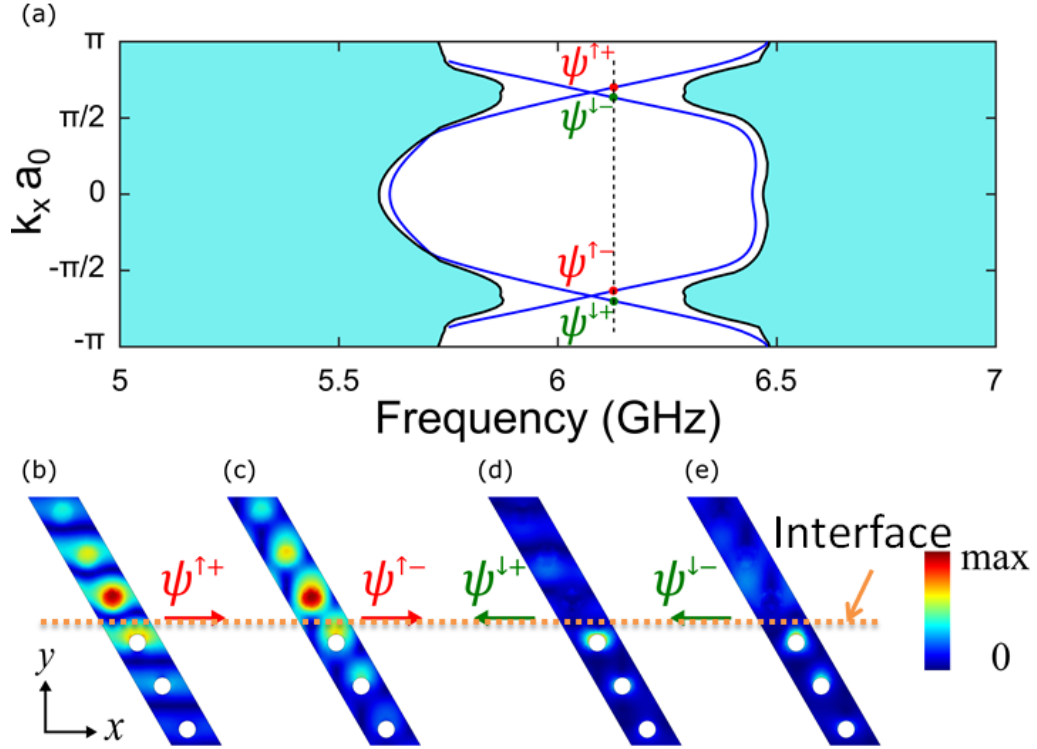


Figure 7.2: (a): Numerically calculated band structure of the waveguide, where four edge modes have been labeled. (b) to (e): Field profile $|H_x - iH_y|$ of the four edge modes at 6.13GHz (shown in (a) as a dashed line). It is clear that only the two spin-up states (from the two valleys), but none of the spin-down states, can be excited by a right circularly polarized magnetic dipole.

we use two loop antennas, perpendicularly positioned to each other, with two ~ 6 GHz sinusoidal input voltage waves with variable phase shift as $v_A(t) = V_A \cos(\omega t)$, $v_B(t) = V_B \cos(\omega t + \phi)$ to antennas A and B, respectively. By setting $V_A = V_B$ and $\phi = +(-)\pi/2$, a clockwise (or counter-clockwise) rotating magnetic dipole is formed. Furthermore, by tuning ϕ one can continuously vary the amplitude of the left or right going modes, providing more control over the directivity.

Circularly polarized (CP) magnetic dipole antennas have been introduced in several fields. In plasma physics, magnetic dipole antennas are used to study the interaction of rotating magnetic fields with plasma [147, 148]. And in magnetic

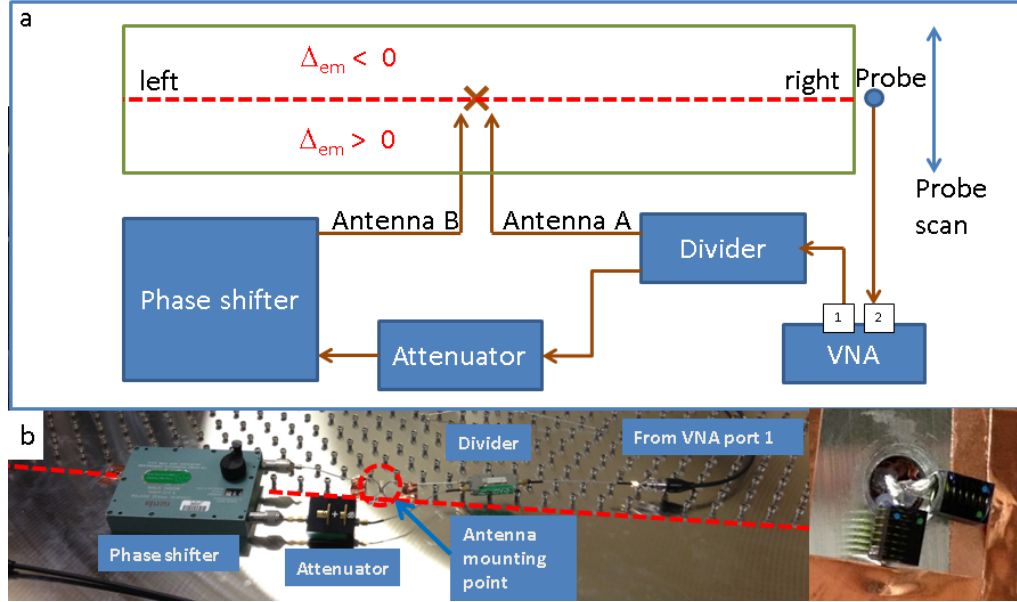


Figure 7.3: (a) Schematic of the experimental setup. Δ_{em} is the bianisotropy coefficient [10] and the interface is defined by the boundary of the two regions with Δ_{em} of opposite sign, denoted by a red dashed line. (b) Photograph of the top of the BMW structure showing the corresponding elements in (a). The inset shows the arrangement of the two loop coils which are in the air gap of a cylinder at the interface.

resonance imaging technology, two mutually perpendicular RF coils, also called quadrature coils, can improve sensitivity by up to 41% and reduce power consumption by half compared to linear RF coils [149, 150]. In our case two perpendicularly placed RF coils is quite effective and simple to implement. The arrangement of this antenna is similar to the turnstile antennas (also known as crossed dipole antennas) [151–153], widely used in satellite communications, consisting of two crossed electric dipoles fed with quadrature phase shift. However the electric dipole in the turnstile and the magnetic dipole in our design are very different in nature.

A rectangular BMW structure is created (1.7 meters by 0.74 meters), consisting of 45 by 20 unit cells, with a single interface bisecting the structure in the length-wise direction, as shown in Figure 7.3. The rotating dipole antenna is placed

inside the BMW structure near the middle of the interface. The source of microwave signals is the first port of an Agilent E5071C Vector Network Analyzer (VNA), and that signal is split approximately in half by a HP87304C power divider, creating two branches. One branch goes directly to loop antenna A while the other one is connected to a variable attenuator and variable phase shifter before going to the other loop antenna, B. The two loop antennas are in fact air-core RF coil inductors (Coilcraft model number 1812SMS-56NJLB, $R=6.2$ mOhm, $L=56$ nH at 150 MHz) with one end grounded to the metal plate and the other end soldered onto the center conductor of the feed coaxial cable, as shown in the inset of Figure 7.3. Hence the input signal from the VNA is divided, phase-shifted and then sent to the two RF coils that each creates a magnetic dipole. By controlling the value of the phase shift, it can produce a linearly, circularly or elliptically polarized magnetic dipole source.

A transmission experiment is performed by placing a simple electric dipole antenna [63] at the edge of the BMW structure on either the left or right side where the interface comes to the edge to pick up and record the transmitted signal at port 2 of the VNA. We then move the probe along the edge to do a lateral scan (see Fig. 7.3(a)), recording the transmission amplitude as a function of the probe's location and also the phase difference between the two loops. The experimental result for the transmission when the probe is at the midpoint of the edge is shown in Fig 7.4. The transmission data when we vary both the probe location and the phase difference can be found in [Supplementary Material Movie 1](#) in Ref. [126]. From the midpoint transmission plot, the excited wave is propagating primarily to the left (right) when the phase difference is close to 2π (1.27π) confirming the successful excitation of a

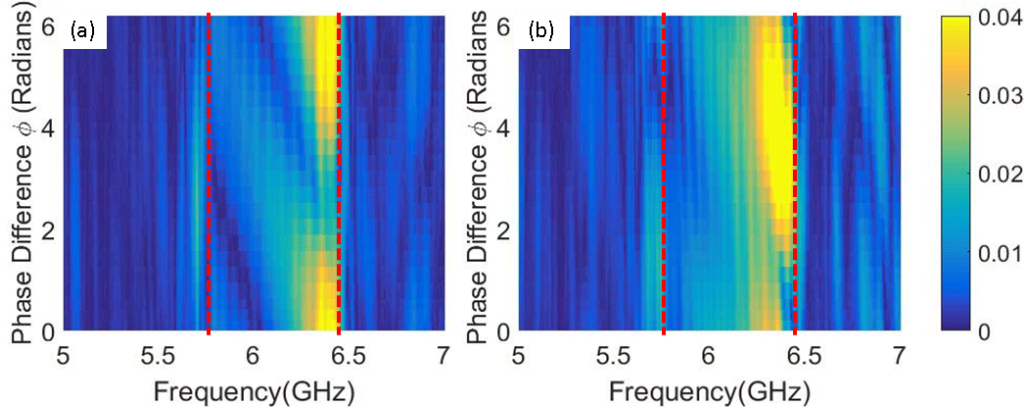


Figure 7.4: Transmission amplitude at the (a) left and (b) right side of the BMW interface as a function of frequency while varying the phase difference ϕ of the two driving loop antennas. The probe is positioned at the center of the edge. The BMW bulk band gap extends from 5.80 GHz to 6.47 GHz, as shown with the vertical dashed lines.

predominantly unidirectional edge mode. It is also clear that the transmission has a period of 2π with respect to the phase difference in the frequency range of 5.80 GHz to 6.47 GHz, which corresponds to the plateau of enhanced transmission due to TPSWs in Figure 1 of Ref. [123]. The TPSWs are more efficiently excited at higher frequencies, with a peak at 6.47 GHz. The [Supplementary Material Movie 1](#) in Ref. [126] further demonstrates that the TPSWs are propagating along the interface, resulting in a spatial focus around the center of the edge, and that the left- and right-going TPSWs are controlled by varying the phase difference ϕ .

7.4 Analysis

Naively, it is expected that when $V_A = V_B$ and $\phi = \pi/2$, a clockwise rotating dipole would excite a purely left or right going edge mode, depending on whether the dipole is placed at the bottom or upper air gap, and thus the left transmission should reach

its maximum while the right transmission should be zero. However, the experiment is affected by several non-idealities beyond our control. The two loop antennas are different in their geometry, the coupling to the edge mode, and the actual power received from input feed lines. Hence we must loosen the restrictions on V_A , V_B and ϕ to obtain a more general result. To keep the total input power constant while giving the two loop antenna variable portions of the power, we parameterize the amplitudes of the driving voltage waves with an angle θ as $V_A = V_0 \cos \theta$ and $V_B = V_0 \sin \theta$, where $\theta \in [0, \pi/2]$.

We performed a numerical simulation of a finite-size BMW structure, whose detailed geometry can be found in Figure 7.5 and in [Supplementary Material](#) of Ref. [126]. The simulation calculates the transmission from antenna A and B to the left and right side probes in Fig. 7.3 and expresses it as a 2-by-2 scattering matrix $\mathbf{S}_{\text{sim}} = \begin{bmatrix} S_{LA} & S_{LB} \\ S_{RA} & S_{RB} \end{bmatrix}$, where S_{ij} is the transmission from j to i , $L(R)$ represent left (right) side probe, $A(B)$ represent antenna A (B) respectively.

Given the simulation result of \mathbf{S}_{sim} , and that $V_A = V_0 \cos \theta$, $V_B = V_0 \sin \theta$ (to keep the total input power constant), we can calculate the transmission to the left or right side with different driving amplitudes in the two antennas (θ) and different phase shift values (ϕ). To calculate transmission to the right side for instance one has $V_R = V_A S_{RA} + V_B e^{-i\phi} S_{RB} = V_0 (S_{RA} \cos \theta + e^{-i\phi} S_{RB} \sin \theta)$ where $e^{-i\phi}$ controls the phase difference between the A, B antenna. Figure 7.6 shows the resulting transmission to the left and right probes as a function of θ and ϕ , at two different frequencies within the bulk band-gap of the BMW structure. Since \mathbf{S} is frequency

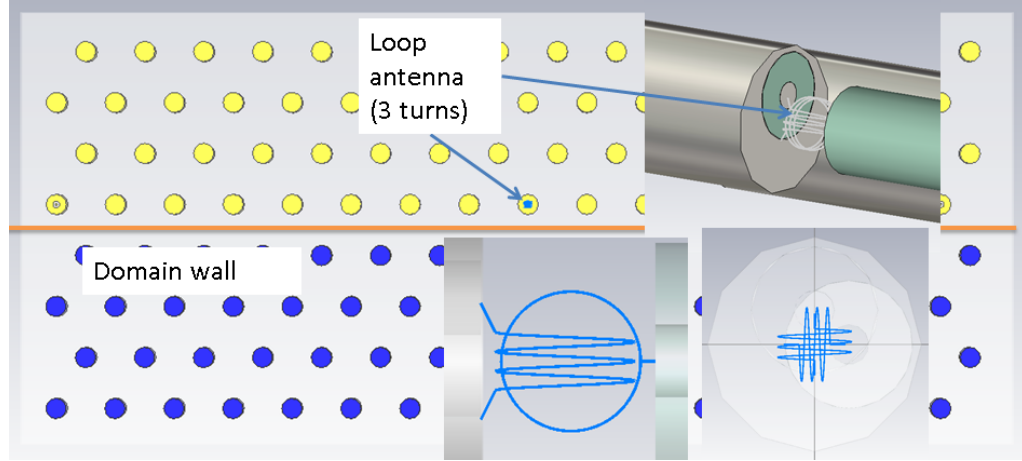


Figure 7.5: Simulated BMW structure with TPSW-supporting interface in CST with 16 period long and 8 period wide graphene-like lattice structure of rods. The two loops making up the rotating magnetic dipole antenna are perpendicularly placed with two independent driving coaxial cable inputs.

dependent and is simulated over the whole band-gap, choosing a different frequency could lead to a different plot but the unidirectional propagation property should remain. Focusing on the minimum and maximum values of the transmission, we observe a number of key features:

- The transmission has a period of 2π with phase difference ϕ .
- When the transmission to the left side is at its maximum, the transmission to the right side is not zero and is not exactly at its minimum (but is near it).
- If θ and ϕ are chosen wisely, one can effectively eliminate the transmission to one side although the transmission to the other side is not at its maximum.

Note that all these observations regarding the results of the simulations are in agreement with measurements. To more firmly connect the simulation results with the experimental data, we followed these steps:

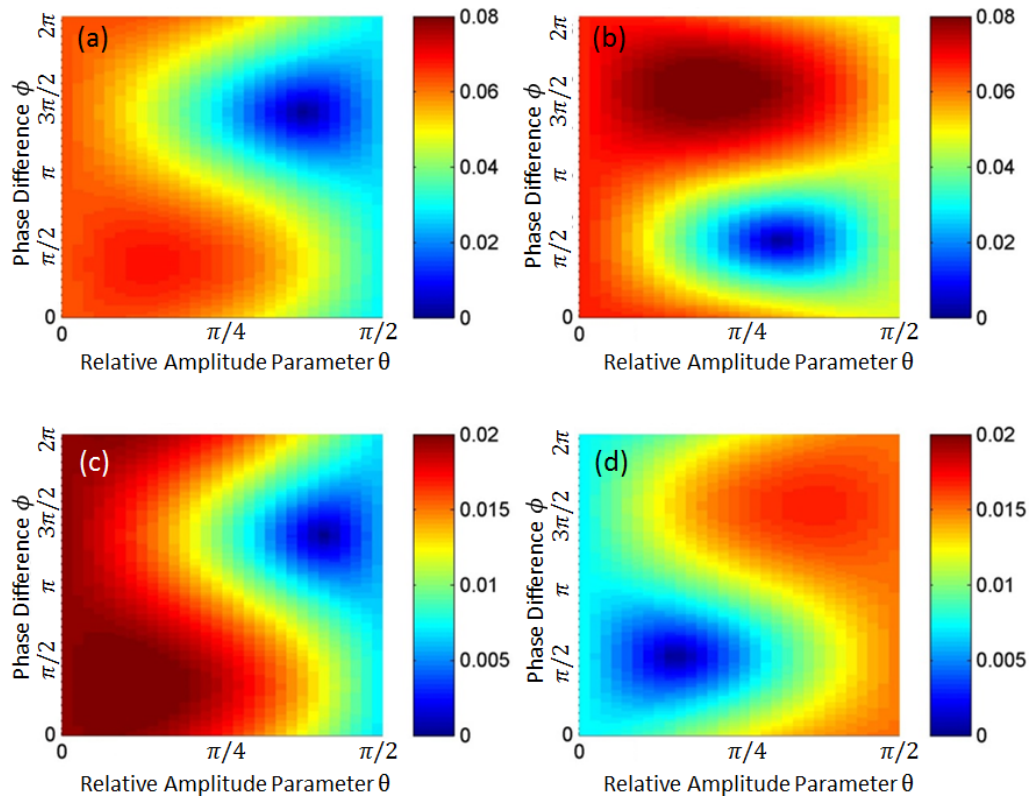


Figure 7.6: CST simulation results for transmission amplitude to the left and right side of the BMW structure while varying both the phase difference ϕ and driving amplitude (parameterized by angle $\theta \in [0, \pi/2]$) of the two loop antennas. Results are shown for (a) left, (b) right 6.47 GHz and (c) left, (d) right 6.08 GHz.

1. Model the transmission process in the experiment using a 2-by-2 scattering matrix, $\mathbf{S}_{\text{exp}} = \begin{bmatrix} S_{LA} & S_{LB} \\ S_{RA} & S_{RB} \end{bmatrix}$. The experimental data can then be expressed as

$$\begin{bmatrix} L_1 & L_2 & \dots & L_N \\ R_1 & R_2 & \dots & R_N \end{bmatrix} = \frac{1}{\sqrt{2}} \mathbf{S}_{\text{exp}} \begin{bmatrix} 1 & 1 & \dots & 1 \\ e^{-i\phi_1} & e^{-i\phi_2} & \dots & e^{-i\phi_N} \end{bmatrix}, \quad (7.1)$$

where ϕ_i ($i = 1, 2, \dots, N$) are the $N = 31$ known experimental values of the loop antenna phase differences, and L_i R_i are the measured complex transmission data taken at the left and right sides of the BMW interface edge. It is assumed that the amplitudes of the driving voltage on the two antennas are both $V_0/\sqrt{2}$. All variables in Eq. 7.1 are functions of frequency.

2. Fit the experimental data to this model to obtain the \mathbf{S}_{exp} matrix as a function of frequency. This fit is strongly over-determined, but is found to be very good for all frequencies (with normalized mean-square-error of around 7%) and both left or right side transmission.
3. Calculate the expected left side transmission for $M = 91$ values of θ and $N = 31$ values of ϕ using $L_{nm} = S_{LA} \cos \theta_m + e^{-i\phi_n} S_{LB} \sin \theta_m$, where $n = 1, 2, \dots, N$, $m = 1, 2, \dots, M$.

The same calculations are done for right side transmission, and the result for transmission amplitude is shown in Figure 7.7 (a) and (b).

It is clear that Fig.7.6 (simulation) and Fig.7.7 (deduced from experimental

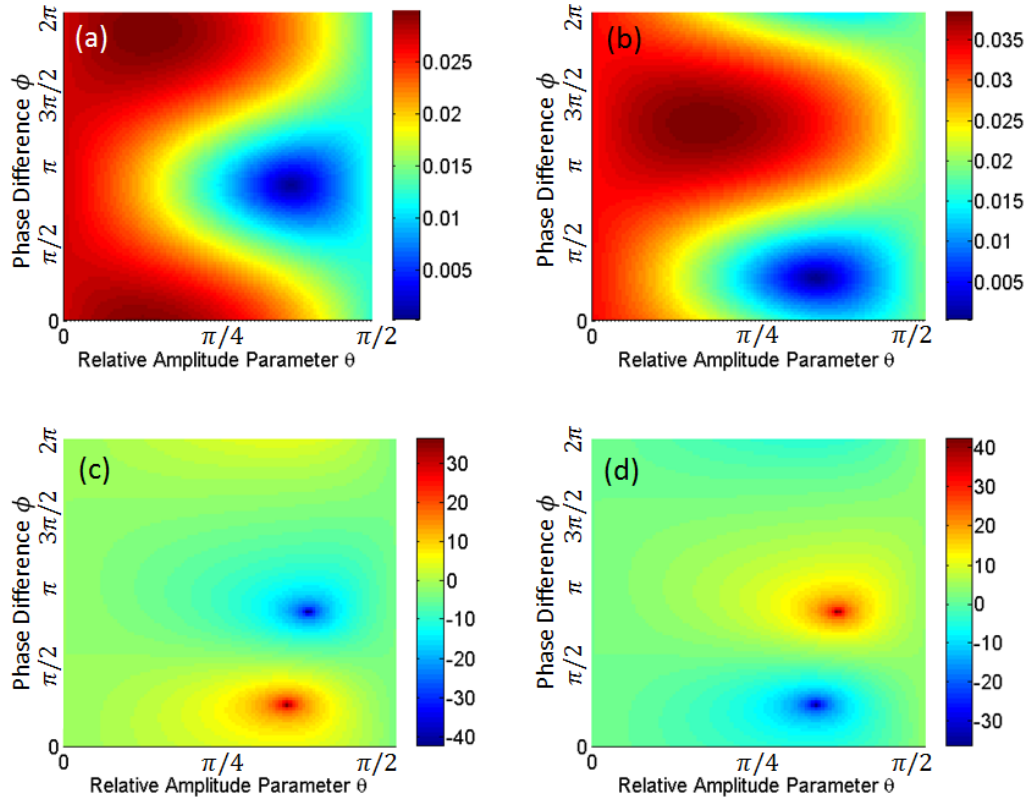


Figure 7.7: Transmission amplitude to the (a) left and (b) right side when varying both the phase difference ϕ and the input power (parameterized by θ) of the two loop antennas as deduced from the data at a frequency of 6.38 GHz. To examine the directivity, we plot the ratio of (c) left to right side and (d) right to left side transmission amplitude (in dB) as a function of θ and ϕ .

		ϕ (degrees)	θ (degrees)	T_L	T_R	$20 \log(\frac{T_L}{T_R})$
Left	Max	334.5	23.6	0.0297	0.0293	0.118 dB
	Min	156.4	65.5	0.0002	0.0254	-42.1 dB
Right	Max	229.1	30.0	0.0225	0.0384	-4.64 dB
	Min	47.3	60.0	0.0197	0.0003	36.3dB

Table 7.1: Summary of extreme transmissison values as deduced from experimental data where T_L and T_R are transmission amplitude to left and right, respectively.

data) have very similar patterns. By choosing the appropriate θ and ϕ values, one can minimize the one side transmission amplitude to as low as 0.0002 or tune the ratio of the left to right transmission amplitude (Fig.7.7 (c) and (d)) from -42 dB to +36 dB. A summary of the results for extreme values of transmission is given in Table 7.1. All of this confirms that the rotating magnetic dipole antenna is an effective way to excite directional edge modes in the BMW structure with tunable directivity.

In terms of applications, our results can be used for selective feeding of a waveguide in either direction. This can be used to feed a beam-forming array of antennas through a series of sensitive and rapidly tunable structures. The current design can also handle high microwave powers making it attractive for transmit applications. Since the directivity of the edge modes can be varied by ϕ , it can be used as a modulation method for communications.

7.5 Ferrite Induced Non-reciprocity

As a recently proposed continuation of this project, we are adding ferrite into the BMW structure to make it non-reciprocal. Combined with the TPSWs' inherent reflectionless nature the non-reciprocal BMW could be used to make circulators or

isolaters. My colleague Shukai Ma has implemented these materials, as discussed in these publications: [\[154, 155\]](#)

7.6 Conclusions

In conclusion we have experimentally demonstrated excitation of a unidirectional edge mode using a rotating magnetic dipole antenna consisting of two perpendicular coils. The edge mode in this time-reversal symmetry preserved Bianisotropic Metawaveguide has been demonstrated to be unidirectional to the level of one part in 10^4 . In addition, the degree of directionality can be tuned continuously using the method that we have outlined here, allowing for novel applications in the field of communications, for example phased array antennas.

Chapter 8: Conclusions

In this thesis, I have studied wave propagation properties in two types of media: wave chaotic enclosures and bianisotropic meta-waveguides.

For ray-chaotic cavities in the frequency domain, I extended the Random Coupling Model from room temperature full-scale cavities to low temperature miniature cavities where the universal statistical properties, determined by the loss parameter α , remain the same between the two. I designed the miniature setup to study wave propagation in complex networks of coupled cavities. The design is extendable, re-configurable and efficiently utilizes the available lab resources, including sample space in the cryostat, material and construction cost. This establishes the foundation for future studies of universal statistical properties in wave chaotic enclosures.

In the time domain, I utilized the time-reversal mirror technique to focus electromagnetic waves at an arbitrary location inside a wave chaotic enclosure by injecting a numerically calculated wave excitation signal. Through this work, I tested the limits of utilizing the deterministic properties defined by the cavity geometry through numerical simulation and experimental testing.

For wave propagation in bianisotropic meta-waveguides, I experimentally demonstrated excitation of a unidirectional edge mode using a rotating magnetic dipole antenna consisting of two perpendicular coils. The degree of directionality can be tuned continuously by tuning the phase shift between the source signal sent to the two dipole antennas.

Overall, this thesis builds the foundation for further studies in wave chaotic enclosures for its universal statistical properties, and tested the limit of its deterministic properties defined by the cavity geometry. It also demonstrated in experiment

the excitation of a unidirectional edge mode in a Bianisotropic Meta-waveguide, allowing for novel applications in the field of communications, for example phased array antennas.

8.1 Prior Works

This work is only made possible by building on top of the foundations that prior students in my research group have laid before me.

Thanks for the work of Sameer Hemmady [2], Xing Zheng [18, 19] and Jen-Hao Yeh [36–38] on the Random Coupling Model, I not only learned the theory of RCM but also gained first hand experience in extracting the universal statistical property, e.g. the loss parameter α , from experiments on the bow-tie cavity and the gigabox, as well as from Monte Carlo simulations of random matrices with Matlab programming.

Thanks to Bisrat Addissie’s work on radiation efficiency in one-port systems [7], I was able to extend it to the two-port setup for the scaled cavities experiment in Chapter 3. It is important to quantify the lossyness of the ports and the free-space propagation paths and then properly exclude them from the overall RCM loss parameter α in order to obtain the correct universal statistical properties of the enclosure of interest.

For the work on photonic topological insulators in Chapter 7, Kueifu Lai and Tzuhsuan Ma in Prof. Gennady Shvets’ research group had already built and simulated the Bianisotropic Meta-waveguide structure consisting of cylindrical rods

arranged in a hexagonal lattice. Thanks for their theoretical work and the existing experimental setup, I was able to complete the experiments during my two short visits to their lab at the University of Texas, Austin.

8.2 Future Work

The multiple scaled cavity experiment discussed in Chapter 5 is really designed to be flexible enough to test many different complex networks, from a simple cascade of connected cavities, as Shukai Ma has discussed in [9, 69], to more complex ones as illustrated in Figure 2.17.

In future studies, one can include extensions of the 1X2 unit box as frequently shown throughout Chapter 5, such as a 2X2 unit box that can couple to 4 other boxes, serving as a node in a more complex network. Then one can start to design and study networks that are far more interesting than a simple cascade.

Another direction is to study the interaction between cavities with different loss parameters α . For example, by coupling three cavities with different volume, e.g. a 1X2 box connected to a 1X3 box which is then connected to a 2X2 box, we can create a cascade of cavities with increasing α . Or we can reduce cavity α by adding metallic objects inside the 1X2 unit box to reduce its inner volume.

Finally, one can also study the effect of the opening that connects the cavities, such as its shape, size, thickness or the relative location in the cavity wall (e.g. positioned right at the center of the wall or close to the edges).

Following the same design principles, the same setup should be able to power

many future experiments on the subject of statistical properties of complex networks of ray-chaotic cavities.

Appendices

Chapter A: MATLAB Script For Generating Normalized Impedance
Ensembles For 2-port Systems

The following script is written by Sameer Hemmady and is modified by Bo Xiao. The purpose of the script is to use Random Matrix Theory and the Random Coupling Model to numerically generate normalized impedance ensembles for a 2-port complex scattering system.

The input parameter is *Ktwiddle_vector*, which is essentially an array of RCM loss parameter α values. For each α value, the script will generate random matrices and calculate the normalized impedances ξ_{11} , ξ_{12} , ξ_{21} and ξ_{22} according to RMT and the RCM, and save their real and imaginary part separately, in a total of 8 columns ($\text{Re}[\xi_{11}]$, $\text{Im}[\xi_{11}]$, $\text{Re}[\xi_{12}]$, $\text{Im}[\xi_{12}]$, $\text{Re}[\xi_{21}]$, $\text{Im}[\xi_{21}]$, $\text{Re}[\xi_{22}]$, $\text{Im}[\xi_{22}]$), in the file named “RMTZ-2.1.txt” for the case of $\alpha = 2.1$.

To obtain the PDF curve of the impedances for a certain α value, one needs to first load the corresponding text file into Matlab workspace, then use the Matlab function “hist” or “histcounts” to get the bin sizes and counts, and finally normalize the counts to have an unit area enclosed by the curve and the x-axis.

The quality of the PDF depends on the size of the data set: the larger the data set you have, the better the PDF quality would be. As the data set grows larger, the PDF curve becomes a smoother line. The data size is controlled by the number of iterations (“runs”) and the number of runs per iteration (“samples”). The more iterations and runs you perform, the larger the data set would be, but it also takes a longer calculation time and larger disk space to store the text file.

Matlab Code

```

1 % This program creates the ensemble of Normalized z from the
    Random Matrix Hamiltonian
2 N=600;% Size of Hamiltonian
3 samples=100;% Number of runs per iteration. "samples" number
    of znorm renditions will be written to output file
4 runs=10000;% Number of iterations. Final size of output file
    will contain "runs*samples" number of znorm entries.
5 % Setting the value of damping, i.e. the loss parameter
6 Ktwidle_vector=0.1:0.1:20;
7 [mask1,mask2]=mask(N);
8 outlier1=(N/2 0.01)*ones(1,samples,'gpuArray'); % removing
    the outliers
9 outlierN=(N/2 0.01)*ones(1,samples,'gpuArray'); % removing
    the outliers
10 for Ktwidle_ind=1:length(Ktwidle_vector)
11     Ktwidle=Ktwidle_vector(Ktwidle_ind);
12     % if file already exist, jump to the next iteration
13     filename=strcat('RMTZ_',num2str(Ktwidle),'.txt');
14     if exist(filename,'file')~=0
15         display([filename ' exist , skip'])
16         continue;
17     end

```

```

18     display(filename)
19     eigen=zeros(N,samples,'gpuArray'); % Initializing the
      eigen matrix
20     z11=zeros(runs,samples,'gpuArray');
21     z12=zeros(runs,samples,'gpuArray');
22     z21=zeros(runs,samples,'gpuArray');
23     z22=zeros(runs,samples,'gpuArray');
24     parfor p=1:runs,
25         [eigen]=RMT_eigen(N,samples,mask1,mask2);
26         %eigen=gather(eigen);
27         Elevel=zeros(N,samples,'gpuArray');
28         Elevel=(N/(2*pi))*(pi+2*asin(complex(eigen./sqrt(2*N
      )))+2.*(eigen./sqrt(2*N)).*sqrt(complex(2*N eigen
      .^2))/sqrt(2*N)) N/2;% Mapping the eigenvalues
      from the semi circle to have uniform spacing
29         Elevel(1,:)=outlier1; % removing the outliers
30         Elevel(N,:)=outlierN; % removing the outliers
31         green=(1i/pi)./(Elevel+1i*Ktwidle);% Setting up
      green's function
32         CoupleMatrix1=gpuArray.randn(N,samples);
33         CoupleMatrix2=gpuArray.randn(N,samples);
34         z11(p,:)=sum(CoupleMatrix1.*green.*CoupleMatrix1);

```

```

35     z12(p,:) = sum(CoupleMatrix1 .* green .* CoupleMatrix2);
36     z21(p,:) = sum(CoupleMatrix2 .* green .* CoupleMatrix1);
37     z22(p,:) = sum(CoupleMatrix2 .* green .* CoupleMatrix2);
38     end
39     z11 = gather( transpose( z11(:) ) );
40     z12 = gather( transpose( z12(:) ) );
41     z21 = gather( transpose( z21(:) ) );
42     z22 = gather( transpose( z22(:) ) );
43     fid = fopen( filename, 'a+' ); % output file name
44     result = [ real( z11 ); imag( z11 ); real( z12 ); imag( z12 ); real( z21
               ); imag( z21 ); real( z22 ); imag( z22 ) ];
45     fprintf( fid, '%8.5f\t %8.5f\t %8.5f\t %8.5f\t %8.5f\t
               %8.5f\t %8.5f\t %8.5f\t \n', result );
46     fclose( fid );
47     end;

```

Bibliography

- [1] Final report on the august 14, 2003 blackout in the united states and canada: Causes and recommendations. Technical report, U.S.-Canada Power System Outage Task Force, 04 2004. <https://www.energy.gov/sites/default/files/oeprod/DocumentsandMedia/BlackoutFinal-Web.pdf>.
- [2] Sameer Hemmady. *A Wave-Chaotic Approach To Predicting And Measuring Electromagnetic Field Quantities In Complicated Enclosures*. PhD thesis, University of Maryland College Park, 2006. <https://drum.lib.umd.edu/handle/1903/3979>.
- [3] Gabriele Gradoni, Jen-Hao Yeh, Bo Xiao, Thomas M. Antonsen, Steven M. Anlage, and Edward Ott. Predicting the statistics of wave transport through chaotic cavities by the random coupling model: A review and recent progress. *Wave Motion*, 51(4):606 – 621, 2014.
- [4] P. D. Desai, H. M. James, and C. Y. Ho. Electrical resistivity of aluminum and manganese. *Journal of Physical and Chemical Reference Data*, 13(4):1131–1172, 1984.
- [5] Virginia Diode, Inc. *VNA Extension Modules Operational Manual*, 2016.
- [6] Z. B. Drikas, J. Gil Gil, S. K. Hong, T. D. Andreadis, Jen-Hao Yeh, B. T. Taddese, and S. M. Anlage. Application of the random coupling model to electromagnetic statistics in complex enclosures. *IEEE Transactions on Electromagnetic Compatibility*, 56(6):1480–1487, Dec 2014.
- [7] Bisrat Addissie, John Rodgers, and Thomas Antonsen. Extraction of the coupling impedance in overmoded cavities. *Wave Motion*, 87, 10 2018.
- [8] Virginia Diode, Inc. *Nominal Horn Specifications*, 2011. <http://vadiodes.com/images/AppNotes/VDI'Feedhorn'Summary'2016.02.pdf>.

- [9] Shukai Ma, Bo Xiao, Zachary Drikas, Bisrat Addissie, Ronald Hong, Thomas M. Antonsen, Edward Ott, and Steven M. Anlage. Wave scattering properties of multiple weakly coupled complex systems. *Phys. Rev. E*, 101:022201, Feb 2020.
- [10] Tzuhsuan Ma, Alexander B. Khanikaev, S. Hossein Mousavi, and Gennady Shvets. Guiding electromagnetic waves around sharp corners: Topologically protected photonic transport in metawaveguides. *Phys. Rev. Lett.*, 114:127401, Mar 2015.
- [11] M. E. Lines. The search for very low loss fiber-optic materials. *Science*, 226(4675):663–668, 1984.
- [12] A. M. Vengsarkar, P. J. Lemaire, J. B. Judkins, V. Bhatia, T. Erdogan, and J. E. Sipe. Long-period fiber gratings as band-rejection filters. *Journal of Lightwave Technology*, 14(1):58–65, Jan 1996.
- [13] K. Tajima, K. Nakajima, K. Kurokawa, N. Yoshizawa, and M. Ohashi. Low-loss photonic crystal fibers. In *Optical Fiber Communication Conference and Exhibit*, pages 523–524, March 2002.
- [14] L. G. Van Uitert and S. H. Wemple. ZnCl₂ glass: A potential ultralowloss optical fiber material. *Applied Physics Letters*, 33(1):57–59, 1978.
- [15] Stanley Kaufman and Jim J Sheu. Optical fiber cable provided with stabilized waterblocking material, February 8 1994. US Patent 5,285,513.
- [16] J. C. Knight, T. A. Birks, P. St. J. Russell, and D. M. Atkin. All-silica single-mode optical fiber with photonic crystal cladding. *Opt. Lett.*, 21(19):1547–1549, Oct 1996.
- [17] Steven Xuefeng Shen. Optical fiber having water swellable material for identifying grouping of fiber groups, November 20 2001. US Patent 6,321,012.
- [18] Xing Zheng, Thomas M. Antonsen, and Edward Ott. Statistics of impedance and scattering matrices in chaotic microwave cavities: Single channel case. *Electromagnetics*, 26(1):3–35, 2006.
- [19] Xing Zheng, Thomas M. Antonsen, and Edward Ott. Statistics of impedance and scattering matrices of chaotic microwave cavities with multiple ports. *Electromagnetics*, 26(1):37–55, 2006.
- [20] Edward Ott. *Chaos in Dynamical Systems*. Cambridge University Press, 2 edition, 2002.
- [21] Richard Holland and Richard St. John. *Statistical electromagnetics*. Taylor & Francis, Philadelphia, 1999.

- [22] Yves Auregan and Vincent Pagneux. Acoustic scattering in duct with a chaotic cavity. *Acta Acustica united with Acustica*, 102(5):869–875, 2016.
- [23] S. Hemmady, T. M. Antonsen, E. Ott, and S. M. Anlage. Statistical prediction and measurement of induced voltages on components within complicated enclosures: A wave-chaotic approach. *IEEE Transactions on Electromagnetic Compatibility*, 54(4):758–771, Aug 2012.
- [24] Gabriele Gradoni, Thomas M. Antonsen, and Edward Ott. Impedance and power fluctuations in linear chains of coupled wave chaotic cavities. *Phys. Rev. E*, 86:046204, Oct 2012.
- [25] Min Zhou, Edward Ott, Thomas M. Antonsen, and Steven M. Anlage. Scattering statistics in nonlinear wave chaotic systems. *Chaos: An Interdisciplinary Journal of Nonlinear Science*, 29(3):033113, 2019.
- [26] Eugene P. Wigner. Characteristic vectors of bordered matrices with infinite dimensions. *Annals of Mathematics*, 62(3):548–564, 1955.
- [27] Hans-Jürgen Stöckmann. *Quantum Chaos: An Introduction*. Cambridge University Press, 1 edition, 3 2007.
- [28] Eugene P. Wigner. On a class of analytic functions from the quantum theory of collisions. *Annals of Mathematics*, 53(1):36–67, 1951.
- [29] Eugene P. Wigner. Characteristic vectors of bordered matrices with infinite dimensions ii. *Annals of Mathematics*, 65(2):548–564, 1957.
- [30] Eugene P. Wigner. On the distribution of the roots of certain symmetric matrices. *Annals of Mathematics*, 67(2):325–327, 1958.
- [31] O. Bohigas, M. J. Giannoni, and C. Schmit. Characterization of chaotic quantum spectra and universality of level fluctuation laws. *Phys. Rev. Lett.*, 52:1–4, Jan 1984.
- [32] Steven W. McDonald and Allan N. Kaufman. Spectrum and eigenfunctions for a hamiltonian with stochastic trajectories. *Phys. Rev. Lett.*, 42:1189–1191, Apr 1979.
- [33] R. L. Weaver. Spectral statistics in elastodynamics. *J. Acoust. Soc. Am.*, 85:1005, 1989.
- [34] C. Ellegaard, T. Guhr, K. Lindemann, H. Q. Lorensen, J. Nygård, and M. Oxborrow. Spectral statistics of acoustic resonances in aluminum blocks. *Phys. Rev. Lett.*, 75:1546–1549, Aug 1995.
- [35] L. L. A. Adams, B. W. Lang, and A. M. Goldman. Observation of discrete energy levels in a quantum confined system. *Phys. Rev. Lett.*, 95:146804, Sep 2005.

- [36] J. A. Hart, T. M. Antonsen, and E. Ott. Effect of short ray trajectories on the scattering statistics of wave chaotic systems. *Phys. Rev. E*, 80:041109, Oct 2009.
- [37] Bo Xiao, Thomas M. Antonsen, Edward Ott, and Steven M. Anlage. Focusing waves at arbitrary locations in a ray-chaotic enclosure using time-reversed synthetic sonas. *Phys. Rev. E*, 93:052205, May 2016.
- [38] Jen-Hao Yeh, James A. Hart, Elliott Bradshaw, Thomas M. Antonsen, Edward Ott, and Steven M. Anlage. Experimental examination of the effect of short ray trajectories in two-port wave-chaotic scattering systems. *Phys. Rev. E*, 82:041114, Oct 2010.
- [39] P. W. Brouwer and C. W. J. Beenakker. Voltage-probe and imaginary-potential models for dephasing in a chaotic quantum dot. *Phys. Rev. B*, 55:4695–4702, Feb 1997.
- [40] J.J.M. Verbaarschot, H.A. Weidenmüller, and M.R. Zirnbauer. Grassmann integration in stochastic quantum physics: The case of compound-nucleus scattering. *Physics Reports*, 129(6):367 – 438, 1985.
- [41] C.H. Lewenkopf and H.A. Weidenmüller. Stochastic versus semiclassical approach to quantum chaotic scattering. *Annals of Physics*, 212(1):53 – 83, 1991.
- [42] F. Beck, C. Dembowski, A. Heine, and A. Richter. R-matrix theory of driven electromagnetic cavities. *Phys. Rev. E*, 67:066208, Jun 2003.
- [43] Y. V. Fyodorov and D. V. Savin. Statistics of impedance, local density of states, and reflection in quantum chaotic systems with absorption. *Journal of Experimental and Theoretical Physics Letters*, 80(12):725–729, Dec 2004.
- [44] Y V Fyodorov, D V Savin, and H-J Sommers. Scattering, reflection and impedance of waves in chaotic and disordered systems with absorption. *Journal of Physics A: Mathematical and General*, 38(49):10731, 2005.
- [45] D. V. Savin, H. J. Sommers, and Y. V. Fyodorov. Universal statistics of the local green’s function in wave chaotic systems with absorption. *Journal of Experimental and Theoretical Physics Letters*, 82(8):544–548, Oct 2005.
- [46] Geoffroy Lerosey, Julien de Rosny, Arnaud Tourin, and Mathias Fink. Focusing beyond the diffraction limit with far-field time reversal. *Science*, 315(5815):1120–1122, 2007.
- [47] Robert A. Guyer and Paul A. Johnson. Nonlinear mesoscopic elasticity: Evidence for a new class of materials. *Physics Today*, 52(4):30–36, 1999.
- [48] Kristian Dysthe, Harald E. Krogstad, and Peter Mller. Oceanic rogue waves. *Annual Review of Fluid Mechanics*, 40(1):287–310, 2008.

- [49] Min Zhou, Edward Ott, Thomas M. Antonsen, and Steven M. Anlage. Non-linear wave chaos: statistics of second harmonic fields. *Chaos: An Interdisciplinary Journal of Nonlinear Science*, 27(10):103114, 2017.
- [50] X. Li, C. Meng, Y. Liu, E. Schamiloglu, and S. D. Hemmady. Experimental verification of a stochastic topology approach for high-power microwave effects. *IEEE Transactions on Electromagnetic Compatibility*, 57(3):448–453, June 2015.
- [51] D. A. Hill, M. T. Ma, A. R. Ondrejka, B. F. Riddle, M. L. Crawford, and R. T. Johnk. Aperture excitation of electrically large, lossy cavities. *IEEE Transactions on Electromagnetic Compatibility*, 36(3):169–178, Aug 1994.
- [52] David A. Hill. *Electromagnetic Fields in Cavities: Deterministic and Statistical Theories*, chapter Appendix J: Scaling, pages 257–260. Wiley-IEEE Press, 10 2009.
- [53] G. Sinclair. Theory of models of electromagnetic systems. *Proceedings of the IRE*, 36(11):1364–1370, Nov 1948.
- [54] Arthur Whitson. Electromagnetic dimensional scale modeling, 1974. <http://ece-research.unm.edu/summa/notes/In/0200.pdf>.
- [55] Similitude. <https://en.wikipedia.org/wiki/Similitude>.
- [56] Dennis M. Bushnell. Scaling: Wind tunnel to flight. *Annual Review of Fluid Mechanics*, 38(1):111–128, 2006.
- [57] Resistance: Temperature coefficient. <http://hyperphysics.phy-astr.gsu.edu/hbase/electric/restmp.html>.
- [58] Peng Zhang. *Effects of Surface Roughness on Electrical Contact, RF Heating and Field Enhancement*. PhD thesis, University of Michigan, 2012.
- [59] Alan H Kessler. Some practical considerations for reducing surface resistivity for x-band components. Technical report, Massachusetts Inst of Tech Lexington Lincoln Lab, 6 1966.
- [60] Virginia Diode, Inc. *Waveguide Band Designations*, 2015. <http://vadiodes.com/images/AppNotes/VDI'Waveguide'Designations'2015.01.pdf>.
- [61] Matthew Frazier, Biniyam Taddese, Bo Xiao, Thomas Antonsen, Edward Ott, and Steven M. Anlage. Nonlinear time reversal of classical waves: Experiment and model. *Phys. Rev. E*, 88:062910, Dec 2013.
- [62] Matthew Frazier, Biniyam Taddese, Thomas Antonsen, and Steven M. Anlage. Nonlinear time reversal in a wave chaotic system. *Phys. Rev. Lett.*, 110:063902, Feb 2013.

- [63] Sameer Hemmady, Xing Zheng, James Hart, Thomas M. Antonsen, Edward Ott, and Steven M. Anlage. Universal properties of two-port scattering, impedance, and admittance matrices of wave-chaotic systems. *Phys. Rev. E*, 74:036213, Sep 2006.
- [64] Jen-Hao Yeh and Steven M. Anlage. In situ broadband cryogenic calibration for two-port superconducting microwave resonators. *Review of Scientific Instruments*, 84(3):034706, 2013.
- [65] D. A. Hill. A reflection coefficient derivation for the Q of a reverberation chamber. *IEEE Transactions on Electromagnetic Compatibility*, 38(4):591–592, Nov 1996.
- [66] Bisrat Addissie, John Rodgers, and Thomas Antonsen. Extraction of the coupling impedance in overmoded cavities. *Wave Motion*, 87:123–131, 2019. Innovations in Wave Modelling II.
- [67] Bisrat Demeke Addissie. *Methods For Characterizing Electromagnetic Coupling Statistics in Complex Enclosures*. PhD thesis, University of Maryland College Park, 2017. <https://drum.lib.umd.edu/handle/1903/20433>.
- [68] Z. Fu, T. Koch, T.M. Antonsen, E. Ott, and Steven Anlage. Experimental study of quantum graphs with simple microwave networks: Non-universal features. *Acta Physica Polonica A*, 132:1655–1660, 12 2017.
- [69] Shukai Ma, Sendy Phang, Zachary Drikas, Bisrat Addissie, Ronald Hong, Valon Blakaj, Gabriele Gradoni, Gregor Tanner, Thomas M. Antonsen, Edward Ott, and Steven M. Anlage. Efficient statistical model for predicting electromagnetic wave distribution in coupled enclosures. *Phys. Rev. Applied*, 14:014022, Jul 2020.
- [70] Allard P. Mosk, Ad Lagendijk, Geoffroy Lerosey, and Mathias Fink. Controlling waves in space and time for imaging and focusing in complex media. *NATURE PHOTONICS*, 6:283, 2012.
- [71] Edward Haojiang Zhou, Haowen Ruan, Changhui Yang, and Benjamin Judkewitz. Focusing on moving targets through scattering samples. *Optica*, 1(4):227–232, Oct 2014.
- [72] Cheng Ma, Xiao Xu, Yan Liu, and Lihong V. Wang. Time-reversed adapted-perturbation (trap) optical focusing onto dynamic objects inside scattering media. *Nat Photon*, 8(12):931–936, Dec 2014.
- [73] I. M. Vellekoop and A. P. Mosk. Focusing coherent light through opaque strongly scattering media. *OPTICS LETTERS*, 32(16):2309, 2007.
- [74] I. M. Vellekoop, E. G. van Putten, A. Lagendijk, and A. P. Mosk. Demixing light paths inside disordered metamaterials. *Optics Express*, 16:67–80, 2008.

- [75] M. Fink, C. Prada, F. Wu, and D. Cassereau. Self focusing in inhomogeneous media with time reversal acoustic mirrors. In *Ultrasonics Symposium, 1989. Proceedings., IEEE*, pages 681–686 vol.2, Oct 1989.
- [76] M. Fink. Time reversal of ultrasonic fields. i. basic principles. *Ultrasonics, Ferroelectrics, and Frequency Control, IEEE Transactions on*, 39(5):555–566, Sept 1992.
- [77] F. Wu, Jean-Louis Thomas, and M. Fink. Time reversal of ultrasonic fields. II. experimental results. *Ultrasonics, Ferroelectrics, and Frequency Control, IEEE Transactions on*, 39(5):567–578, Sept 1992.
- [78] D. Cassereau and M. Fink. Time-reversal of ultrasonic fields. iii. theory of the closed time-reversal cavity. *Ultrasonics, Ferroelectrics, and Frequency Control, IEEE Transactions on*, 39(5):579–592, Sept 1992.
- [79] Arnaud Derode, Philippe Roux, and Mathias Fink. Robust acoustic time reversal with high-order multiple scattering. *Phys. Rev. Lett.*, 75:4206–4209, Dec 1995.
- [80] Arnaud Derode, Arnaud Tourin, and Mathias Fink. Random multiple scattering of ultrasound. i. coherent and ballistic waves. *Phys. Rev. E*, 64:036605, Aug 2001.
- [81] Arnaud Derode, Arnaud Tourin, and Mathias Fink. Random multiple scattering of ultrasound. ii. is time reversal a self-averaging process? *Phys. Rev. E*, 64:036606, Aug 2001.
- [82] Claire Prada, Estelle Kerbrat, Didier Cassereau, and Mathias Fink. Time reversal techniques in ultrasonic nondestructive testing of scattering media. *Inverse Problems*, 18(6):1761, 2002.
- [83] Dehong Liu, Gang Kang, Ling Li, Ye Chen, S. Vasudevan, W. Joines, Qing Huo Liu, J. Krolik, and L. Carin. Electromagnetic time-reversal imaging of a target in a cluttered environment. *Antennas and Propagation, IEEE Transactions on*, 53(9):3058–3066, Sept 2005.
- [84] Brian E Anderson, Michele Griffa, Carène Larmat, Timothy J Ulrich, and Paul A Johnson. Time reversal. *Acoustics Today*, 4(1):5–16, 2008.
- [85] Hernan L. Calvo, Rodolfo A. Jalabert, and Horacio M. Pastawski. Semiclassical theory of time-reversal focusing. *Phys. Rev. Lett.*, 101:240403, 2008.
- [86] Y.-A. Liou and S.K. Kar. Study of cloud-to-ground lightning and precipitation and their seasonal and geographical characteristics over Taiwan. *Atmospheric Research*, 95(23):115 – 122, 2010. Special Section: Little Alaska Weather Symposium 2008LAWS '08.

- [87] N. Mora, F. Rachidi, and M. Rubinstein. Application of the time reversal of electromagnetic fields to locate lightning discharges. *Atmospheric Research*, 117:78 – 85, 2012. Special Issue dedicated to the 30th International Conference on Lightning Protection (ICLP).
- [88] R. Razzaghi, G. Lugrin, H.M. Manesh, C. Romero, M. Paolone, and F. Rachidi. An efficient method based on the electromagnetic time reversal to locate faults in power networks. *Power Delivery, IEEE Transactions on*, 28(3):1663–1673, July 2013.
- [89] G. Lugrin, N.M. Parra, F. Rachidi, M. Rubinstein, and G. Diendorfer. On the location of lightning discharges using time reversal of electromagnetic fields. *Electromagnetic Compatibility, IEEE Transactions on*, 56(1):149–158, Feb 2014.
- [90] N. Quieffin, S. Catheline, R. K. Ing, and M. Fink. Real-time focusing using an ultrasonic one channel time-reversal mirror coupled to a solid cavity. *J. Acoust. Soc. Am.*, 115:1955, 2004.
- [91] M. Fink. Time reversed acoustics. *Phys. Today*, 50:34–40, 1997.
- [92] C. Draeger and M. Fink. One-channel time reversal of elastic waves in a chaotic 2d-silicon cavity. *Phys. Rev. Lett.*, 79:407, 1997.
- [93] G. Lerosey, J. de Rosny, A. Tourin, A. Derode, G. Montaldo, and M. Fink. Time reversal of electromagnetic waves. *Phys. Rev. Lett.*, 92:193904, May 2004.
- [94] Steven M. Anlage, John Rodgers, Sameer Hemmady, James Hart, Thomas M. Antonsen, and Edward Ott. New results in chaotic time-reversed electromagnetics: High frequency one-recording-channel time reversal mirror. *Acta Physica Polonica A*, 112:569, 2007.
- [95] Jen-Hao Yeh, James A. Hart, Elliott Bradshaw, Thomas M. Antonsen, Edward Ott, and Steven M. Anlage. Experimental examination of the effect of short ray trajectories in two-port wave-chaotic scattering systems. *Phys. Rev. E*, 82:041114, 2010.
- [96] Matthew Frazier, Biniyam Taddese, Thomas Antonsen, and Steven M. Anlage. Nonlinear time-reversal in a wave chaotic system. *Phys. Rev. Lett.*, 110:063902, 2013.
- [97] Matthew Frazier, Biniyam Taddese, Bo Xiao, Thomas Antonsen, Edward Ott, and Steven M. Anlage. Nonlinear time-reversal of classical waves: Experiment and model. *Phys. Rev. E*, 88:062910, 2013.
- [98] Sun K. Hong, Victor M. Mendez, Trystan Koch, Walter S. Wall, and Steven M. Anlage. Nonlinear electromagnetic time reversal in an open semireverberant system. *Phys. Rev. Applied*, 2:044013, Oct 2014.

- [99] Hee Chun Song, W. A. Kuperman, and W. S. Hodgkiss. A time-reversal mirror with variable range focusing. *The Journal of the Acoustical Society of America*, 103(6):3234–3240, 1998.
- [100] Stephane Conti, Philippe Roux, and Mathias Fink. Depth and range shifting of a focal spot using a time-reversal mirror in an acoustic waveguide. *Applied Physics Letters*, 80(19):3647–3649, 2002.
- [101] Biniyam T. Taddese, Gabriele Gradoni, Franco Moglie, Thomas M Antonsen, Edward Ott, and Steven Mark Anlage. Quantifying volume changing perturbations in a wave chaotic system. *New J. Phys.*, 15:023025, 2013.
- [102] Biniyam T. Taddese, James Hart, Thomas M Antonsen, Edward Ott, and Steven Mark Anlage. Sensor based on extending the concept of fidelity to classical waves and overcoming the effects of dissipation. *Appl. Phys. Lett.*, 95:114103, 2009.
- [103] Biniyam T. Taddese, Thomas M Antonsen, Edward Ott, and Steven Mark Anlage. Sensing small changes in a wave chaotic scattering system. *J. Appl. Phys.*, 108:114911, 2010.
- [104] James Hart, E. Ott, and T. Antonsen. The effect of short ray trajectories on the scattering statistics of wave chaotic systems. *Phys. Rev. E*, 80:041109, 2009.
- [105] Jen-Hao Yeh, James Hart, Elliott Bradshaw, Thomas Antonsen, Edward Ott, and Steven M. Anlage. Universal and non-universal properties of wave chaotic scattering systems. *Phys. Rev. E*, 81:025201(R), 2010.
- [106] Biniyam T. Taddese, Thomas M Antonsen, Edward Ott, and Steven Mark Anlage. Mitigating the effect of non-uniform loss on time reversal mirrors. *AIP Advances*, 4:087138, 2014.
- [107] Biniyam Tesfaye Taddese, Thomas M. Antonsen, Edward Ott, and Steven M. Anlage. Iterative time reversal with tunable convergence. *Electronics Letters*, 47:1165, 2011.
- [108] Hans-Jrger Steckmann. *Quantum Chaos*. Cambridge University Press, 1999.
- [109] Paul So, Steven M. Anlage, Edward Ott, and Robert N. Oerter. Wave chaos experiments with and without time reversal symmetry: GUE and GOE statistics. *Phys. Rev. Lett.*, 74:2662–2665, Apr 1995.
- [110] Seok-Hwan Chung, Ali Gokirmak, Dong-Ho Wu, J. S. A. Bridgewater, E. Ott, T. M. Antonsen, and Steven M. Anlage. Measurement of wave chaotic eigenfunctions in the time-reversal symmetry-breaking crossover regime. *Phys. Rev. Lett.*, 85:2482–2485, Sep 2000.

- [111] Sameer Hemmady, Xing Zheng, Edward Ott, Thomas M. Antonsen, and Steven M. Anlage. Universal impedance fluctuations in wave chaotic systems. *Phys. Rev. Lett.*, 94:014102, 2005.
- [112] Suhan Ree and L. E. Reichl. Classical and quantum chaos in a circular billiard with a straight cut. *Phys. Rev. E*, 60:1607–1615, Aug 1999.
- [113] B. Dietz, A. Heine, A. Richter, O. Bohigas, and P. Leboeuf. Spectral statistics in an open parametric billiard system. *Phys. Rev. E*, 73:035201, Mar 2006.
- [114] Jen-Hao Yeh, Zachary Drikas, Jesus Gil Gil, Sun Hong, Biniyam T. Taddese, Edward Ott, Thomas M. Antonsen, Tim Andreadis, and Steven M. Anlage. Impedance and scattering variance ratios of complicated wave scattering systems in the low loss regime. *Acta Phys. Polon. A*, 124:1045, 2013.
- [115] Jen-Hao Yeh and Steven M. Anlage. In situ broadband cryogenic calibration for two-port superconducting microwave resonators. *Rev. Sci. Instrum.*, 84:034706, 2013.
- [116] Carsten Draeger and Mathias Fink. One-channel time-reversal in chaotic cavities: Theoretical limits. *The Journal of the Acoustical Society of America*, 105(2):611–617, 1999.
- [117] Carsten Draeger, Jean-Christian Aime, and Mathias Fink. One-channel time-reversal in chaotic cavities: Experimental results. *The Journal of the Acoustical Society of America*, 105(2):618–625, 1999.
- [118] BT Taddese, MD Johnson, JA Hart, TM Antonsen Jr, E Ott, and SM Anlage. Chaotic time-reversed acoustics: Sensitivity of the loschmidt echo to perturbations. *Acta Physica Polonica, A.*, 116(5), 2009.
- [119] Arnaud Derode, Arnaud Tourin, and Mathias Fink. Ultrasonic pulse compression with one-bit time reversal through multiple scattering. *Journal of Applied Physics*, 85(9):6343–6352, 1999.
- [120] Xing Zheng, Sameer Hemmady, Thomas M. Antonsen, Steven M. Anlage, and Edward Ott. Characterization of fluctuations of impedance and scattering matrices in wave chaotic scattering. *Phys. Rev. E*, 73:046208, 2006.
- [121] Wenlong Gao, Mark Lawrence, Biao Yang, Fu Liu, Fengzhou Fang, Benjamin Béri, Jensen Li, and Shuang Zhang. Topological photonic phase in chiral hyperbolic metamaterials. *Phys. Rev. Lett.*, 114:037402, Jan 2015.
- [122] Wen-Jie Chen, Shao-Ji Jiang, Xiao-Dong Chen, Baocheng Zhu, Lei Zhou, Jian-Wen Dong, and C. T. Chan. Experimental realization of photonic topological insulator in a uniaxial metacrystal waveguide. *Nat Commun*, 5(5782), Dec 2014.

- [123] Kueifu Lai, Tsuhsuang Ma, Xiao Bo, Steven Anlage, and Gennady Shvets. Experimental realization of a reflections-free compact delay line based on a photonic topological insulator. *Scientific Reports*, 6:28453, Jun 2016.
- [124] Alexander B. Khanikaev, S. Hossein Mousavi, Wang-Kong Tse, Mehdi Kar-garian, Allan H. MacDonald, and Gennady Shvets. Photonic topological in-sulators. *Nat Mater*, 12(3):233–239, Mar 2013.
- [125] Xiaojun Cheng, Camille Jouvaud, Xiang Ni, S. Hossein Mousavi, Azriel Z. Genack, and Alexander B. Khanikaev. Robust reconfigurable electromagnetic pathways within a photonic topological insulator. *Nat Mater*, 15(5):542–548, May 2016.
- [126] Bo Xiao, Kueifu Lai, Yang Yu, Tzuhsuan Ma, Gennady Shvets, and Steven M. Anlage. Exciting reflectionless unidirectional edge modes in a reciprocal pho-tonic topological insulator medium. *Phys. Rev. B*, 94:195427, Nov 2016.
- [127] M. Z. Hasan and C. L. Kane. Colloquium : Topological insulators. *Rev. Mod. Phys.*, 82:3045–3067, Nov 2010.
- [128] Xiao-Liang Qi and Shou-Cheng Zhang. Topological insulators and supercon-ductors. *Rev. Mod. Phys.*, 83:1057–1110, Oct 2011.
- [129] K. v. Klitzing, G. Dorda, and M. Pepper. New method for high-accuracy determination of the fine-structure constant based on quantized hall resistance. *Phys. Rev. Lett.*, 45:494–497, Aug 1980.
- [130] F. D. M. Haldane and S. Raghu. Possible realization of directional optical waveguides in photonic crystals with broken time-reversal symmetry. *Phys. Rev. Lett.*, 100:013904, Jan 2008.
- [131] S. Raghu and F. D. M. Haldane. Analogs of quantum-hall-effect edge states in photonic crystals. *Phys. Rev. A*, 78:033834, Sep 2008.
- [132] Mohammad Hafezi, Eugene A. Demler, Mikhail D. Lukin, and Jacob M. Taylor. Robust optical delay lines with topological protection. *Nat Phys*, 7(11):907–912, Nov 2011.
- [133] Kejie Fang, Zongfu Yu, and Shanhui Fan. Realizing effective magnetic field for photons by controlling the phase of dynamic modulation. *Nat Photon*, 6(11):782–787, Nov 2012.
- [134] Ling Lu, Liang Fu, John D. Joannopoulos, and Marin Soljacic. Weyl points and line nodes in gyroid photonic crystals. *Nat Photon*, 7(4):294–299, Apr 2013.
- [135] Scott A. Skirlo, Ling Lu, and Marin Soljačić. Multimode one-way waveguides of large chern numbers. *Phys. Rev. Lett.*, 113:113904, Sep 2014.

- [136] Yaacov E. Kraus, Yoav Lahini, Zohar Ringel, Mor Verbin, and Oded Zilberberg. Topological states and adiabatic pumping in quasicrystals. *Phys. Rev. Lett.*, 109:106402, Sep 2012.
- [137] Mikael C. Rechtsman, Julia M. Zeuner, Yonatan Plotnik, Yaakov Lumer, Daniel Podolsky, Felix Dreisow, Stefan Nolte, Mordechai Segev, and Alexander Szameit. Photonic floquet topological insulators. *Nature*, 496(7444):196–200, Apr 2013.
- [138] M Hafezi, S Mittal, J Fan, A Migdall, and J M Taylor. Imaging topological edge states in silicon photonics. *Nat Photon*, 7(12):1001–1005, Dec 2013.
- [139] Ling Lu, John D. Joannopoulos, and Marin Soljacic. Topological photonics. *Nat Photon*, 8(11):821–829, Nov 2014.
- [140] Zheng Wang, Y. D. Chong, John D. Joannopoulos, and Marin Soljačić. Reflection-free one-way edge modes in a gyromagnetic photonic crystal. *Phys. Rev. Lett.*, 100:013905, Jan 2008.
- [141] Zheng Wang, Yidong Chong, J. D. Joannopoulos, and Marin Soljacic. Observation of unidirectional backscattering-immune topological electromagnetic states. *Nature*, 461(7265):772–775, Oct 2009.
- [142] S. Mittal, J. Fan, S. Faez, A. Migdall, J. M. Taylor, and M. Hafezi. Topologically robust transport of photons in a synthetic gauge field. *Phys. Rev. Lett.*, 113:087403, Aug 2014.
- [143] C. L. Kane and E. J. Mele. Quantum spin hall effect in graphene. *Phys. Rev. Lett.*, 95:226801, Nov 2005.
- [144] B. Andrei Bernevig and Shou-Cheng Zhang. Quantum spin hall effect. *Phys. Rev. Lett.*, 96:106802, Mar 2006.
- [145] Yin Poo, Rui-xin Wu, Zhifang Lin, Yan Yang, and C. T. Chan. Experimental realization of self-guiding unidirectional electromagnetic edge states. *Phys. Rev. Lett.*, 106:093903, Mar 2011.
- [146] Immo Sollner, Sahand Mahmoodian, Sofie Lindskov Hansen, Leonardo Midolo, Alisa Javadi, Gabija Kirsanske, Tommaso Pregnolato, Haitham El-Ella, Eun Hye Lee, Jin Dong Song, Soren Stobbe, and Peter Lodahl. Deterministic photon-emitter coupling in chiral photonic circuits. *Nat Nano*, 10(9):775–778, Sep 2015.
- [147] A. V. Karavaev, N. A. Gumerov, K. Papadopoulos, Xi Shao, A. S. Sharma, W. Geckelman, A. Gigliotti, P. Pribyl, and S. Vincena. Generation of whistler waves by a rotating magnetic field source. *Physics of Plasmas*, 17(1):012102, 2010.

- [148] A. Gigliotti, W. Gekelman, P. Pribyl, S. Vincena, A. Karavaev, X. Shao, A. Surjalal Sharma, and D. Papadopoulos. Generation of polarized shear alfvén waves by a rotating magnetic field source. *Physics of Plasmas*, 16(9):092106, 2009.
- [149] Cecil E Hayes, William A Edelstein, John F Schenck, Otward M Mueller, and Matthew Eash. An efficient, highly homogeneous radiofrequency coil for whole-body NMR imaging at 1.5 T. *Journal of Magnetic Resonance (1969)*, 63(3):622 – 628, 1985.
- [150] G.H Glover, C.E Hayes, N.J Pelc, W.A Edelstein, O.M Mueller, H.R Hart, C.J Hardy, M O'Donnell, and W.D Barber. Comparison of linear and circular polarization for magnetic resonance imaging. *Journal of Magnetic Resonance (1969)*, 64(2):255 – 270, 1985.
- [151] Brown George. Antenna system, July 13 1937. U.S. Patent 2086976.
- [152] L. Griffee and M. Anderson. Antenna for airborne satellite communications, May 1974. U.S. Patent 3811127.
- [153] J.D. Kraus. *Antennas*. Electrical Engineering Series. McGraw-Hill, 1988.
- [154] Shukai Ma, Bo Xiao, Yang Yu, Kueifu Lai, Gennady Shvets, and Steven M. Anlage. Topologically protected photonic modes in composite quantum hall/quantum spin hall waveguides. *Phys. Rev. B*, 100:085118, Aug 2019.
- [155] Shukai Ma and Steven M. Anlage. Microwave applications of photonic topological insulators. *Applied Physics Letters*, 116(25):250502, 2020.